NAVAL POSTGRADUATE SCHOOL

MONTEREY, CALIFORNIA

DISSERTATION

**EVOLUTION OF ATMOSPHERE AND OCEAN
BOUNDARY LAYERS FROM AIRCRAFT
OBSERVATIONS AND COUPLED COAMPS/NCOM**

by

Heather R. Hornick

September 2012

Dissertation Supervisor: Qing Wang

Approved for public release; distribution is unlimited

THIS PAGE INTENTIONALLY LEFT BLANK

1. AGENCY USE ONLY *(Leave blank)*	2. REPORT DATE September 2012	3. REPORT TYPE AND DATES COVERED Dissertation	
4. TITLE AND SUBTITLE: Evolution of Atmosphere and Ocean Boundary Layers from Aircraft Observations and coupled COAMPS/NCOM		5. FUNDING NUMBERS	
6. AUTHOR(S) Heather R Hornick			
7. PERFORMING ORGANIZATION NAME(S) AND ADDRESS(ES) Naval Postgraduate School Monterey, CA 93943-5000		8. PERFORMING ORGANIZATION REPORT NUMBER	
9. SPONSORING / MONITORING AGENCY NAME(S) AND ADDRESS(ES) N/A		10. SPONSORING / MONITORING AGENCY REPORT NUMBER	

11. SUPPLEMENTARY NOTES The views expressed in this thesis are those of the author and do not reflect the official policy or position of the Department of Defense or the U.S. Government. IRB Protocol number _____N/A_____.

12a. DISTRIBUTION / AVAILABILITY STATEMENT Authorized for public release; distribution is unlimited	12b. DISTRIBUTION CODE

13. ABSTRACT (maximum 200 words)

Strong offshore winds are frequently observed over the Gulf of Tehuantepec in the eastern Pacific Ocean when synoptic conditions create a cross-isthmus pressure gradient through the Chivela Pass in southern Mexico. During such high wind events, turbulent mixing and upwelling in the upper-ocean can reduce the sea-surface temperature by several degrees within hours of event onset. This research conducts an extensive analysis of aircraft measurements from the 2004 Gulf of Tehuantepec Experiment (GOTEX). Combined with coupled COAMPS/NCOM simulations, this research provides new insight into the spatial and temporal evolution of the marine and atmospheric boundary layers during outflow events. Three regions within the outflow are identified with distinct response characteristics. The addition of COAMPS simulations reveals the three-dimensional variations of the outflow jet not visible from the observations and the presence of a secondary outflow jet to the east that influences the symmetry of the atmospheric forcing. Calculations of the ocean mixed layer heat budget indicate entrainment mixing as the dominant cooling mechanism during outflow events. An evaluation of the fully-coupled model reveals minimal improvement in wind speed and stress, temperature, and moisture, but shows the greatest improvement in the air-sea temperature difference and surface sensible and latent heat fluxes.

14. SUBJECT TERMS Gap winds, gap outflow, air-sea interaction, turbulent fluxes, Gulf of Tehuantepec, COAMPS, NCOM, coupled model, heat budget, ocean mixed layer, atmospheric boundary layer	15. NUMBER OF PAGES 187
	16. PRICE CODE

17. SECURITY CLASSIFICATION OF REPORT Unclassified	18. SECURITY CLASSIFICATION OF THIS PAGE Unclassified	19. SECURITY CLASSIFICATION OF ABSTRACT Unclassified	20. LIMITATION OF ABSTRACT UU

THIS PAGE INTENTIONALLY LEFT BLANK

EVOLUTION OF ATMOSPHERE AND OCEAN BOUNDARY LAYERS FROM AIRCRAFT OBSERVATIONS AND COUPLED COAMPS/NCOM

Heather R. Hornick
Lieutenant Commander, United States Navy
B.S., University of South Carolina, 2002
S.M., Massachusetts Institute of Technology/Woods Hole Oceanographic Institution, 2009

Submitted in partial fulfillment of the
requirements for the degree of

DOCTOR OF PHILOSOPHY IN METEOROLOGY

from the

NAVAL POSTGRADUATE SCHOOL
September 2012

Author: _____
Heather R. Hornick

Approved by:

_____   _____
Qing Wang   Josh Hacker
Professor of Meteorology   Professor of Meteorology
Dissertation Supervisor

_____   _____
Patrick Harr   Rebecca Stone
Professor of Meteorology   Professor of Oceanography

_____   _____
Xiaodong Hong   Shouping Wang
Naval Research Laboratory   Naval Research Laboratory

Approved by: _____
Wendell Nuss, Chair, Department of Meteorology

Approved by: _____
Douglas Moses, Vice Provost for Academic Affairs

iii

THIS PAGE INTENTIONALLY LEFT BLANK

ABSTRACT

Strong offshore winds are frequently observed over the Gulf of Tehuantepec in the eastern Pacific Ocean when synoptic conditions create a cross-isthmus pressure gradient through the Chivela Pass in southern Mexico. During such high wind events, turbulent mixing and upwelling in the upper-ocean can reduce the sea-surface temperature by several degrees within hours of event onset. This research conducts an extensive analysis of aircraft measurements from the 2004 Gulf of Tehuantepec Experiment (GOTEX). Combined with coupled COAMPS/NCOM simulations, this research provides new insight into the spatial and temporal evolution of the marine and atmospheric boundary layers during outflow events. Three regions within the outflow are identified with distinct response characteristics. The addition of COAMPS simulations reveals the three-dimensional variations of the outflow jet not visible from the observations and the presence of a secondary outflow jet to the east that influences the symmetry of the atmospheric forcing. Calculations of the ocean mixed layer heat budget indicate entrainment mixing as the dominant cooling mechanism during outflow events. An evaluation of the fully-coupled model reveals minimal improvement in wind speed and stress, temperature, and moisture, but shows the greatest improvement in the air-sea temperature difference and surface sensible and latent heat fluxes.

THIS PAGE INTENTIONALLY LEFT BLANK

TABLE OF CONTENTS

LIST OF FIGURES

xiv

THIS PAGE INTENTIONALLY LEFT BLANK

LIST OF TABLES

THIS PAGE INTENTIONALLY LEFT BLANK

LIST OF ACRONYMS AND ABBREVIATIONS

ABL	Atmospheric Boundary Layer
ADCP	Acoustic Doppler Current Profiler
ADSCAT	Advance Scatterometer
AXBT	Airborne expendable bathythermograph
COAMPS	Coupled Ocean/Atmospheric Mesoscale Prediction System
CSM	Climate System Model
CTD	Conductivity, Temperature and Depth
CZ	Coupling Zone
DBDB2	Digital Bathymetric Data Base
ESMF	Earth System Modeling Framework
GFS	Global Forecast System
GoT	Gulf of Tehuantepec
GOTEX	Gulf of Tehuantepec Experiment
MABL	Marine Atmospheric Boundary Layer
MCT	Model Coupling Toolkit
MPI	Message Passing Interface
NAM	North American Model
NAVDAS	NRL Atmospheric Variational Data Assimilation System
NCAR	National Center for Atmospheric Research
NCEP	National Center for Environmental Prediction
NCODA	Navy Coupled Ocean Data Assimilation
NCOM	Navy Coastal Ocean Model
NHC	National Hurricane Center

NOGAPS	Navy Operational Global Atmospheric Prediction System
NPS	Naval Postgraduate School
NRL	Naval Research Laboratory
NS	Nearshore
OML	Ocean mixed layer
RMSE	Root Mean Squared Error
$RMSE_C$	Centered Root Mean Squared Error
$RMSE_{CN}$	Normalized Centered Root Mean Squared Error
SLP	Sea Level Pressure
SST	Sea-surface Temperature
TOGA-COARE	Tropical Ocean Global Atmosphere Coupled Ocean-Atmosphere Response Experiment
TKE	Turbulent Kinetic Energy
QuikSCAT	Quick Scatterometer

ACKNOWLEDGMENTS

First, I would like to thank my advisor, Professor Qing Wang, for the time and energy that she so willingly gave. Qing, you made everyday a fun and valuable experience. I have learned so much from you and am grateful for all of the time we have spent together discussing science, and just about everything else.

To my committee members, Dr. Xiaodong Hong, Dr. Shouping Wang, Professor Joshua Hacker, Professor Patrick Harr, and CAPT Rebecca Stone: for your support and enthusiasm during this process. I am grateful for your feedback and contributions.

Special thanks to Dr. Xiaodong Hong for providing the model simulations and continuous support while I was learning to work with the model data.

To Professor Emeritus R. L. Haney: for your fascinating insight into the dynamics of the ocean mixed layer and the heat budget problem.

To Carl Friehe, Djamal Khelif, and Ken Melville for the data collections efforts of GOTEX, which provided such a comprehensive data set.

To John Kalogiros for providing many of the data analyses tools used in this study.

To Mary Jordan for providing critical MATLAB support.

To Kurt Nielsen for obtaining satellite imagery.

Finally, I would like to thank my friends and family who have supported me every day of this journey. There are too many names to list but I am grateful for every one of you. Mom and Dad, even when I doubted myself you lifted me up and pushed me forward. I made it to this day because of your unconditional love and support. I can never truly express my love and gratitude. Johnny, your love makes me stronger every single day. Thank you for standing by my side during this journey. I cannot wait to stand by your side for the rest of our lives. I love you!

THIS PAGE INTENTIONALLY LEFT BLANK

I.   INTRODUCTION

A.   THE GULF OF TEHUANTEPEC GAP WIND OUTFLOW

When synoptic conditions set up a pressure gradient through a low-level mountain pass, funneling of low-level flow through the pass can occur. The strongest wind speeds occur at the gap exit due to acceleration by the local pressure gradient, rather than at the gap entrance, as would be expected based on the Bernoulli principle. These strong winds are referred to as gap winds and occur in a variety of locations, such as the Gulf of Tehuantepec (Steenburgh et al. 1998); the Strait of Juan de Fuca (Overland and Walter 1981); the Frasier River Valley of Washington and British Columbia (Mass et al.1995); and the Strait of Gibraltar (Dorman et al.1995). A detailed discussion of the gap wind phenomenon can be found in the COMET®[1] module on gap winds at https://www.meted.ucar.edu/ (UCAR, 2012).

The gap outflow is the extension of a gap wind downstream of a terrain restriction (Steenburgh et al. 1998). Gap wind outflow events in southern Mexico, over the Gulf of Tehuantepec, produce strong, far-reaching offshore winds and significant cooling of sea-surface temperatures (Steenburgh et al. 1998). While the ocean upwelling induced by these events enhances local nearshore fishing by bringing nutrients to the surface, the strong winds associated with these events can be inherently dangerous to coastal vessels if not well-predicted. Early ship reports of strong northerly winds far offshore in the Gulf of Tehuantepec that corresponded to coastal measurements of gap wind events in the Chivela Pass suggested that the gap outflow had a broad area of influence beyond the constraints of the mountain pass. Unlike other gap wind locations, such as the Strait of Juan de Fuca, the Gulf of Tehuantepec outflow extends several hundred kilometers offshore and strong winds fan out over a broad region. These gap outflow events are known locally as a Tehuantepecer or Tehuano (Hurd 1929; Trasviña et al. 1995). The development and evolution of the atmospheric and ocean boundary layers during these

---

[1] COMET® is a registered trademark of UCAR. ©1997-2011. University Corporation for Atmospheric Research.

events are due to a combination of several dynamic mechanisms including synoptic forcing, topographic forcing, and air-sea interactions.

Numerous studies, both observational and simulated, have been conducted on the Gulf of Tehuantepec gap outflow. The synoptic forcing by Central American cold surges over the eastern slopes of the Sierra Madre Mountains or within the Gulf of Mexico is well understood (Schultz et al. 1997; Schultz et al. 1998). The anticyclonic turning of the outflow jet and the asymmetric response of the atmosphere and ocean were originally deduced from idealized simulations (Clarke 1988; McCreary et al. 1989). Observational studies include a limited number of local field experiments (Barton et al. 1993; Trasviña et al.1995), and analysis of satellite observations of sea-surface temperature and surface winds (Stumpf 1975; Chelton et al. 2000a, b; Xie et al. 2005). The most detailed mesoscale study of the gap outflow was by Steenburgh et al. (1998) using an uncoupled atmospheric model (MM5 at 6.67 km grid spacing) to determine the structure and evolution of the atmospheric boundary layer within the Gulf of Tehuantepec outflow. Steenburgh et al. (1998) included a detailed analysis of the balance of the cross-flow pressure gradient acceleration with the Coriolis acceleration on the observed anticyclonic turning of the outflow jet. There have been no studies conducted using high-resolution, co-located atmosphere and ocean measurements during multiple outflow events or using a two-way coupled ocean-atmosphere mesoscale model. The 2004 Gulf of Tehuantepec Experiment (GOTEX) data set provided co-located atmosphere and ocean measurements during five gap outflow events.

While the synoptic forcing and the general atmospheric feature of the outflow is fairly well understood, the air-sea interactions and the response of the ocean mixed layer to the outflow forcing are not. This study focuses on understanding the small-scale spatial and temporal characteristics of the atmospheric boundary layer and ocean mixed layer, the role of the air-sea interactions in influencing the evolution of the gap outflow, and determining the dominant mechanisms that lead to the significant cooling of sea-surface temperatures in response to gap outflow events.

2

B.   RECENT MODEL EVALUATIONS

Based on a 10-year climatology of ocean surface vector wind data from the NASA Quick Scatterometer (QuikSCAT) satellite, from 19992009, of the Gulf of Tehuantepec, there are an average of 11.9 gale-force gap outflow events (34–47 kts) and 8.1 storm-force events (48–63 kts) per season (Brennan et al. 2010). An operational model evaluation by Brennan et al. (2010) found that while the National Center for Environmental Prediction (NCEP) Global Forecast System (GFS) and the North American Model (NAM) have some ability to predict gale-force events, neither has skill at predicting storm-force events. Forecasters at the National Hurricane Center Tropical Analysis and Forecast Branch (NHC TAFB) use a variety of atmospheric models when releasing high winds and seas forecasts for the Gulf of Tehuantepec. However, the models commonly underestimate the surface winds (E. Christensen 2011, personal communication). Verification of wind speed relies heavily on satellite derived winds that do not provide the grid spacing necessary to resolve the strongest winds in the outflow jet core.   Additionally, the Advance Scatterometer (ADSCAT), the replacement to QuikSCAT, has resulted in a 40% decrease in available passes over the Gulf of Tehuantepec region since 2006.

A study by Cherrett (2006) of the COAMPS V. 3 simulations for one GOTEX gap outflow event revealed that the general features of the gap wind outflow is well represented by the uncoupled atmospheric component. However, the small scale variability in surface fluxes and turbulent kinetic energy is not. The largest deficiencies were found in areas where air-sea processes, rather than topographic effects, dominate the surface fluxes and boundary layer dynamics. Such deficiencies adversely affect simulations of the upper-ocean because of the large uncertainties in the upper-ocean forcing terms. These deficiencies also suggest that a coupled model approach may be beneficial (Steenburgh et al. 1998).

C.   THE COUPLED MODEL APPROACH

Traditional stand-alone atmospheric or ocean models rely on fixed input during forecast initialization for forcing fields (such as wind stress) or boundary conditions (such

3

as sea-surface temperature). In regions where the atmospheric boundary layer and ocean mixed layer are strongly coupled and processes within either boundary layer feed back to the other, a two-way coupled model should lead to improvements in the estimation of surface quantities, such as sensible and latent heat fluxes. Although the framework for coupled ocean-atmosphere mesoscale models has been available for some time (Hodur 1997), the required computational ability has, until recently, been a limiting factor. Coupled models are currently being used for idealized simulations (Deng et al. 2009; Lie et al. 2010; Perlin et al. 2011), and climate modeling (von Storch 2000; Fu et al. 2006), as well as in combination with observational studies to understand the behavior of the coupled model, and evaluate the performance of the coupled model versus the stand-alone models (Chen et al. 2010; Allard et al. 2010).

Several studies have suggested the benefits of higher-frequency air-sea coupling for better representation of sea-surface temperature changes in atmospheric models and thus improved estimation of surface fluxes (Steenburgh et al.1998; Powers and Stoelinga 2000; Drennan et al. 2003; Lebeaupin-Brossier et al. 2009). For this study, high-resolution coupled simulations of the GOTEX period using the Coupled Ocean-Atmosphere Mesoscale Prediction System (COAMPS®2) and the Navy Coastal Ocean Model (NCOM) were provided by Dr. Xiaodong Hong, Naval Research Laboratory (NRL) Monterey.

D.   OBJECTIVES OF RESEARCH

The atmospheric boundary layer and the ocean mixed layer comprise the primary operating environment for the US Navy's ships, submarines, and aircraft. Improving our forecast ability of the marine atmospheric boundary layer and ocean mixed layer improves our understanding of the operating environment, and allows us to maximize the performance of our sensors and weapons. Additionally, coastal regions where the air-sea boundary layers are strongly coupled are a source of income and sustainment for countries all over the world. A better understanding of air-sea boundary layer dynamics

---

2 COAMPS® is a registered trademark of the Naval Research Laboratory.

and improved prediction of strong winds, such as the gap outflow, can lead to safer, more efficient fishing practices for these coastal economies.

Although the dynamics of the Gulf of Tehuantepec outflow jet have been studied for decades, concurrent measurements of the atmospheric boundary layer and ocean mixed layer are not widely available. Therefore, many of the previous studies have focused on the synoptic and topographic forcing of gap outflow events. Modeling studies of this region have used only stand-alone atmospheric or ocean models, and have often relied on sparse *in situ* observations and satellite sea-surface temperatures and derived wind fields. The validation test report for coupled COAMPS/NCOM relied on bulk method estimates to determine the surface fluxes, rather than *in situ* flux measurements (Allard et al. 2010).

This study includes analysis of aircraft measurements of the atmospheric boundary layer and ocean mixed layer from the 2004 GOTEX field campaign and simulations of a two-way coupled ocean-atmosphere mesoscale model. Simulations of the stand-alone COAMPS V. 5, the stand-alone NCOM V. 4, and the fully-coupled COAMPS/NCOM models were provided by NRL Monterey.

This work focuses on furthering our understanding of the air-sea interactions within the Gulf of Tehuantepec outflow region using aircraft observations and two-way coupled-model simulations. It is suggested that the atmospheric boundary layer and ocean mixed layer have a strongly coupled response during gap outflow events, similar to other strong wind events, such as tropical cyclones (Bao et al. 1999; Zhang et al. 2009). In addition to topographic forcing near the coast, air-sea processes play a key role in defining the structure of the marine atmospheric boundary layer and ocean mixed layer.

The three objectives of this study are 1) to improve the understanding of the air-sea coupling processes, including the small-scale spatial and temporal variability of the atmospheric boundary layer and ocean mixed layer, within the GoT gap outflow using a combination of observations and simulations; 2) to determine the dominant mechanisms that lead to strong cooling of the sea-surface temperature; 3) to evaluate the performance of the fully-coupled COAMPS/NCOM model using the GOTEX observations and stand-

5

alone model simulations to determine the effect of two-way coupling on the surface fluxes and boundary layer properties.

The extensive GOTEX data set provided greater spatial and temporal coverage of the gap outflow during five outflow events compared to all previous observational studies in this region. Analysis of the aircraft observations identified three regions within the outflow that have distinct response characteristics. The Nearshore region, over the continental shelf, is the region with the strongest atmospheric forcing during the intensification stage of the outflow event. The boundary layer stabilizes in response to the outflow forcing due to cold sea-surface temperatures. The outflow jet is at maximum elevation and strength, and the sea-surface temperatures cool the most within this region. The Coupling Zone region has cooler sea-surface temperatures, slightly weaker winds, and the strongest latent heat flux. During the decay stage, the atmospheric forcing is strongest within the Coupling Zone. The Offshore region is influenced by the strong northerly winds of the gap outflow, but generally does not show obvious oceanic response to the outflow forcing. The ocean mixed layer remains relatively deep and warm, while the boundary layer air remains warm and moist. These spatial and temporal characteristics are revealed for the first time in this study.

Calculations of the ocean mixed layer heat budget from the coupled NCOM simulations indicated that entrainment mixing at the base of the mixed layer is the dominant mechanism for cooling of the sea-surface temperatures. Loss of heat due to upward heat flux also contributes to cooling. Closest to the coast, upwelling from divergence caused by offshore flow provides additional cooling; such effects are minimal in the Coupling Zone and Offshore regions. The time variation of the heat budget terms suggests different recovery time periods for each of the identified outflow regions.

Model error statistics of the uncoupled and two-way coupled models showed the largest improvement in variables related to the air-sea temperature difference. Improved sea-surface temperatures led to better prediction of the air-sea temperature difference, which resulted in improvement in the sensible and latent heat fluxes. The evaluation revealed no improvement in wind speed and minor improvements in potential

temperature and specific humidity. However, the greatest improvement is the more realistic atmospheric forcing for the upper-ocean due to surface heat fluxes.

E.   SUMMARY OF DISSERTATION

Chapter II provides background information on the Gulf of Tehuantepec gap wind outflow, including case studies of the atmospheric boundary layer and ocean mixed layer response to the outflow forcing, and an overview of coupled ocean-atmosphere modeling. Chapter III describes the GOTEX field campaign, the model setup, and the methods used for analysis of aircraft observations and model simulations. In Chapter VI, the analysis of GOTEX observations is presented, including case studies of two gap outflow events. The results of the coupled model simulations are presented in Chapter V, along with calculations of the heat budget in the ocean mixed layer. In Chapter VI, an evaluation of the fully-coupled COAMPS/NCOM using GOTEX observations and the stand-alone COAMPS and NCOM simulations is presented. Chapter VII provides a summary of this study, conclusions, and recommendations for future work.

THIS PAGE INTENTIONALLY LEFT BLANK

II.   BACKGROUND

A.   OVERVIEW OF THE GULF OF TEHUANTEPEC GAP OUTFLOW

The Sierra Madre mountain range runs along Mexico and Central America, separating the lower atmosphere over the Gulf of Mexico from that over the Pacific Ocean. A notable break in this mountain range is the Chivela Pass, which separates the Bay of Campeche from the Gulf of Tehuantepec (GoT, Figure 1). The Chivela Pass is 220 km long and 40 km wide with a maximum elevation of approximately 250 m (Steenburgh et al. 1998). Near the entrance of the Chivela Pass is a small topographic feature, Cerro Santa Marta, with an elevation of 750 m. To the west, the maximum topographic elevation is 2000 m, slightly higher than to the east, 1500 m. Along 93°W, there is another pass approximately 200 km east of the Chivela Pass with a minimum elevation of 750 m, which spans the width of the isthmus.
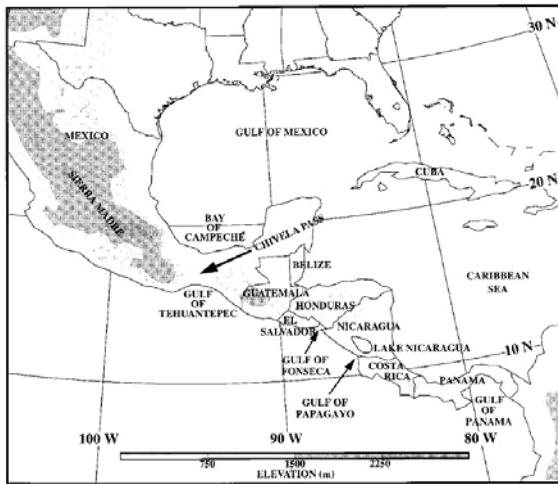
Figure 1.   Map of Mexico and Central America including Chivela Pass and the Gulf of Tehuantepec (from Steenburgh et al. 1998).

The existence of a high-pressure ridge north and east of the Sierra Madre Mountains or in the Gulf of Mexico can set up favorable conditions for gap outflow events in the GoT. The most common initiation of these events is related to Central American cold surges, which bring cold air south of 20°N over Central America (Schultz et al. 1997). These surges, typically lasting from 2–6 days, strengthen the pressure

gradient through the Chivela Pass and lead to the evolution of a gap wind event (Trasviña et al. 1995). These events are common from November to March.

As mentioned previously, a Tehuano differs from other gap winds in that strong outflow winds are often observed several hundred kilometers from the gap exit. The gap outflow is often identified by a convective cloud band, or rope cloud, marking the leading edge with a fairly cloud free region behind it. The oceanic response is upwelling and entrainment of cold water, with an often dramatic decrease in sea-surface temperature (SST). Sea-surface temperatures have been observed to cool as much as 8 °C in a few hours (Stumpf 1975; Schultz et al. 1997). Roden (1961) noted that observations of the coldest sea-surface temperatures were often found offshore, rather than closest to the coast.

The outflow associated with a Tehuano usually exhibits anticyclonic curvature to the west of the jet axis and weaker cyclonic curvature to the east of the jet axis, represented by the blue and red dashed arrows in Figure 2, respectively. Clarke (1988) studied the GoT jet to compare the observed turning to a wind path predicted by an inertial turning radius. The outflow trajectories result from a balance of Coriolis, centrifugal and pressure gradient forces. However, the trajectories to the west show anticyclonic curvature of smaller radius than predicted by inertial balance, due to the pressure gradient force and Coriolis force acting in the same direction (Steenburgh et al. 1998). To the east, the pressure gradient force and Coriolis force act in opposite directions resulting in a larger radius of curvature, and straight or even cyclonic trajectories. The linear model by Clarke (1988) predicted a symmetric response in the ocean with upwelling and shallowing of the thermocline to the east equal to the downwelling and deepening of the thermocline to the west. Since then, observations and additional studies have highlighted the asymmetric response of both the ocean and atmosphere to the gap outflow forcing.
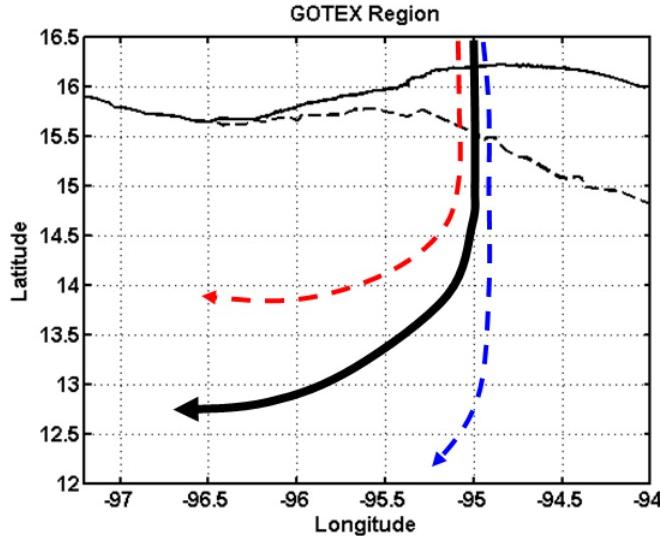
Figure 2. Schematic of general gap outflow trajectories from the gap exit. The solid black arrow represents trajectories along the outflow jet core. The red and blue dashed arrows represent trajectories to the west and east of the axis, respectively. These trajectories are approximations for illustrative purposes only.

B. CASE STUDIES OF THE GULF OF TEHUANTEPEC GAP OUTFLOW

Trasviña et al. (1995) analyzed observations from the 1989 Tehuano field campaign were analyzed to better understand the characteristic symmetric forcing of the Gulf of Tehuantepec outflow jet and the asymmetric ABL and OML response. The observed wind event began with a greater than 10 m s^{-1} increase in wind speed in less than 3 hours; reached its maximum wind speed within 15 hours, and began to weaken within 60 hours. The wind speed decline occurred in two abrupt steps. Shoreward of 14°N, the winds were symmetrical about the jet axis.

Sea-surface temperatures cooled throughout the Gulf beneath the influence of the outflow jet, with the coldest surface temperatures measured within the central GoT, not closest to the coast. The offshore surface current followed the curvature of the well-formed anticyclonic eddy to the west, while a weak cyclonic circulation was measured to the east. Warm water near the coast on the west side of the GoT flowed in a converging current toward the mouth of the gap exit. This warm water was entrained into the western boundary of the offshore current and wrapped around the anticyclonic eddy. Positive temperature anomalies were measured to the west in the near-surface waters,

11

while weak negative anomalies below 50 m suggested upwelling based on the decrease in thermocline depth. Negative temperature anomalies were spread throughout the central Gulf as a result of strong entrainment beneath the outflow jet. East of the outflow jet, cooler surface temperatures and a band of positive temperature anomalies at 30 m depth resulted from entrainment mixing at the base of the mixed layer. Heat budget estimations showed that the rapid cooling was much larger than that accounted for by loss of heat at the ocean surface by sensible and latent heat fluxes, and longwave radiation.

Trasviña et al. (1995) concluded that entrainment mixing was the primary mechanism for cooling surface temperatures. The asymmetric ocean circulation was determined to be a result of Ekman convergence and divergence within the climatically shallow OML within this region. Ekman divergence within the shallow OML east of the outflow combined with weaker density gradients due to enhanced entrainment resulted in weaker geostrophic flow within the cyclonic circulation.

Steenburgh et al. (1998) conducted a case study of the GoT gap outflow using a stand-alone atmospheric model to determine the simulated structure and evolution of the outflow. The study used the mesoscale model MM5 with a minimum grid spacing of 6.67 km and 30 vertical levels. A mesoscale pressure ridge formed along the axis of the gap with an anticyclonic and a cyclonic eddy forming to the west and east of the outflow, respectively. The cold northerly flow was strong enough to flow over the mountains to the east and west, and therefore, not entirely contained within the gap. A stronger pressure gradient to the west suggested a stronger lee trough due to the mountains to the west of the pass. The layer of cold boundary layer air was 200 hPa deep along the jet axis, thinning to either side, and resulted in a maximum potential temperature decrease of 7 K. Surface winds were stronger over the GoT than immediately beyond the coast, where there was a maximum in vertical wind shear. The simulations showed the fan-like spreading of the outflow which was attributed to the contributions of cross-flow pressure gradient accelerations which increase away from the axis of the jet core. The study concluded that the greater downstream extension of the GoT outflow compared with other gap wind regions was due to weak synoptic scale forcing, lack of terrain features beyond the exit of the pass, and a small Coriolis parameter. Additionally, the

asymmetrical response of the outflow was due to the uneven terrain producing stronger lee troughing to the west than to the east. Finally, the study suggested that a coupled-model approach may be beneficial due to the large variability in sea-surface temperatures and surface roughness during outflow events.

Cherrett (2006) conducted a study of COAMPS V. 3 simulations and GOTEX data for 26–27 February 2004, which revealed deficiencies in the surface flux estimation away from the jet axis where air-sea exchanges dominate. The general features of the gap wind outflow were well modeled in the wind fields, but the boundary layer height and elevation of the outflow jet were too high. The axis and western side of the outflow jet was well-simulated by COAMPS, which captured the anticyclonic turning of the jet. However, COAMPS did a poor job in simulating the southeastern extent of the outflow. The building of a high-pressure ridge along the jet axis was captured in the pressure fields. COAMPS simulated an unstable boundary layer and positive sensible and latent heat fluxes throughout the region, while aircraft data showed a transition to a stable air-sea boundary layer within the jet and areas of negative sensible and latent heat flux. Comparison of COAMPS and dropsondes revealed that the boundary layer was not well modeled. There was a cold bias in potential temperature throughout the domain and the sea-surface temperature was generally too warm. COAMPS over-predicted both latent and sensible heat fluxes and under-predicted turbulent kinetic energy.

Konstantinou (2006) compared GOTEX Airborne Expendable Bathythermographs (AXBTs) to the Naval Postgraduate School Ocean mixed layer (NPS OML) model forced by COAMPS output at each COAMPS grid point. He found that the NPS OML model simulated substantial changes in sea-surface temperature that were not represented in the uncoupled COAMPS SST field. Sensitivity testing of the OML model was used to evaluate changes in upwelling, wind stress, and heat fluxes to determine the dominant physical process affecting the upper-ocean during a Tehuano. He determined that the OML depth, and hence the depth of the top of the thermocline was critical to the response of the upper-ocean.

McCreary et al. (1989) used 1 ½ -layer ocean models to study the ocean response to gap outflow forcing in the GoT. The offshore wind created an ageostrophic offshore

current, which was not Ekman flow, forcing coastal upwelling. The offshore ageostrophic flow resulted in decreased sea height near the coast, and the coastal upwelling brought cold water toward the surface. Entrainment at the bottom of the mixed layer from turbulent mixing cooled the OML temperatures along the axis of the jet core and to the east. The coldest sea-surface temperatures were nearshore, although significant cooling was also simulated offshore. The results of the nonlinear model suggested a long relaxation period for the cold sea-surface temperatures to return to normal (50 days).

Anticylconic and cyclonic eddies spun up to the west and east, respectively, but did not develop symmetrically. The change in depth of the thermocline was greater to the west than to the east. The cyclonic eddy was much weaker and less circular in shape than the anticyclonic eddy to the west. Horizontal advection strengthened the anticyclonic eddy, while entrainment weakened the cyclonic eddy. The anticyclonic eddies propagated westward with the speed of local nondispersive Rossby waves which increased as the mixed layer depth at the center of the eddy increased.

Coastal currents converged at the mouth of the gap and resulted in filaments of warm and cold water being wrapped around the anticyclonic eddy. The linear model results were comparable to the symmetric response by Clarke (1988). The nonlinear model, with variable Coriolis parameter input, resulted in an asymmetric response which was closer to the typically observed response.

The offshore surface current, which develops as a result of the offshore wind jet, was named a "Super-squirt" by Barton et al. (1993). Using measurements from Acoustic Doppler Current Profilers (ADCPs), Conductivity, Temperature, Depth (CTD) casts, and ocean moorings, Barton et al. studied the dynamics of the GoT ocean current. Within a few hours of onset of the outflow winds, a strong southward current up to 1 m s^{-1} had formed. Convergent flow near the mouth of the gap was also observed. A cusp-like signature of cold sea-surface temperatures was observed in the satellite sea-surface temperature imagery within the central Gulf. Twenty-four hours after onset of strong winds, the central sea-surface temperature anomaly began to weaken while the coastal sea-surface temperatures continued to cool. Within one week, sea-surface temperatures

throughout the GoT had returned to pre-event conditions. The asymmetric thermocline response agreed with the nonlinear model of McCreary et al. (1989), with the maximum thermocline elevation to the east of the jet core. Horizontal advection and wrapping of warm water around the anticyclonic eddy was observed in agreement with the model. Cross-sections of the anticyclonic eddy revealed that it was fairly symmetric in structure, with an OML depth of 120 m at the center. Following the field-phase of the study, satellite imagery suggested that a rapid succession of wind events may strengthen the anticyclonic eddy before it has time to propagate westward. Results of this study also suggest that the dominant mechanism contributing to the cooling of sea-surface temperatures is entrainment mixing at the bottom of the ocean mixed layer rather than surface heat fluxes.

C.   THE COUPLED MODELING APPROACH

Two-way coupled ocean-atmosphere mesoscale models are currently being used in research mode for idealized simulation studies, and undergoing extensive evaluation for validation and transition to operations. The coupling of ocean-atmosphere models is important because air-sea interactions provide feedback to the atmospheric boundary layer and ocean mixed layer, which can affect the structure and evolution of both boundary layers. The stability of the atmospheric surface layer, the air-sea temperature difference and the magnitude of the wind speed determine the direction and magnitude of surface heat fluxes that result in changes in the ocean mixed layer temperature or the boundary layer air temperature and moisture content. Surface wind and stress directly affect upper-ocean mixing and, hence, entrainment of water from below the thermocline to the ocean mixed layer. All surface fluxes are parameterized in current atmospheric or ocean models because they represent turbulence exchange processes on a scale smaller than the model resolution.

In traditional stand-alone atmospheric mesoscale models, sea-surface temperatures are usually input during forecast initialization and remain fixed throughout each simulation period. For example, COAMPS received sea-surface temperature fields from the Navy Coupled Ocean Data Assimilation (NCODA) every 6 or 12 hours, as

specified in the model setup. Coupled ocean-atmosphere models use surface forcing fields at a much higher coupling frequency to improve the input to each model component. The coupling of ocean-atmosphere models allows both the atmospheric boundary layer and ocean mixed layer to evolve together. Commonly exchanged variables include surface wind stress, evaporation rate, precipitation, sensible heat flux, and latent heat flux from the atmosphere to the ocean, and sea-surface temperature from the ocean to the atmosphere.

Lebeaupin-Brossier et al. (2009) investigated various coupling frequencies for the ability of a high-resolution ocean model to simulate ocean mixed layer forcing due to strong precipitation events in the Mediterranean. This study found that with a temporal resolution finer than 3 hours, the model's ability to simulate the fine-scale structure of the OML was greatly improved. A comparison of results using coupling frequencies of 1 hour and 5 minutes found that there was little to be gained at temporal resolution finer than 1 hour because the ocean time scale is much slower than within the atmosphere.

One of the biggest challenges to coupled modeling is the coupling framework itself. Due to the historically disparate development paths of ocean and atmospheric models, the interface required to couple them is quite complex (Wen et al. 2006). The most common method is to use a coupler, which is a separate set of code that creates an interface between the two models (Zhou et al. 2004). Due to the variety of ocean and atmosphere models, as well as the importance of efficiency and accuracy in the model coupling, there is a multitude of couplers being used, such as the Climate System Model (CSM) Flux coupler (Bryan et al. 1996); the Model Coupling Toolkit (MCT; Larson et al. 2001); and the Earth System Modeling Framework (ESMF; Hill et al. 2004; Collins et al. 2005). The coupler is a Message Passing Interface (MPI) that allows variables to be exchanged without significant modification to the models themselves.

Allard et al. (2010) reported the results of the initial validation of coupled COAMPS/NCOM V. 5 for five test cases in a variety of regions. Significant changes to the prognostic quantities of wind, air temperature, and specific humidity were neither expected nor realized. However, the test cases did show improvement in the surface heat fluxes, mainly due to improvement in the sea-surface temperature. Ocean data

assimilation was only used in two of the five test cases, but the coupled NCOM sea-surface temperature without data assimilation still out-performed the sea-surface temperature from NCODA. The most significant improvements were found in regions where there were strong sea-surface temperature gradients, such as ocean eddies, or intense atmospheric forcing, such as the Adriatic bora wind. It is important to note that although there was a large number and variety of *in situ* observations for validation, few *in situ* flux measurements were available. The study relied on the comparison of fluxes estimated using the bulk method.

One further concern about coupled modeling is the additional computational time required. According to Allard et al. (2010), the increased computational time to run a fully–coupled model was estimated at 20–30% greater than that for a stand-alone atmospheric model. However, if both stand-alone ocean and atmospheric models are already required, the additional computational time is only a few percent more.

THIS PAGE INTENTIONALLY LEFT BLANK

III.   METHODS

This chapter provides an introduction to methodology used for this study. Section A gives a brief overview of the Gulf of Tehuantepec Experiment, including the time period of the field experiment and the research flights that measured the gap outflow events. The model setup is provided in Section B with details on the configuration of the uncoupled and two-way coupled model systems used for the analysis in Chapter V and evaluated in Chapter VI. Section C explains how the outflow was divided into three regions and how the aircraft low-level measurements were used to calculate the surface turbulent fluxes. The technique for calculating the heat budget of the ocean mixed layer from the NCOM simulations is presented in Section D. Finally, Section E describes the model error statistics calculated for the model evaluation in Chapter VI.

A.   THE GULF OF TEHUANTEPEC EXPERIEMENT: GOTEX

The Gulf of Tehuantepec Experiment (GOTEX) was conducted from 1 February to 1 March 2004 to study the air-sea coupling processes within the gap wind outflow over the Gulf of Tehuantepec. Using the National Center for Atmospheric Research (NCAR) C130 aircraft, eleven research flights were conducted to measure the lower atmosphere and ocean mixed layer conditions using aircraft onboard sensors, dropsondes, and airborne expendable bathythermographs (AXBT). Five gap outflow events occurred during February 2004 and were measured by nine research flights (Figure 3). Flight RF06 collected no data due to equipment malfunction, and the final flight, RF11, was flown for calibration purposes only.

GOTEX Flights February 2004
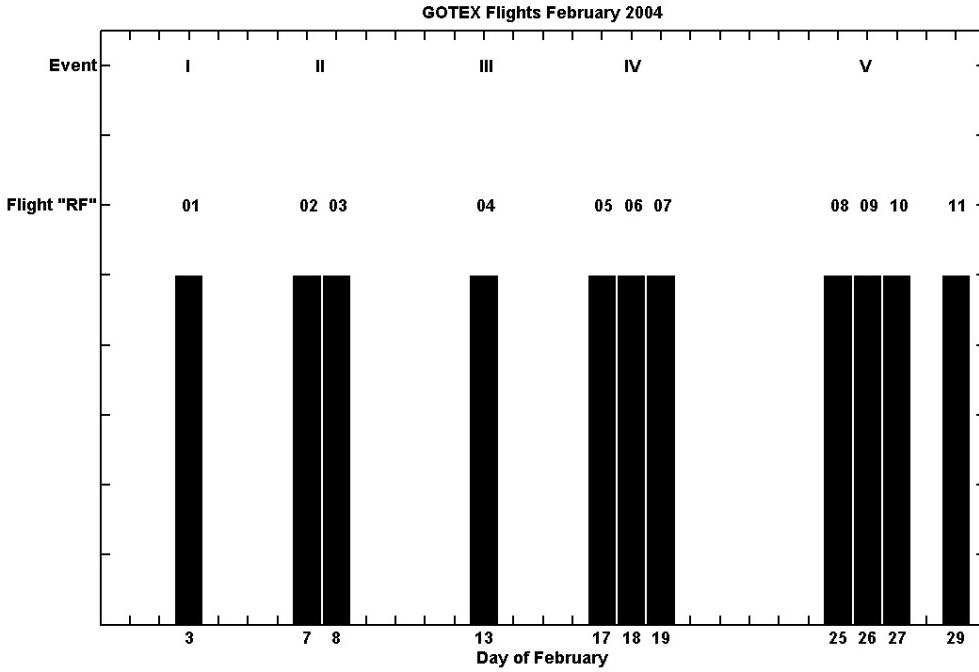
Figure 3.   Summary of date, flight number, and event number for all GOTEX flights.

The typical flight pattern consisted of a series of cross sections perpendicular to the axis of the outflow jet, beginning nearshore at the mouth of the gap exit and moving offshore, generally following the anticyclonic trajectory of the jet.   Aircraft measurements perpendicular to the outflow were sampled two ways. During Event II, the cross sections consisted of vertical stacks of level legs approximately 40–50 km long at altitudes varying from 30 m to 1200 m.   During Event V, the cross sections were measured by repeated low-level legs (30 m altitude). The cross section nearest to the coast was measured at the beginning and end of the flight on most flight days, providing temporal separation of approximately six hours.

B.   COAMPS/NCOM MODEL SETUP

The Coupled Ocean/Atmosphere Mesoscale Prediction System (COAMPS[®]) as described in Hodur (1997) is currently available in two-way coupled mode at NRL Monterey using COAMPS and the Navy Coastal Ocean Model (NCOM). COAMPS is a non-hydrostatic fully-compressible primitive-equation atmospheric model, solved

20

horizontally on a staggered Arakawa C grid and vertically on a sigma-z coordinate grid. Atmospheric boundary conditions for COAMPS V. 5 are provided by the Navy Operational Global Atmospheric Prediction System (NOGAPS) every six hours. Data assimilation is done via the NRL Atmospheric Variational Data Assimilation System (NAVDAS) on a 12-h cycle. The surface flux parameterization is a combination of Louis (1979) and the Tropical Ocean Global Atmosphere Coupled Ocean-Atmosphere Response Experiment (TOGA-COARE) bulk algorithm (Fairall et al. 2003; Wang et al. 2002). A new radiation scheme following Fu and Liou (1993) is also employed. The planetary boundary layer scheme used is described in Mellor and Yamada (1982).

The NCOM V. 4 incompressible, hydrostatic model is employed for the oceanic component. Boundary conditions are provided by global NCOM every 12 hours at 1/8 degree resolution. Data assimilation updates the NCOM state every 12 hours by the Navy Coupled Ocean Data Assimilation (NCODA) 3DVAR version. For vertical mixing, the Mellor-Yamada level 2.5 turbulence scheme is used (Mellor and Yamada 1982). NRL's two-minute resolution Digital Bathymetric Data Base (DBDB2) is used for bathymetry (Hong et al. 2012, submitted).

Simulations from the coupled COAMPS/NCOM, uncoupled COAMPS, and uncoupled NCOM for the GOTEX time period were used for this study. The GOTEX observations were not included in the data assimilation for either the atmosphere or ocean. The simulations were made with 60 vertical levels, and three nested grids in the atmosphere with an inner-nest grid spacing of 3 km (Figure 4). The NCOM grid spacing is 3 km with 50 vertical levels. The uncoupled COAMPS and NCOM are run independently with sea-surface temperature from NCODA provided to both every 12 hours. For the coupled model, COAMPS and NCOM exchange fields every 30 minutes through the Earth System Modeling Framework (ESMF). COAMPS forcing fields of wind stress, heat fluxes (solar, longwave, sensible and latent), surface evaporation, and precipitation are passed to NCOM. NCOM SST fields are passed to COAMPS. Figure 5 shows a schematic of variable exchanges for both the uncoupled and coupled model setup. Model output is hourly for surface variables and every three hours for sigma or pressure level variables. The current simulation period is from 25 January to 3 March

21

2004 to cover the entire time period of the GOTEX 2004 experiment. Hours 6 through 17 for each simulation (00 UTC and 12 UTC) are used for the evaluation to allow for initialization of each run.
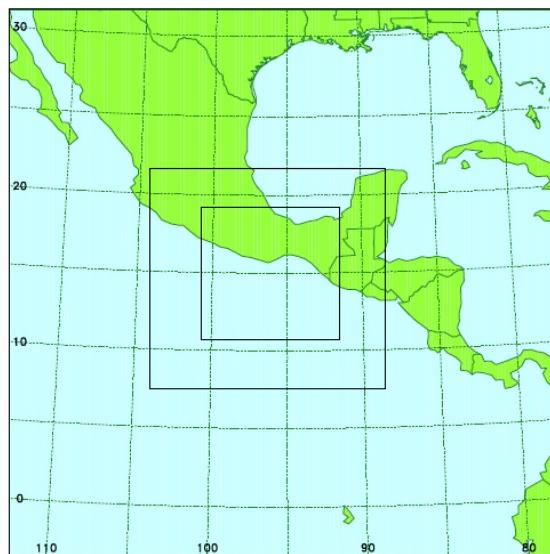
Figure 4.   Location of COAMPS domain for nests 1, 2, and 3. (Courtesy of Dr. X. Hong, NRL Monterey, 19 July 2012.)
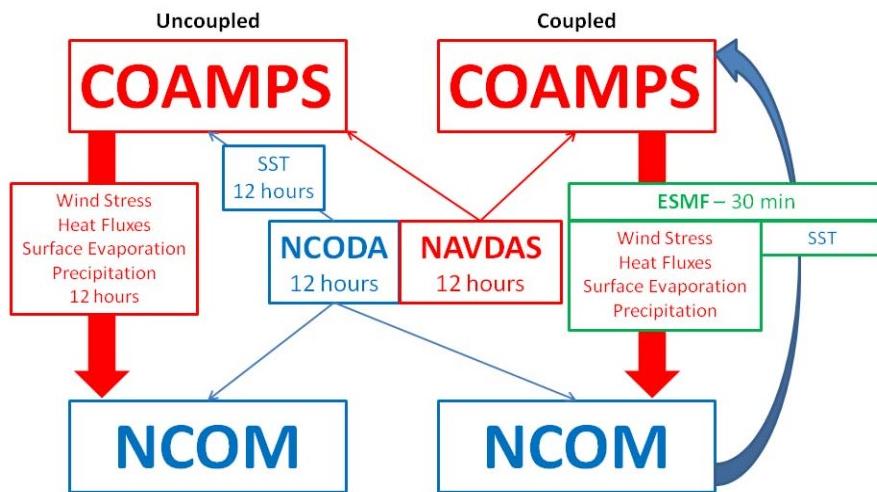
Figure 5.   Schematic of model setup for GOTEX simulations using uncoupled and coupled COAMPS and NCOM.

C.   AIRCRAFT DATA ANALYSIS

1.   Defining Different Outflow Regions

Based on a careful review of the nine successful GOTEX flights, the outflow area has been divided into three regions for analysis. The first region, the Nearshore region (NS), extends from the shoreline to the 500 m bathymetry contour (Figure 6). The initial analysis suggested a change in the magnitude of sea-surface temperature cooling and surface heat fluxes which occurred approximately 75 km from the coast. A more thorough comparison of where this change occurred during each outflow event revealed that this approximate boundary aligned with the edge of the continental shelf, making the 500 m bathymetry curve an appropriate choice for the outer boundary of the Nearshore region. This region encompasses the ocean and atmosphere above the gently sloping continental shelf which remains shallower than 500 m. The width of the Nearshore region represents the available fetch of the outflow beyond the terrain restrictions. To the west of the GoT, the width of the shelf is only 7 km. Along the axis of the gap exit at 95°W, the width of the shelf is 70 km. To the east, the shelf reaches a maximum width of 132 km at 94°W. The axis of the outflow jet is aligned with the axis of the gap exit within this region.
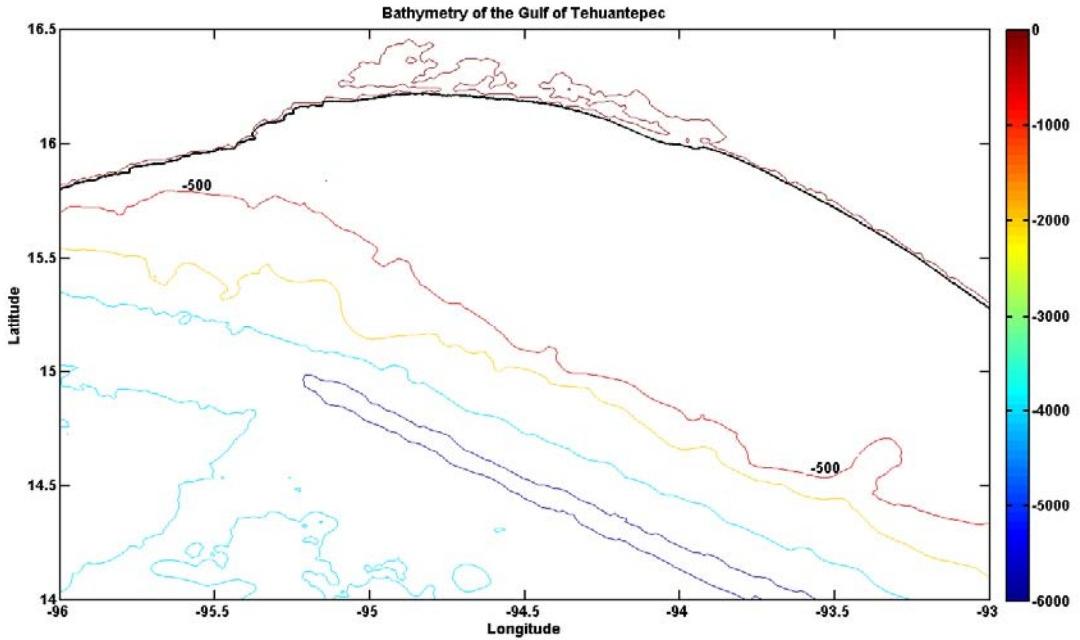
Figure 6.   Bathymetry of the Gulf of Tehuantepec at contour intervals of -500m, -2000m, -4000m, and -6000m. Gridded bathymetry at one minute resolution from David T. Sandwell, Walter H. F. Smith, and Joseph J. Becker, © 2008. The Regents of the University of California.

The second region, the Coupling Zone (CZ), extends from the 500 m bathymetry contour to the furthest offshore extent of outflow-induced cooling of sea-surface temperatures. This region is named the Coupling Zone because we hypothesize that the air-sea interactions within this region are the dominant mechanism due to strong atmospheric forcing and relatively weaker upwelling compared to the Nearshore region. The offshore boundary of this region is event dependent. For this study, the boundary was loosely determined using a criteria of ΔSST=0. Due to the spatial separation between aircraft-measured cross sections, a specific geographic boundary was not assigned. The boundary of the Coupling Zone was determined to fall between the two cross sections where ΔSST goes to zero. Beyond the 500 m bathymetry contour, the seafloor slopes dramatically down to the Middle America Trench with a maximum depth

greater than 6000 m and a width of 50 km. Offshore of the trench, the seafloor levels off at approximately 4000 m. The width of the Coupling Zone varies based on individual event conditions.

The third region, the Offshore (OFF) region, is nominally defined as the region beyond the influence of the outflow jet on the surface of the ocean. The most obvious feature of this region is the absence of significant cooling of sea-surface temperatures. Northerly winds often continue to flow over this region but the sea-surface temperature remains relatively homogenous and unchanged. Figure 7 shows the SST variability from the COAMPS surface temperature field to illustrate the three zones within the outflow.
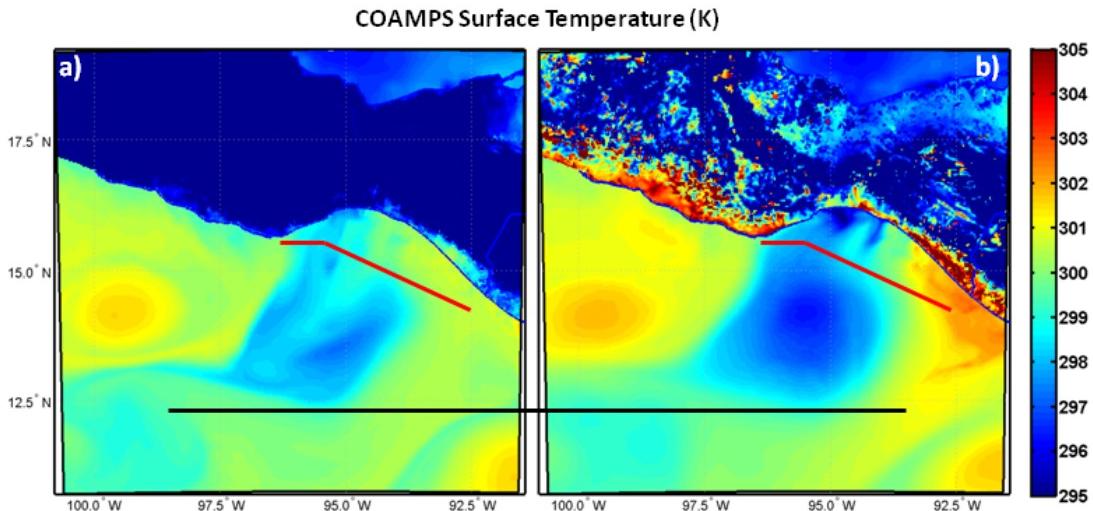
Figure 7.   The COAMPS surface temperature fields from a) 1500 UTC, 7 February 2004 and b) 2200 UTC, 8 February 2004. The red lines denote the approximate boundary between the NS and CZ regions. The black line denotes the approximate boundary between the CZ and OFF regions.

2.   Analysis of Observations

The aircraft track for each flight was divided into level legs and sounding legs. Level legs were identified during any non-turning, level flight leg, with minimal altitude variations. Sounding legs were identified for any aircraft ascent or descent. Turning ascent and descent legs were used for temperature and moisture profiles only because these aircraft maneuvers normally result in unreliable wind measurements.

25

Measurements from onboard aircraft sensors, as well as aircraft-launched dropsondes and AXBTs, were used in this analysis. The variables measured from onboard aircraft sensors are summarized in Table 1. Additional details are described in the NCAR EOL C-130 Investigator Handbook, Chapter 6 (NCAR EOL, 2012). The average spatial sampling intervals based on mean aircraft speed (107.6 m s^{-1}) was 4.3 m, 21.5 m, and 107.6 m at 25 Hz, 5 Hz, and 1 Hz, respectively.

Table 1.   Aircraft-measured variables from the NSF/NCAR C-130 aircraft used for this study. This list does not include all variables measured during the GOTEX experiment. Additional information is available in the NCAR EOL C-130 Investigator Handbook [Available at http://www.eol.ucar.edu/instrumentation/aircraft/C-130/documentation/c-130-investigator-handbook/c-130-investigator-handbook/.]

Aircraft Measured Variable	Instrument	Frequency (Hz)	Redundancy
Ambient Air Temperature	Infrared Thermometer	25	Y
Dew Point Temperatire	Thermoelectric Hygrometer	25	N
GPS Geopotential Altitude	GPS Navigational Sensor	1	Y (APN)
Geometric (radar) Altitude	APN-232	5	Y (GPS)
Infrared Irradiance	Pyrgeometer	25	Y
Latitude	GPS Navigational Sensor	1	Y (INS)
Longitude	GPS Navigational Sensor	1	Y (INS)
Mixing Ratio	Lyman-alpha and T-electric	25	Y
Relative Humidity	Lyman-alpha	25	N
Absolute Humidity	Lyman-alpha	25	N
Surface Temperature	Radiometer	5	Y
Sky/ Cloudbase Temperature	Radiometer	5	Y
Shortwave Irradiance	Pyranometer	25	Y
True Aicraft Speed	Inertial Navigation System	25	Y (GPS)
Track Angle (Aircraft Heading)	Inertial Navigation System	25	Y (GPS)
UIC, VIC Horizontal Wind Vectors	GPS-corrected	25	Y (INS)
WIC Vertical Wind Vector	GPS-corrected	25	Y (INS)

Momentum and heat fluxes were calculated from 25 Hz aircraft measurements using the eddy-correlation or covariance method. Using a moving window of 5 km, mean and covariance were computed for each segment of data to provide the vertical kinematic eddy fluxes of heat, moisture and momentum. Aircraft measurements along level legs were decomposed into the mean and perturbation time series. To calculate fluxes from the perturbations, a 5 km moving average was used which corresponds to a

time average of approximately 50 seconds given an average aircraft speed of 107.6 m s^{-1}, similar to previous studies using low-level aircraft flux measurements (Friehe et al. 1991; Li et al. 1989). Once the kinematic eddy fluxes were calculated, the surface fluxes of momentum, sensible heat (Q_H), latent heat (Q_E) and turbulent kinetic energy (TKE) were calculated by

$$Q_H = \rho C_p \left(\overline{w'\theta'} \right) \tag{1}$$

$$Q_E = \rho L_v \left(\overline{w'q'} \right) \tag{2}$$

$$TKE = \frac{1}{2} \left(\overline{u'u'} + \overline{v'v'} + \overline{w'w'} \right) \tag{3}$$

where ρ is the density of air, C_p is the specific heat of air, and L_v is the latent heat of vaporization (Stull 1988). Although the eddy-correlation method is considered an improvement to the fluxes estimated using the bulk method, there are some potential errors in this approach. For the high-frequency measurements to truly represent the turbulent fluxes at the surface, the measurements must be made within the surface layer, where fluxes vary by less than 10%. The low-level GOTEX measurements were made at approximately 30 m, which is generally within the surface layer during given that the measured boundary layer heights were mostly deeper than 300 m. However, there may be occasionally shallower boundary layers in the Coupling Zone region that violate the surface layer assumption. The error in calculating turbulent fluxes from the eddy correlation method is in general less than 10%.

D. CALCULATION OF THE OCEAN MIXED LAYER AND ITS HEAT BUDGET

To better understand the mechanisms responsible for the dramatic cooling of sea-surface temperatures, the heat budget of the ocean mixed layer was calculated from the coupled NCOM simulations. GOTEX AXBTs measured a highly stratified ocean. In several AXBT profiles, there was no well-mixed layer, due to upwelling raising the thermocline to the ocean surface. Details of the observed ocean structure will be presented in Chapter IV. However, because of these observations, the definition of the

mixed layer was chosen using potential density rather than sea temperature. Potential density (σ_θ) is the density of a fixed parcel of water moved adiabatically to a given reference pressure, p_r, usually 1 bar, and is a function of salinity and potential temperature.

Initially, the mixed layer depth (MLD) in the model simulations was found using a threshold of $\Delta\sigma_\theta = 0.01\,\mathrm{kg}\ \mathrm{m}^{-3}$ from the surface potential density (Thomson and Fine 2003). However, this threshold resulted in anomalously shallow MLD values as illustrated by the black points in Figure 8. Since the calculation of the heat budget hinges on quantifying the heating and cooling within the mixed layer and analysis of NCOM profiles of temperature, salinity and potential density revealed a deeper mixed layer than diagnosed using the original threshold, the utility of different $\Delta\sigma_\theta$ thresholds was examined. Eighty randomly selected locations within the GOTEX domain, over an 84 hour time period, were analyzed and the MLD was manually selected based on a comparison of temperature, salinity and potential density profiles. Then, the MLD was calculated for each location and simulation time using $\Delta\sigma_\theta$ thresholds of 0.01, 0.05, 0.10, and 0.15 kg m^{-3}. The results are shown in the scatter plot in Figure 8. The correlation coefficients between the manually selected MLD and calculated MLD were 0.61, 0.85, 0.958, and 0.955 for 0.01, 0.05, 0.10, and 0.15 kg m^{-3}, respectively (N=2240). Based on the high correlation coefficient and the distribution pattern in Figure 8, $\Delta\sigma_\theta = 0.10$ kg m^{-3} was selected as the defining criterion for mixed layer depth in this study.
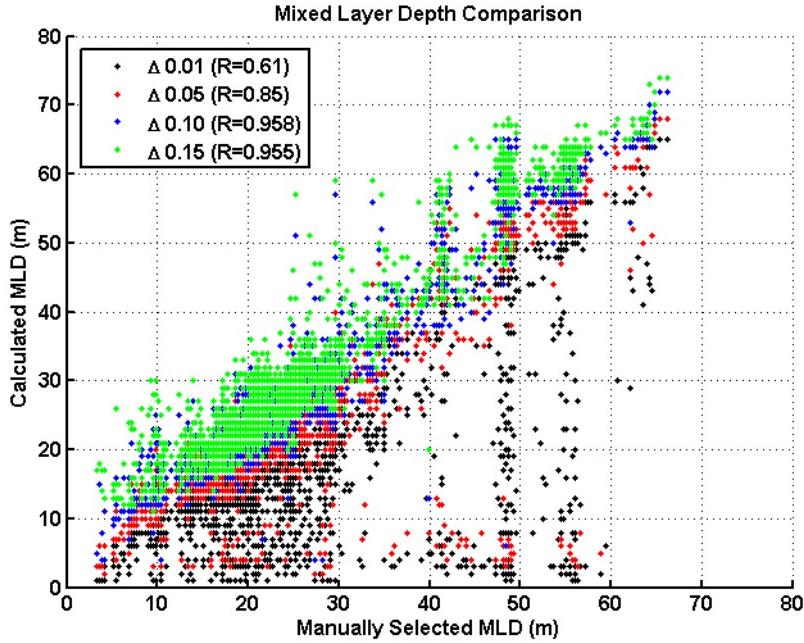
Figure 8. Scatter plot of manually selected MLD (m) vs. calculated MLD (m) according to the following thresholds of $\Delta\sigma_\theta$: 0.01kg m^{-3} (black), 0.05 kg m^{-3} (red), 0.10 kg m^{-3} (blue), and 0.15 kg m^{-3} (green). The correlation coefficients are provided in the legend.

The heat budget of the ocean mixed layer can be described by

$$\frac{\partial \overline{T}}{\partial t} = -\left(\overline{u} \frac{\partial \overline{T}}{\partial x} + \overline{v} \frac{\partial \overline{T}}{\partial y} \right) - w \frac{\partial T}{\partial z} + Q - \frac{\partial \left(\overline{w'T'} \right)}{\partial z} \tag{4}$$

where the heating rate in the mixed layer is equal to the sum of the horizontal advection, the vertical advection, the solar heat-flux divergence, and the heat-flux divergence (Kundu and Cohen 2008). Although our definition of the mixed layer depth uses potential density and not temperature, we will assume that for the heating rate and horizontal advection terms, the temperature gradient is small and therefore, we can use the mean temperature in the mixed layer ($\overline{T}$) for the time derivative and horizontal gradients. Similarly for the horizontal advection, the mean zonal and meridional current speeds in the mixed layer are used ($\overline{u}, \overline{v}$).

The second term on the right hand side represents the vertical advection which is often completely attributed to upwelling due to Ekman transport near the coast and

29

Ekman pumping in the open ocean. However, the offshore wind in the GoT results in offshore ageostrophic currents, rather than pure Ekman transport (90° to the right of the wind stress in the Northern Hemisphere) as is the case with alongshore flow. The vertical velocity, w, was diagnosed from the mass conservation, or continuity, equation where

$$\frac{\partial \rho}{\partial t} + \vec{\nabla} \cdot \left(\rho \vec{u} \right) = 0 \tag{5}$$

Since NCOM is an incompressible, hydrostatic model, we can make the simplification that

$$\frac{\partial w}{\partial z} + \frac{\partial u}{\partial x} + \frac{\partial v}{\partial y} = 0 \tag{6}$$

Integrating the continuity equation with respect to z over the depth of the mixed layer, we calculated w_{-h} as

$$w_{-h} = -h * \left(\frac{\partial u}{\partial x} + \frac{\partial v}{\partial y} \right) \tag{7}$$

where h is the mixed layer depth. Because we used potential density as the MLD criterion, we calculate $\frac{\partial T}{\partial z}$ in the mixed layer and multiply by the vertical velocity calculated using Equation 7 to find the vertical advection.

The solar heat-flux divergence represents the heating to the ocean mixed layer from solar flux at the surface and that absorbed within the mixed layer. Solar radiation is absorbed quickly within the water column, decreasing exponentially with depth. The solar flux divergence was calculated using the solar flux output from NCOM and a function (γ) of the solar extinction (Martin 2000).

$$Q = -\frac{1}{\rho_w C_{p_w}} Q_r \frac{\partial \gamma}{\partial z} \tag{8}$$

The solar extinction function from Paulson and Simpson (1977) was differentiated with respect to depth to yield

30

$$\frac{\partial \gamma}{\partial z} = \frac{R}{\zeta_1} e^{\frac{z}{\zeta_1}} + \frac{1}{\zeta_2} \left[(1-R) e^{\frac{z}{\zeta_2}} \right] \qquad (9)$$

Coefficients of R, ζ_1, and ζ_2 are given for a variety of ocean types and represent the turbidity of the water (Jerlov 1968). The Gulf of Tehuantepec is classified as Type II, which was the input parameter for the NCOM simulations. For a Type II ocean, R is 0.77; ζ_1 is 1.5m; and ζ_2 is 14 m. For the solar flux divergence, $\frac{\partial \gamma}{\partial z}$ was calculated at each depth within the mixed layer and multiplied by $\frac{Q_r}{\rho_w C_{p_w}}$, then integrated over the depth of the mixed layer to calculate the heating rate due to divergence of solar radiative flux divergence, Q.

The last term in the heat budget equation represents the divergence of turbulent heat flux in the ocean mixed layer. For an upper-ocean well-mixed in temperature, one can calculate the mixed layer flux divergence using the surface heat flux and entrainment flux at the bottom of the mixed layer:

$$-\frac{\partial \left(\overline{w'T'} \right)}{\partial z} = -\left(\frac{\left(\overline{w'T'} \right)_0 - \left(\overline{w'T'} \right)_h}{h} \right) \qquad (10)$$

where surface heat flux can be related to sensible heat flux (Q_H), latent heat flux (Q_E), and longwave flux (Q_L) in the atmosphere. In our budget analysis, the heat-flux divergence was calculated as the residual from the heat budget equation. The heating rate from the surface heat flux was calculated as

$$\left(\overline{w'T'} \right)_0 = \frac{1}{\rho_w C_{p_w}} * \left(Q_H + Q_E + Q_L \right) \qquad (11)$$

using the NCOM net heat flux at the ocean surface. The residual heating, which includes the entrainment heating rate at the bottom of the mixed layer and any inherent error, was calculated by

$$-residual = -\frac{\partial \overline{T}}{\partial t} - \left(\overline{u} \frac{\partial \overline{T}}{\partial x} + \overline{v} \frac{\partial \overline{T}}{\partial y} \right) - w \frac{\partial T}{\partial z} + Q - \frac{\left(\overline{w'T'} \right)_0}{h} \qquad (12)$$

It is assumed that the entrainment heating/cooling rate at the base of the mixed layer dominates the residual term. Heat budget calculations are presented in Chapter V.

E.   ANALYSIS OF MODEL RESULTS

To compare fully-coupled COAMPS/NCOM to the aircraft observations, COAMPS and NCOM variables were interpolated in space and time to the latitude, longitude, altitude/depth, and time of the measurement. For each level aircraft leg, COAMPS and NCOM variables were interpolated in time to the mean time of the level leg. Approximately 41,000 model-observation pairs were used for the surface variables, and 103,000 pairs for the sigma-level variables.

Statistical calculations for the observation-model pairs provide a measure of error and comparison of overall model performance. First, the traditional root mean square error (RMSE) was calculated for each variable as defined by

$$RMSE = \sqrt{\frac{1}{N} \sum_{n=1}^{N} \left(f_n - r_n \right)^2} \qquad (4)$$

where f_n represents the interpolated model value, r_n represents the observed value, and N is the total number of observation-model pairs (Wilks 1995).

To gain an understanding of how the ocean-atmosphere coupling affected the model performance, the remaining statistical analysis followed Taylor (2001). Statistics were calculated for wind speed, wind stress, potential temperature, sea-surface temperature, sensible heat flux, specific humidity, latent heat flux, turbulent kinetic energy, and the air-sea temperature difference (T_s-T_a). The overall bias ($\overline{E}$) was calculated by subtracting the observed mean from the model mean (Equation 5) to calculate the centered pattern RMS difference ($RMSE_C$, Equation 6), where f_n and $\overline{f}$ represent the nth interpolated model value and the mean of the interpolated model values,

32

respectively, and r_n and $\bar{r}$ represent the n$^{\text{th}}$ observation and the mean of the observations, respectively.

$$\bar{E} = \bar{f} - \bar{r} \tag{5}$$

$$RMSE_C = \sqrt{\frac{1}{N} \sum_{n=1}^{N} \left[\left(f_n - \bar{f} \right) - \left(r_n - \bar{r} \right) \right]^2} \tag{6}$$

The centered pattern RMS difference gives the error in the perturbations about the mean. The perturbation patterns become more similar as $RMSE_C$ approaches zero. Finally, the correlation coefficient, R, is calculated by

$$R = \frac{\dfrac{1}{N} \sum_{n=1}^{N} \left(f_n - \bar{f} \right) \left(r_n - \bar{r} \right)}{\sigma_f \sigma_r} \tag{7}$$

where σ_f and σ_r represent the standard deviation of the model and observations, respectively. To summarize the model performance for all variables, a normalized Taylor diagram was constructed and is presented in Chapter VI. Taylor (2001) consolidates the statistical measures into a single diagram. The values are normalized according to

$$RMSE_{CN} = \frac{RMSE_C}{\sigma_r} \tag{8}$$

$$\hat{\sigma}_f = \frac{\sigma_f}{\sigma_r} \tag{9}$$

$$\hat{\sigma}_r = 1 \tag{10}$$

where $RMSE_{CN}$ and $\hat{\sigma}_f$ represent the normalized centered RMS difference and the normalized model standard deviation, respectively. The normalized observation standard deviation is represented by $\hat{\sigma}_r$. To construct the Taylor diagram, the normalized standard deviation of the observations ($\hat{\sigma}_r = 1$) is plotted on the x-axis and represents all of the observations. The position for each variable is assigned by the value of the normalized standard deviation ($\hat{\sigma}_f$) on the y-axis and the value of the correlation

coefficient, R, on the azimuthal axis. The radial separation between the model point and the observation point represents the normalized centered pattern RMS difference ($RMSE_{CN}$). For the comparison presented in Chapter VI, the coupled and uncoupled statistical values are plotted together. Further explanation will be provided in Chapter VI.

IV. OBSERVED EVOLUTION OF THE ATMOSPHERIC BOUNDARY LAYER AND OCEAN MIXED LAYER

Although the Gulf of Tehuantepec gap outflow has been the subject of numerous observational case studies, this study provides new information that augments the findings from previous studies. Because of the high mobility of a research aircraft, GOTEX provided high-resolution, low-level sampling of the boundary layer with greater spatial and temporal coverage throughout multiple stages of five gap outflow events. The use of this data set makes the current study unique as previous observational studies relied on data sets that covered a smaller geographic area within the outflow, did not provide temporal sampling of the event during different stages, or did not have co-located measurements in the atmosphere and ocean. Additionally, few studies were based on surface fluxes calculated using the direct eddy-correlation method in different regions of the gap outflow. Instead, surface stress and heat fluxes were derived from the bulk formulation. Although the bulk aerodynamic formulations are accurate to a certain extent (Fairall et al. 2003), they are not ideal in the GoT region during the Tehuano events for two reasons. First, the bulk aerodynamic formulation in high wind regimes, as seen in GoT outflow events, have not been tested with sufficiently high-frequency measurements. Secondly, the oceanic response in the GoT region is highly dependent on the 'coupling' factors, which are the momentum and heat fluxes. It is essential to have reliable surface fluxes for better accuracy in estimating upper-ocean response.

During GOTEX, a total of five gap outflow events were sampled by ten C-130 flights. Two of these events were measured by two flights on successive days. These two events, Events II and V, will be the focus of our analysis to further our understanding of the development and evolution of the MABL during a gap outflow event. Figure 9 shows the flights tracks, dropsonde, and AXBT locations for these two events. Figure 9a shows the flight track and instrument locations for flights RF02 and RF03, measured 24 hours apart during Event II. Figure 9b shows the flights during Event V, RF09 and RF10, also flown 24 hours apart. RF08 was flown 24 hours prior to RF09 before the onset of Event V. The RF08 flight track was perpendicular to the coast, along 95°W (not

shown). AXBTs and dropsondes were not launched during this flight. The zones described in Chapter III are shown for both events in Figure 9. The Nearshore region spans from the coast to the dashed black line representing the 500 m bathymetry curve. The green line shows the approximate location of the boundary between the Coupling Zone and the Offshore region for each event.
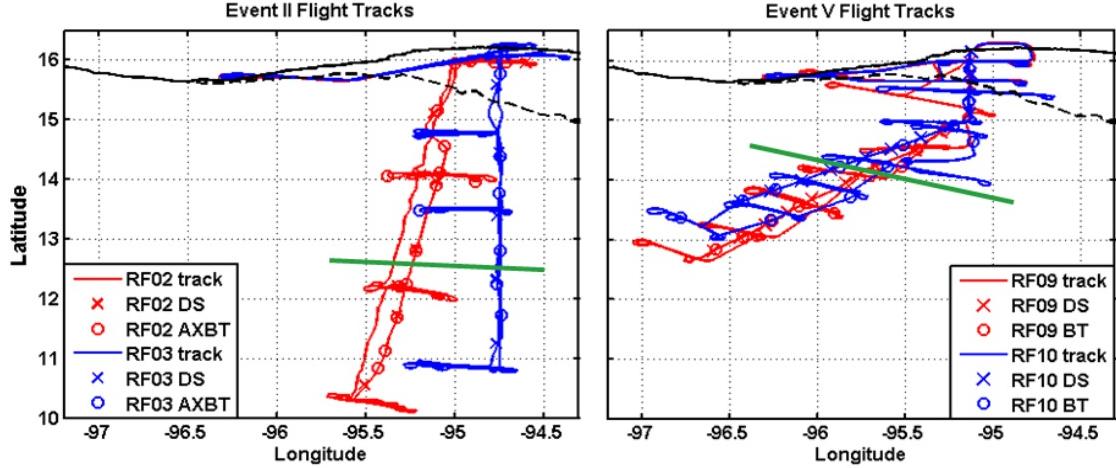
Figure 9.   Flight tracks for Events II and V. a) RF02 flight track, dropsondes, and AXBTs are shown in red. RF03 flight track, dropsondes, and AXBTs are shown in blue. b) RF09 flight track, dropsondes, and AXBTs are shown in red. RF10 flight track, dropsondes, and AXBTs are shown in blue. The black dashed line is the 500 m bathymetry contour which represents NS/CZ boundary. The green line shows the approximate boundary of the CZ/OFF region for each event.

In the following sections, we will discuss each event separately, beginning with the downwind development of the atmospheric boundary layer, then the temporal evolution of the atmospheric boundary layer, and finally, the evolution of the ocean mixed layer. A summary is given at the end of this chapter to discuss the common characteristics observed from both events.

A.   EVENT II: 6–10 FEBRUARY 2004

The first case study is GOTEX Event II, which occurred from 6–10 February 2004. It was measured by flights RF02 and RF03 approximately 21 hours and 45 hours after event onset, respectively (Figure 10). The time series of COAMPS surface wind stress is shown in Figure 10 for a point at 50 km offshore along the axis of the gap exit.

The timing of flights RF02 and RF03 with respect to the event are shown by the red and blue shaded bars, respectively. Based on QuikSCAT surface winds and COAMPS simulations (not shown), the northerly gap winds began at approximately 1800 UTC on 6 February 2004. By the beginning of RF02, at 1500 UTC 7 February 2004, northerly winds flowed over the entire GoT, with winds stronger than 20 m s^{-1} reaching greater than 350 km from the coast, as shown in the vertical cross section of dropsonde-measured wind speed (Figure 18a, shown in section A.2). The gap outflow continued to develop and strengthen for approximately 33 hours, weakening by 0300 UTC on 8 February 2004, before the beginning of flight RF03. The gradually weakening northerly winds persisted through the gap and Nearshore region until 11 February 2004, as seen in both QuikSCAT observations (not shown) and model simulations (Figure 10).
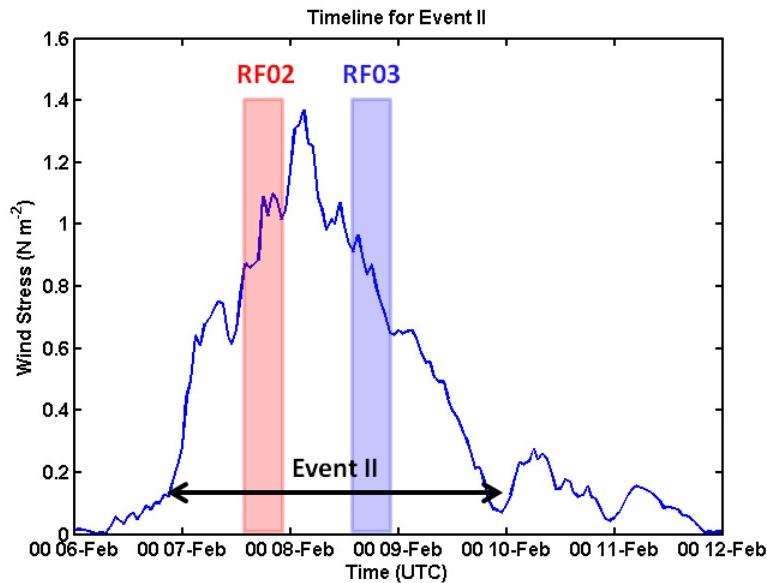
Figure 10.   Time series of COAMPS wind stress (N m^{-2}) during Event II, 50 km offshore along 95°W. Event duration and flight times for RF02 and RF03 are identified.

In the following sections, we will first discuss the downwind development of the outflow jet and its associated boundary layer development during the first flight (RF02) using all available measurements from onboard aircraft sensors and expendable instruments. The time evolution of the outflow will be discussed using measurements from both RF02 and RF03. The evolution of the ocean mixed layer will be discussed

37

using AXBTs from flights RF02 and RF03. Aircraft soundings from the ascents and descents will be compared along with dropsonde profiles to study the vertical structure of the boundary layer.

Each flight consisted of roughly longitudinal level legs at varying altitudes between 30 m and 1600 m above mean sea level. Each group of level legs will be referred to as a vertical stack (VS). Turbulence mean, fluxes, and variance were derived from these level legs. Results from legs at different altitudes give coarse vertical profiles of statistical quantities, but are representative of the mean conditions at the location of the measurement region. The location of the vertical stacks (VS, red), aircraft soundings (S, black), dropsondes (DS, blue), and AXBTs (BT, green) for RF02 are shown in Figure 11.
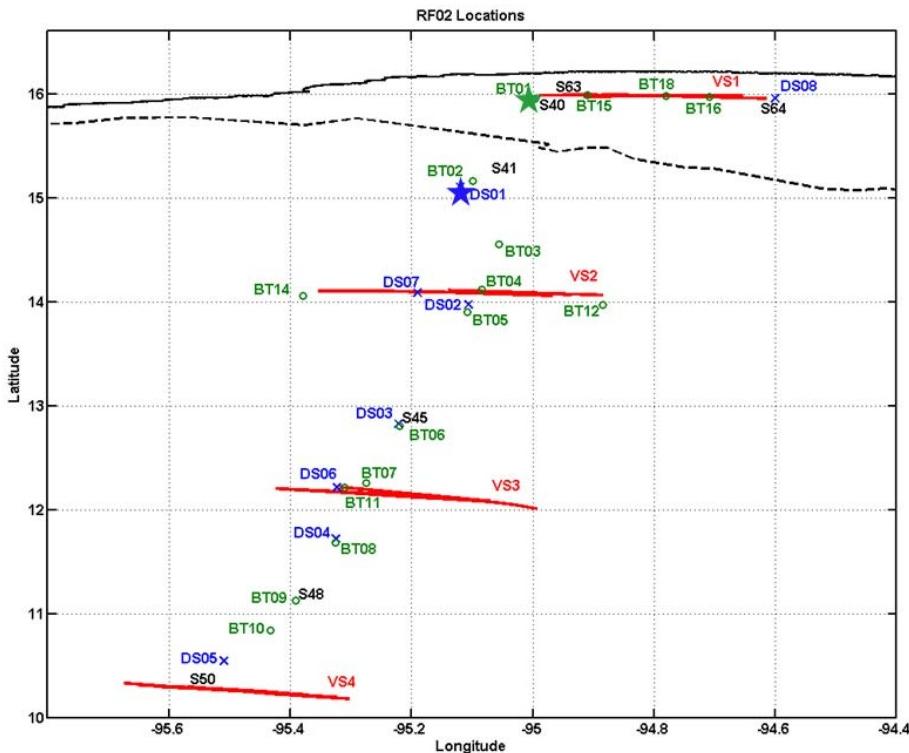
Figure 11.   Locations of aircraft measurements during RF02. Vertical stacks of level legs are shown in red and labeled VS. Aircraft soundings are shown in black and labeled S. The location of the label is the center point of the ascent/descent leg. Dropsonde locations are shown in blue and labeled DS. The blue star denotes the start of the dropsonde cross section shown in Figure 18a. The AXBTs are shown in green and labeled BT. The green star denotes the start of the AXBT cross section shown in Figure 28a.

1. Downwind Development of the Atmospheric Boundary Layer

A general overview of the downstream boundary layer development is shown in Figures 12 and 13 using measurements from the four vertical stacks, one in the Nearshore region (VS1), one in the Coupling Zone (VS2), and two in the Offshore region (VS3 and VS4). It is clear that the strongest winds occurred in the Nearshore and Coupling Zone regions with significant wind shear in the lower 200 m of the boundary layer (Figure 12a). The Nearshore wind jet seemed to have a deep jet core, with the peak between 200–400 m with a mean wind speed of nearly 30 m s^{-1} and only showed a small decrease at the next altitude of 775 m. The Coupling Zone had weaker wind near the surface but may have similar magnitude higher above as seen from the measurement at 450 m. Weak low-level wind shear still existed in VS3, within the Offshore region, but diminished farther downwind (VS4, Figure 12a). The profiles of wind stress (Figure 12c) and TKE (Figure 12d) are consistent with turbulence and wind stress generated by wind shear in the lower 200 m of the boundary layer. Both stress and TKE decrease significantly above the shear layer with no systematic difference among the three regions.
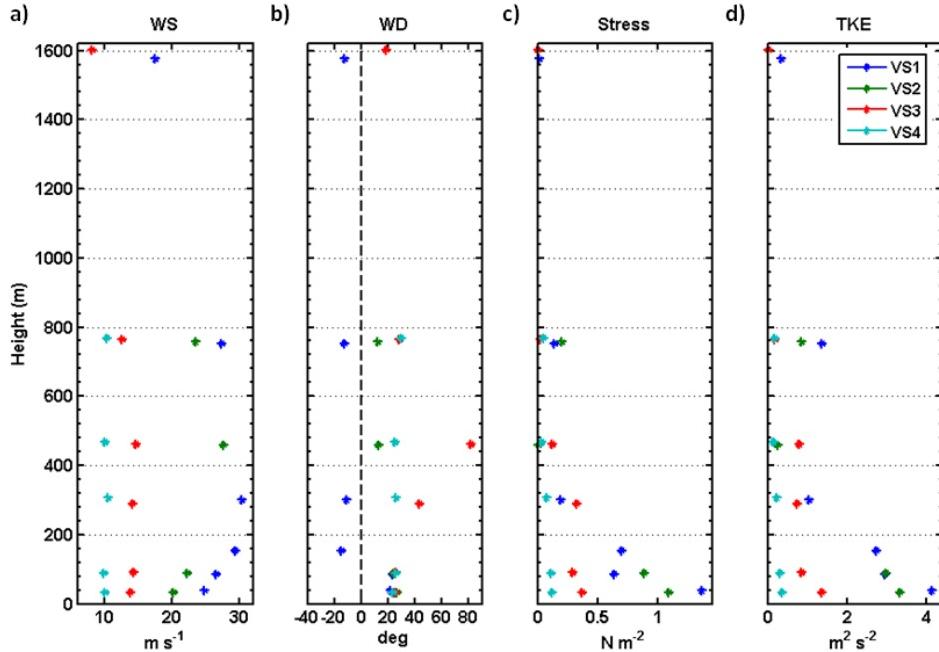
Figure 12. Mean values of a) wind speed (m s^{-1}), b) wind direction (deg), c) wind stress (N m^{-2}), and d) TKE (m^2 s^{-2}) plotted at the mean altitude of the aircraft level leg.

The mean potential temperature in the jet core warmed gradually toward the open ocean from VS1 to VS4 (Figure 13a), with all vertical stacks showing a vertically well-mixed boundary layer. The low-level water vapor specific humidity also showed gradual moistening downstream (Figure 13c). While the Nearshore and Offshore mean moisture profiles showed a gradual decrease in height within the upper boundary layer above 450 m (VS1, VS3 and VS4), the Coupling Zone region had a much sharper decrease above the lowest 200 m (VS2). This drier upper layer was also seen clearly in the dropsonde measurements to be discussed later.

Sensible heat flux (Figure 13b) showed the most dramatic change across the three regions. In the Nearshore region (VS1), negative heat flux of -30 to -20 W m^{-2} was measured near the surface up to 311 m. Calculating the sensible heat-flux divergence within the boundary layer, similar to Equations 10 and 11, the cooling rate at VS1 can be estimated from the mean sensible heat flux values at 30 m and 175 m. The flux divergence indicates a cooling rate of about 4 K day^{-1} for the atmospheric boundary layer by turbulent flux transport. Indeed, the vertical mean potential temperature profiles (Figure 13a) showed weak stable stratification in the lower layer that was associated with the negative heat flux throughout the lower 300 m of the boundary layer. From the COAMPS simulations of 10 m potential temperature (discussed in Chapter V), the typical magnitude of diurnal warming within the Nearshore region was 2 K during GOTEX. With an estimated cooling rate of 4 K day^{-1} due to turbulent flux transport and a warming rate of 2 K day^{-1} due diurnal warming of advected boundary layer air, an additional 2 K of cooling within the Nearshore region is expected for RF03. In fact, the early vertical profiles from RF03 (blue in Figure 21) show an additional cooling of approximately 2 K.

The negative sensible heat flux at the surface (30 m above the surface) also suggests heating of the upper-ocean by sensible heat flux from the atmosphere to the ocean. In the Coupling Zone and the shoreward vertical stack (VS3) of the Offshore region, sensible heat fluxes were measured to be 25 W m^{-2} near the surface, while the flux weakened to nearly zero in the far Offshore region (VS4). The three regions of the gap outflow thus have very different near-surface thermal stability: stable Nearshore,

unstable in the Coupling Zone region and the adjacent Offshore region, and weakly unstable or near-neutral in the far Offshore region.

Large latent heat flux was measured throughout the outflow region, but with significant variability (Figure 13d). The largest air-sea moisture exchange happened in the unstable region, averaging to 400 W m^{-2} (VS2 and VS3), and the smallest flux was in the far Offshore region. The Nearshore and Coupling Zone regions should therefore have seen large moistening from the turbulence flux convergence (Figure 13d). For these two regions, a rough estimate of the moistening rate ($\frac{\partial q}{\partial t}$) using moisture flux measurements in the lowest 200 m gives estimates of 24 and 31 g kg^{-1} day^{-1} for VS1 and VS2, respectively.

Using the gradient derived from the q_v difference between VS1 and VS2 and the mean wind speed of approximately 30 m s^{-1}, we estimate a moistening rate of approximately -26 g kg^{-1} day^{-1} by horizontal advection, about the same magnitude of drying due to horizontal advection as the moistening from turbulence flux convergence. Thus, dry air advection and turbulent mixing are the two dominant processes, with opposite sign and similar magnitude. Therefore, we do not expect significant variation of boundary layer moisture with time during the gap outflow event. It is seen from the measurements from the following day (RF03, to be shown later) that specific humidity indeed remained similar 24 hours later.
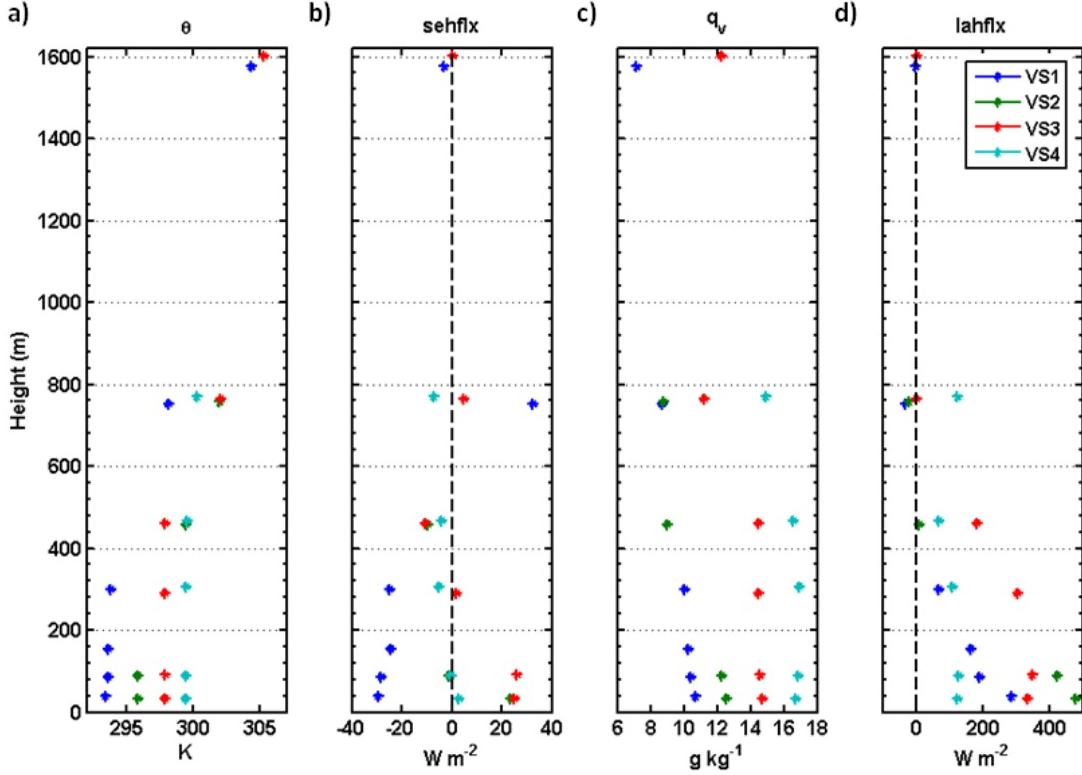
Figure 13.   Mean values of a) potential temperature (K), b) sensible heat flux (W m^{-2}), c) specific humidity (g kg^{-1}) and d) latent heat flux (W m^{-2}) plotted at the mean altitude of the aircraft level leg.

a.   The Nearshore Region

Within the Nearshore region, in addition to the vertical stacks discussed earlier, there are also three aircraft soundings and one dropsonde (S40, S63, S64, and DS08, see Figure 11) that can be used to show the vertical structure and the variability from the jet core to the east within this region. Aircraft sounding S40, at the axis of the gap exit, measured a weakly stable atmospheric boundary layer, consistent with results from VS1 (Figure 14). Here, wind speed increased continuously until the top of S63, another aircraft sounding at the jet axis reaching 36 m s^{-1} at about 800 m. DS08 and S64 were measured 41 km to the east of the axis of the jet core axis (Figure 14). Here the soundings showed a slightly weaker wind speed maximum of 28.7 m s^{-1} at 276 m, indicating that the sounding location was towards the edge of the jet core.
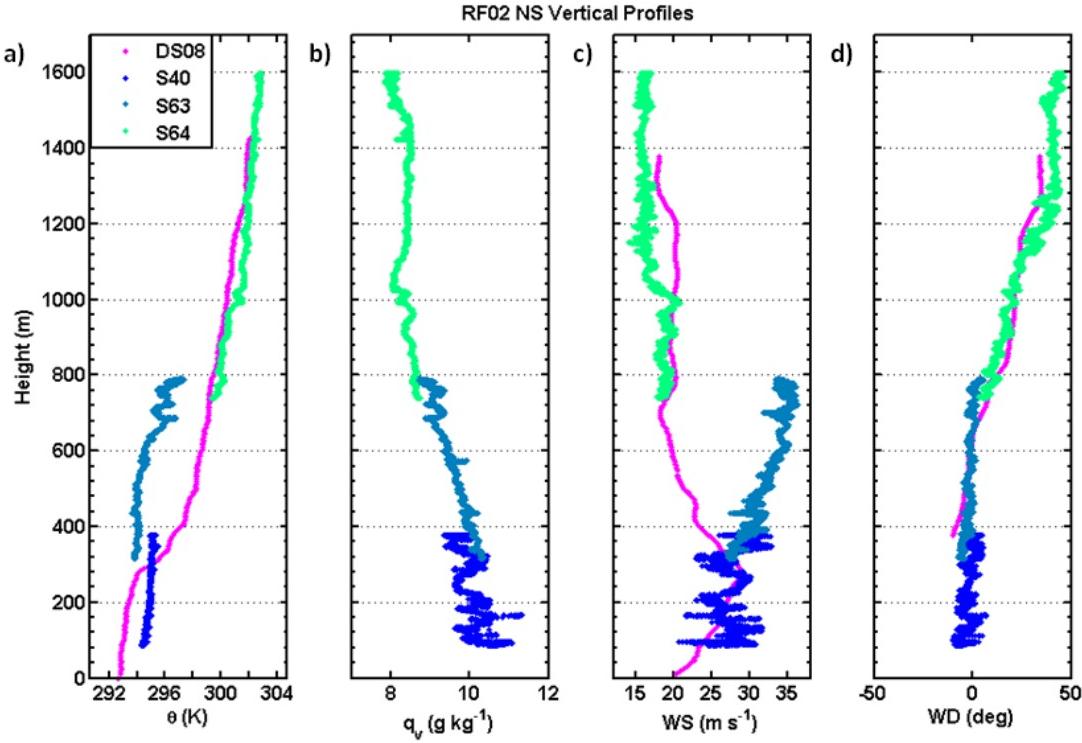
Figure 14. RF02 Nearshore vertical profiles of a) potential temperature (K), b) specific humidity (g kg^{-1}), c) wind speed (m s^{-1}), and d) wind direction (deg).

b. *The Coupling Zone Region*

The Coupling Zone for RF02 extended from 76 km offshore at the edge of the shelf, south to 400 km offshore, shown in Figure 9 as the region between the black dashed line and solid green line. The southern boundary of the Coupling Zone, at 12.7°N, was marked by a 1.6 K increase in sea-surface temperature (Figure 24, in section A.3). Aircraft measurements for this region include four dropsondes, eleven soundings, and a vertical stack (VS2) of four 48 km-level level legs from altitudes of 45 m to 750 m, located along 14.1°N. For figure clarity, only the profiles referred to in this section are shown in Figure 15.

The soundings and dropsondes showed an elevated jet maximum with vertical shear above and below (Figure 15). The elevation and strength of the jet core decreased away from shore. From 15.2°N southward 244 km (S41 to S45 and DS03), the jet maximum decreased in wind speed from 37 m s^{-1} to 25 m s^{-1} and the jet core altitude

43

dropped from 720 m to approximately 540 m. The height of the wind speed maximum correlated with the level of strong stable stratification in potential temperature and specific humidity, which is representative of the boundary layer top. DS03 showed that the boundary layer was warmer and moister toward the offshore edge of the Coupling Zone region. Vertical profiles at the outside edges of VS2 (48 km apart) showed little horizontal variability, which indicate that VS2 was contained within the jet core (not shown). In the Coupling Zone, the wind direction shifted slightly from N to NE as expected from previously documented anticyclonic turning of gap outflow jets in the GoT.
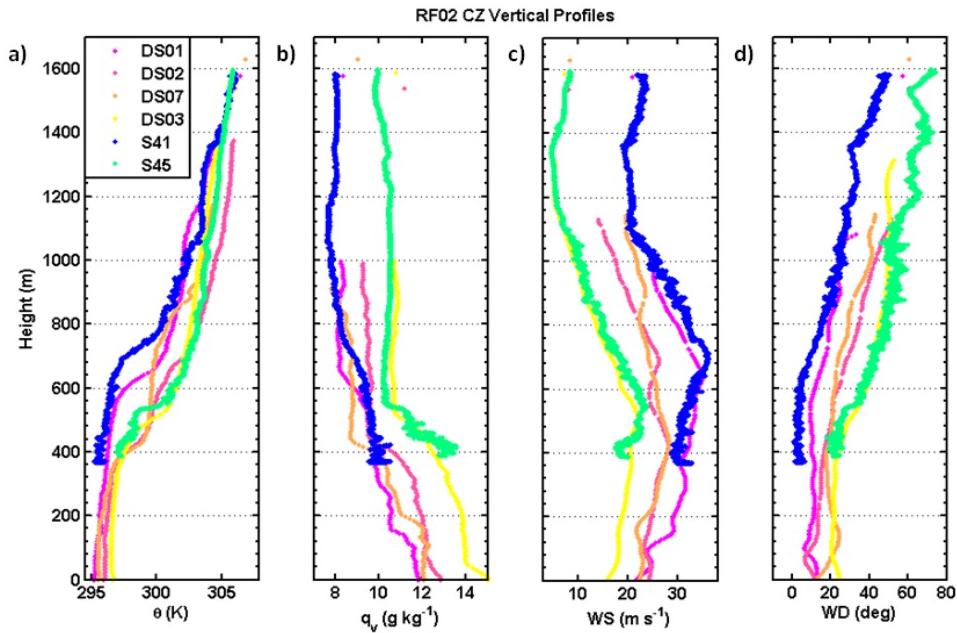
Figure 15.   Selected RF02 vertical profiles of a) potential temperature (K), b) specific humidity (g kg^{-1}), c) wind speed (m s^{-1}), and d) wind direction (deg) in the CZ region.

c.   *The Offshore Region*

The Offshore region of RF02 extended from approximately 12.7°N over the remaining flight track which ended at 10.1°N. Eleven soundings, three dropsondes, and two vertical stacks were measured within this region. Selected profiles are shown in Figure 16. The boundary layer within the Offshore region was well-mixed, warm and moist, with comparatively weaker northerly winds that were consistent throughout the

boundary layer (Figures 12 and 13 discussed earlier). Southward from 12.7°N, all vertical profiles showed the gradual increase of low-level temperature and water vapor, and an apparent decrease of wind speed. The jet core appeared to lower between DS06 and DS04, about 400–500 km away from the coastline. The stable stratification above the boundary layer was highly variable, similar to the Coupling Zone profiles. The vertical stacks showed little horizontal variability across the level legs (not shown). The spatial variability within this region was mostly in the N-S direction, away from shore.
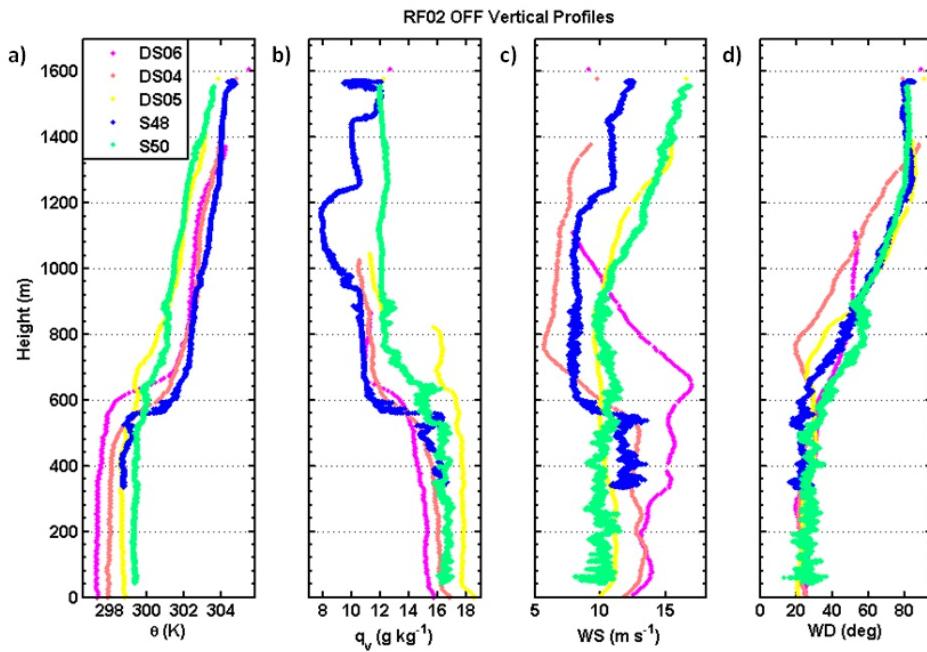
Figure 16.   Selected RF02 vertical profiles of a) potential temperature (K), b) specific humidity (g kg^{-1}), c) wind speed (m s^{-1}), and d) wind direction (deg) in the OFF region.

2.   Temporal Evolution of the Atmospheric Boundary Layer

Aircraft soundings and dropsondes measured approximately seven hours apart at the beginning and end of RF02 show the short-term temporal evolution of the MABL. RF03 measurements show the evolution of the MABL 24 hours after RF02 as the gap outflow continued to develop and then began to decay between RF02 and RF03 (Figure 21). In this section, we will use the aircraft measurements at the beginning and end of each flight to study the temporal evolution of the outflow jet. The flight track for RF03

45

covered the same Nearshore region as RF02 and was then oriented directly N-S along 94.75°W, east of the axis of the gap exit (Figure 9a). The track for RF03 was 30 km east of the RF02 track at 15°N and 73 km east of the track at 11°N. The location of the vertical stacks (VS, red), aircraft soundings (S, black), dropsondes (DS, blue), and AXBTs (BT, green) for RF03 are shown in Figure 17.
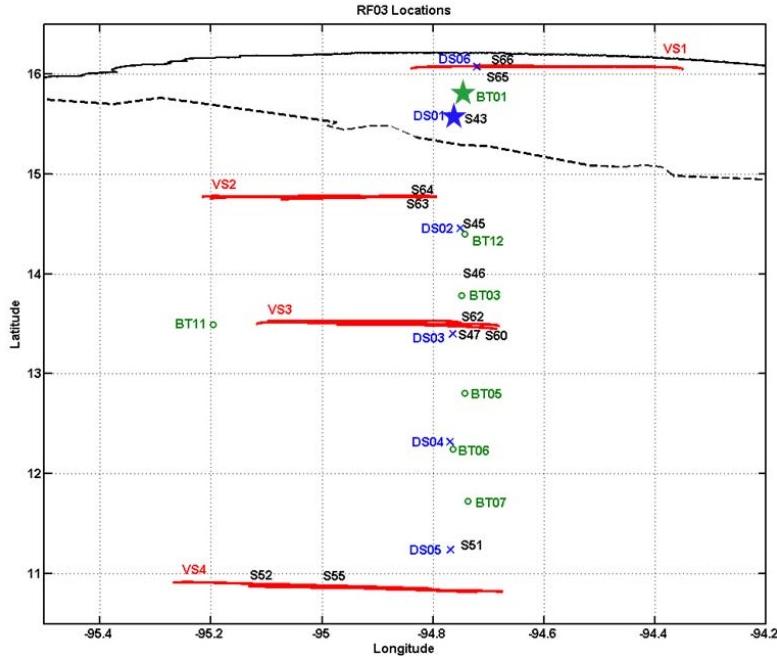
Figure 17.   Locations of aircraft measurements during RF03. Vertical stacks of level legs are shown in red and labeled VS. Aircraft soundings are shown in black and labeled S. The location of the label is the center point of the ascent/descent leg. Dropsonde locations are shown in blue and labeled DS. The blue star denotes the start of the dropsonde cross section shown in Figure 18b. The AXBTs are shown in green and labeled BT. The green star denotes the start of the AXBT cross section shown in Figure 32c.

Figure 18 shows a comparison of the vertical cross sections of wind speed from dropsonde measurements during RF02 and RF03 over a twenty-four hour period. These vertical cross sections were created by linearly interpolating between the available dropsonde profiles. The start point of the RF03 cross section (Figure 18b) was within the Nearshore region and was located 64 km to the NE of the start point of the RF02 cross section (Figure 18a); both start points are annotated in Figure 11 and Figure 17 for RF02

and RF03, respectively. The RF03 cross section showed a weaker jet core at 250 m elevation, with winds stronger than 20 m s^{-1} extending only 270 km offshore, compared to 350 km as seen in the RF02 cross section. Although the temporal variation was a contributing factor to the observed difference, the lesser extent of strong winds offshore was most likely due to the positioning of the RF03 cross section east of the outflow jet.
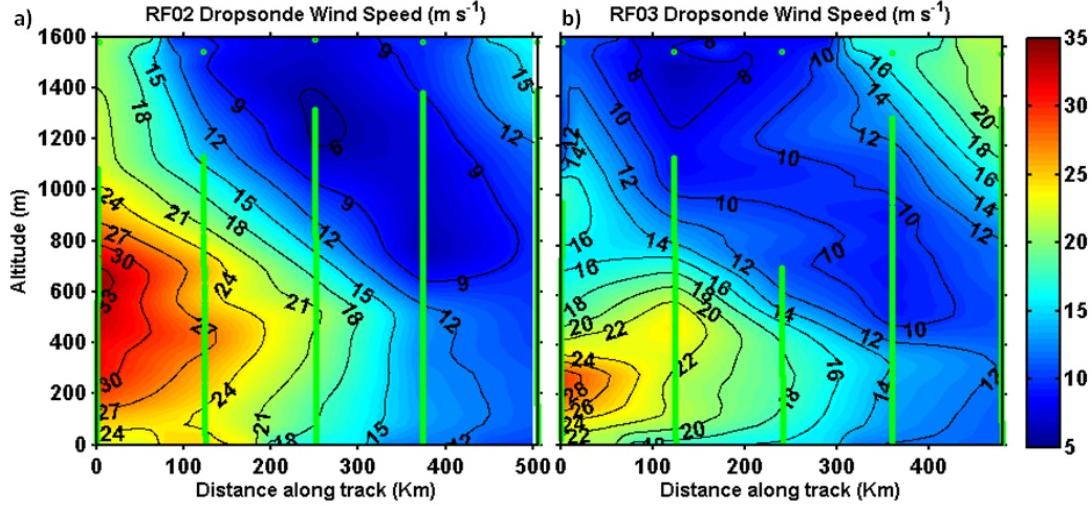
Figure 18.   Vertical cross sections of wind speed (m s^{-1}) interpolated from a) RF02 and b) RF03 dropsondes. Green vertical lines represent the locations where the dropsonde data were available. The horizontal axis shows the distance along the track in km. The start point for each cross section is shown by the blue star in Figures 11 and 17, respectively.

The mean measurements from the RF03 vertical stacks are shown in Figures 19 and 20. The Nearshore (VS1) wind stress and TKE have weakened significantly since RF02 (from 1.36 to 0.06 N m^{-2} and from 4.14 to 0.6 m^2 s^{-2}, respectively, Figure 19). RF02 VS1 had very strong low-level (30 m) wind stress and TKE which dropped off rapidly (Figure 12). During RF03, the wind stress and TKE at VS2 were weaker, but more consistent below 200 m. VS3, (red in Figure 19) showed that the wind speed, wind stress, and TKE continued to weaken with distance offshore within the boundary layer. The average wind speed within the boundary layer decreased from 19 m s^{-1} at VS2 to 13 m s^{-1} at VS3. Wind stress decreased by 50% between VS2 and VS3 (from approximately 0.5 N m^{-2} to 0.25 N m^{-2}), which were 130 km apart. Although the wind speed was weak,

approximately 11 m s^{-1} below 375 m, the wind stress at VS4 was slightly greater than within the Nearshore region (VS1).
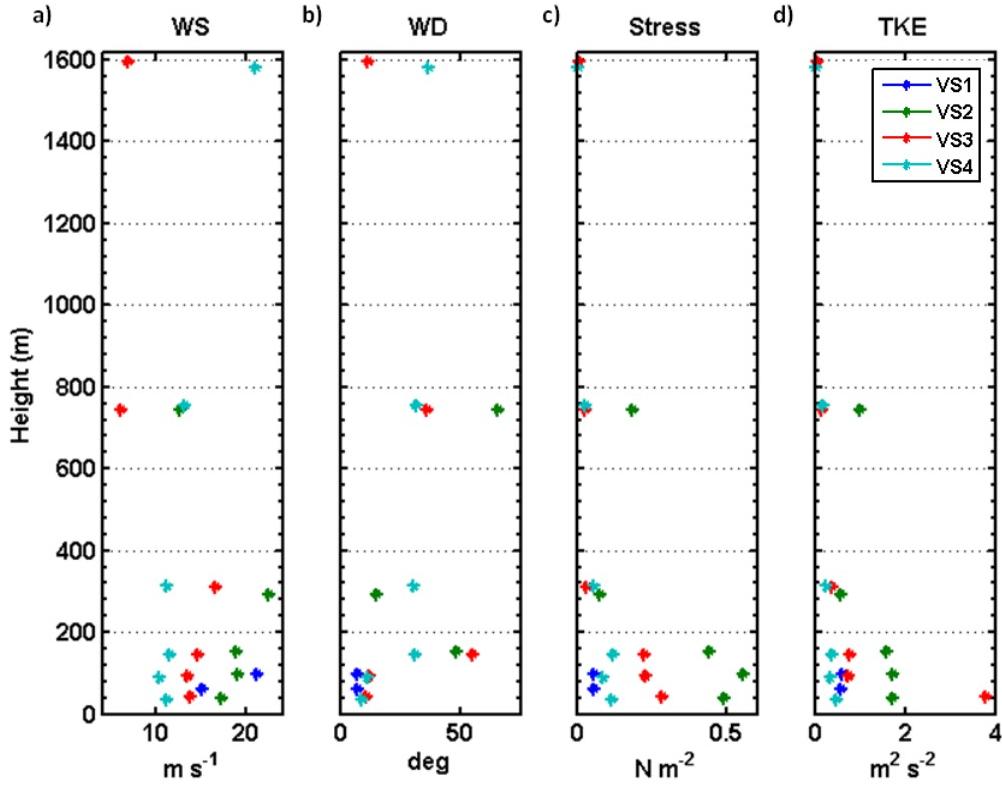
Figure 19.   Mean values of a) wind speed (m s^{-1}), b) wind direction (deg), c) wind stress (N m^{-2}), and d) TKE (m^2 s^{-2}) plotted at the mean altitude of the aircraft level leg for the four vertical stacks measured during RF03.

The Nearshore atmospheric boundary layer (VS1) remained unstable with a negative temperature gradient and negative sensible heat flux (Figure 20 a and b). Both VS2 and VS3 show that the boundary layer was well-mixed in temperature, with sensible heat flux near zero at 30 m, becoming increasingly negative above. The Offshore boundary layer along VS4 was well-mixed and warm (299 K) with weak positive sensible heat flux (approximately 15 W m^{-2}) near the surface, decreasing to near zero by 93 m above the surface.

Overall, the specific humidity from both flights was about the same with similar spatial gradients. The low-level latent heat flux in the Nearshore region along VS1 (46.3 W m^{-2}) was significantly weaker than during RF02 (286.1 W m^{-2}), due to continuously

cooling sea-surface temperatures reducing the air-sea temperature difference over the previous 24 hours (Figure 20 c and d). Within the Coupling Zone, the magnitude of the latent heat flux decreased and the low-level specific humidity increased from VS2 to VS3. The Coupling Zone during RF03 was warmer and more moist than the RF03 Nearshore region, but cooler and drier than the RF02 Coupling Zone. Analysis of the COAMPS simulations will help to determine if these observations were a true result of the temporal evolution, or simply the eastward displacement of the RF03 flight track.
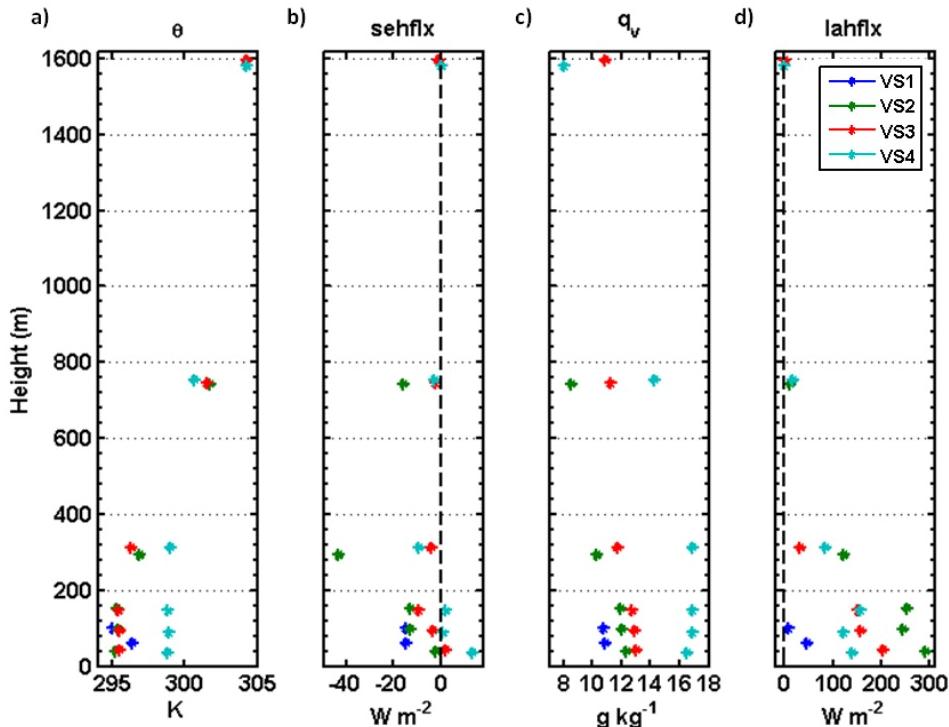
Figure 20.   Mean values of a) potential temperature (K), b) sensible heat flux (W m^{-2}), c) specific humidity (g kg^{-1}) and d) latent heat flux (W m^{-2}) plotted at the mean altitude of the aircraft level leg for the four vertical stacks measured during RF03.

a.   The Nearshore Region

At the mouth of the GoT, RF02 soundings S63, S64 and DS08 measured vertical profiles across the gap outflow seven hours after S40. S40 and S63 were co-located at the jet axis, while DS08 and S64 were located 40 km east of the jet axis (locations shown in Figure 11). All four profiles are plotted together in Figure 21 where the earlier sounding S40 is denoted 'RF02 early' (black line in Figure 21) and the later

three are denoted as 'RF02 late' (red in Figure 21). The later soundings revealed a cooling of approximately 1.5 K in the boundary layer (below 300 m) compared to the earlier sounding, S40, while low specific humidity remained constant. A stronger outflow jet was present at the end of RF02 with wind speed increasing with height to the top of the profile, reaching 35.8 m s^{-1} at 779 m. To the east, the elevation and magnitude of strongest winds decreased away from the jet axis. The later RF02 profiles show that Event II was still strengthening at 2200 UTC 7 February 2004 as wind speed increased, the elevation of the jet increased, and temperature decreased.
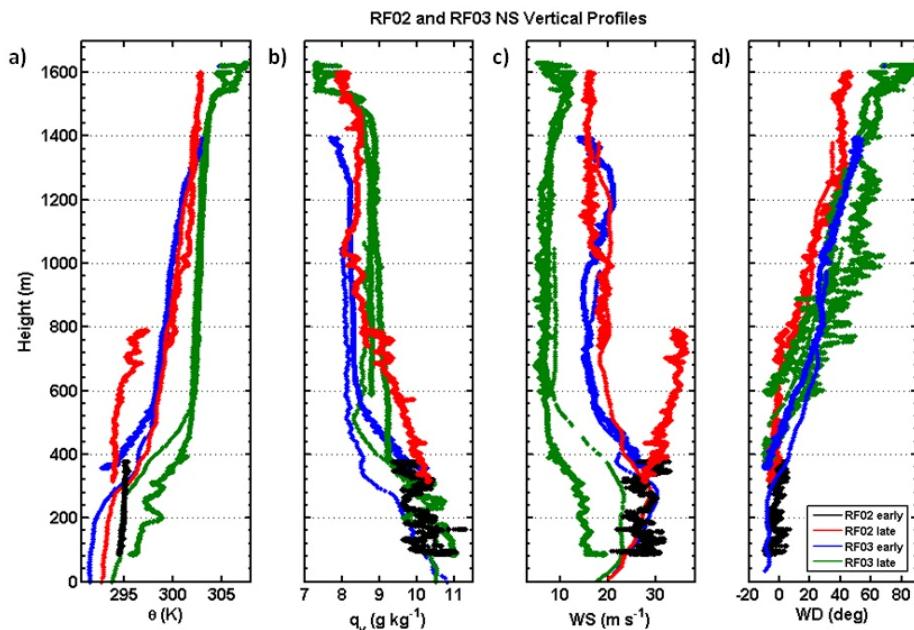
Figure 21.   Selected RF02 and RF03 vertical profiles of a) potential temperature (K), b) specific humidity (g kg^{-1}), c) wind speed (m s^{-1}), and d) wind direction (deg) in the NS region. Profiles colors correspond to measurement time: black was at the beginning of RF02; red was at the end of RF02, blue was at the beginning of RF03, green was at the end of RF03.

The Nearshore region, along the axis of the RF03 flight track at 94.75°W, extended 100 km from the shoreline. RF03 aircraft measurements within this region include two dropsondes, five soundings, and one vertical stack (VS1) with two 40 km level legs at 70 m and 100 m (Figure 17). RF03 VS1 was approximately 10 km north of RF02 VS1, approximately 10 km from shore. Vertical profiles along VS1 were measured

at the beginning and end of RF03, approximately 6.5 hours apart. The early vertical profiles are shown in blue in Figure 21, while the later profiles are shown in green. All of the RF03 vertical profiles within the Nearshore region are along the axis of the outflow jet. At the beginning of RF03, the jet maximum was 30.2 m s^{-1} at 267 m, with cool boundary layer air, consistent with the profile measured at the beginning of RF02 (black in Figure 21). However, the jet elevation and maximum speed was lower than at the end of RF02. During the flight, the Nearshore wind speed decreased (22.9 m s^{-1}) and the wind maximum deepened through the boundary layer from 85 m to 300 m as seen in the comparison from the blue to green wind speed profiles in Figure 21.

The boundary layer air, which cooled during RF02, continued to cool overnight. The coldest potential temperature measured within the boundary layer was at the beginning of RF03. At the end of RF03, the green profiles in Figure 21 revealed warming of the Nearshore region by 2.3 K within seven hours. Based on the COAMPS simulations, which will be discussed in detail in Chapter V, the typical range for the diurnal heating effect in the Nearshore region was approximately 2 K. While the warming agreed with typical daytime heating rates, it was in contrast with the continued cooling measured during RF02 while the gap outflow event was still intensifying.

Between RF02 and the beginning of RF03, the Nearshore boundary layer continued to cool. Colder air was advected over the GoT during the night. The source of this cold air was from both the Central American cold surge which initiated this event, and locally-advected cold air which was cooling during the night over land. During RF02, the gap outflow was intensifying and the advected air within the Nearshore region showed no diurnal warming. By RF03, the outflow was weakening and the Nearshore boundary layer air began to show evidence of late afternoon warming. The warming was most likely due to increased land surface temperatures warming the boundary layer air which was then advected over the GoT, rather than local heating of the boundary layer, because the mean sensible heat flux at VS1 was negative during this time (Figure 20).

51

b.   *The Coupling Zone*

The Coupling Zone region of RF03 contained two vertical stacks (VS2 and VS3) located approximately 130 km apart. The locations of the vertical stacks and corresponding vertical profiles are shown in Figure 17. The vertical profiles in Figure 22 are grouped by color to designate the sounding location and when they were measured with respect to flight time. The black and red profiles correspond to VS2, while the blue and green profiles correspond to VS3. The red and green profiles were measured approximately three hours after the black and blue profiles, respectively.

VS2, at 14.75°N, included four soundings, one dropsonde and five 45 km level legs from altitudes of 40 m to 750 m. All of the vertical profiles from VS2 (black and red, Figure 22) showed warmer, moister air and weaker wind speed within the boundary layer compared to the Nearshore region. This was consistent with RF02.

VS3 consisted of six 40 km level legs from 40 m to 1600 m along 13.5°N (Figure 17). Vertical profiles from this stack are shown in Figure 22 represented by the blue and green profiles. All of the profiles shown were measured along the axis of the flight track, which was east of the core of the outflow jet. The green profiles were measured approximately three hours after the blue profiles. During this time, the boundary layer warmed and moistened, while the wind speed weakened, further suggesting that Event II was weakening at the time of RF03.
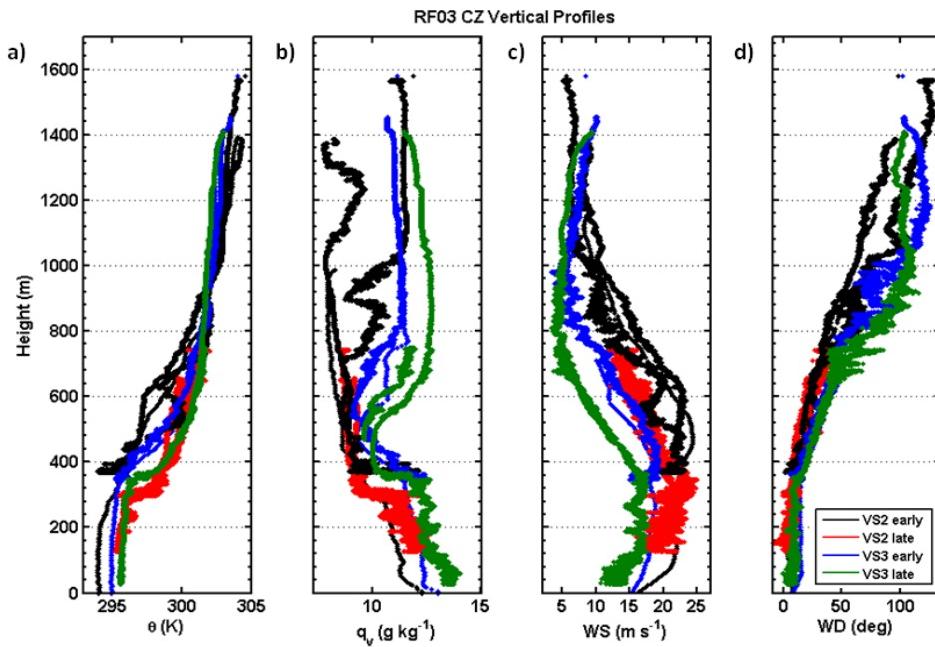
Figure 22. Selected RF03 vertical profiles of a) potential temperature (K), b) specific humidity (g kg^{-1}), c) wind speed (m s^{-1}), and d) wind direction (deg) in the CZ region.

c. The Offshore Region

The Offshore region for RF03 extended from 12.5°N south to 10.75°N. Within this region, there were two dropsondes, eleven soundings, and one vertical stack (VS4) of six 40 km level legs from altitudes of 40 m to 1580 m (locations shown in Figure 17). The dropsondes and vertical legs showed a warm, moist and well-mixed boundary layer with weak NE winds (Figure 23). Above the BL, there was stable stratification and increasing wind speed with winds which continued to veer east with height. The Offshore boundary layer was significantly warmer and moister than the Coupling Zone, and slightly warmer and moister than the Offshore region of RF02.
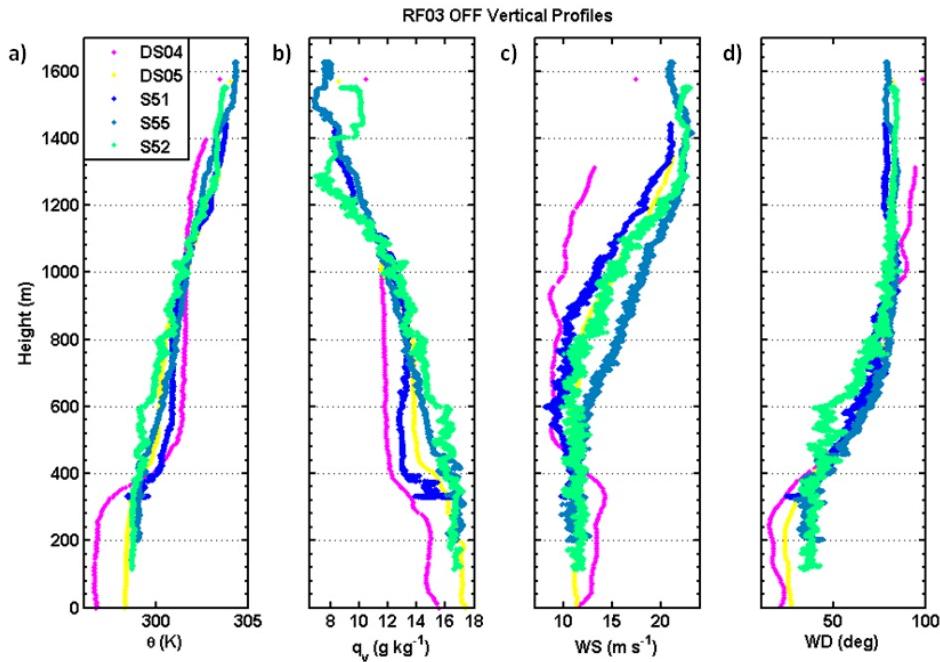
Figure 23.   Selected RF03 vertical profiles of a) potential temperature (K), b) specific
humidity (g kg^{-1}), c) wind speed (m s^{-1}), and d) wind direction (deg), in the OFF
region.

3.   Evolution of the Ocean Mixed Layer

Aircraft observations of the ocean mixed layer are limited to sea-surface temperature measurements from the onboard radiometer, and temperature profiles from AXBTs dropped along the flight path. Figure 24 shows the aircraft-measured sea-surface temperature from below 50 m altitude during RF02 and individual points show sea-surface temperature from the AXBTs. The coldest sea-surface temperatures were found nearshore and along the axis of the outflow jet. The aircraft-measured sea-surface temperatures showed cold sea-surface temperatures under the outflow jet from the coast southward to approximately 385 km offshore. South of 12.7°N, the sea-surface temperatures remained very warm (>299 K).
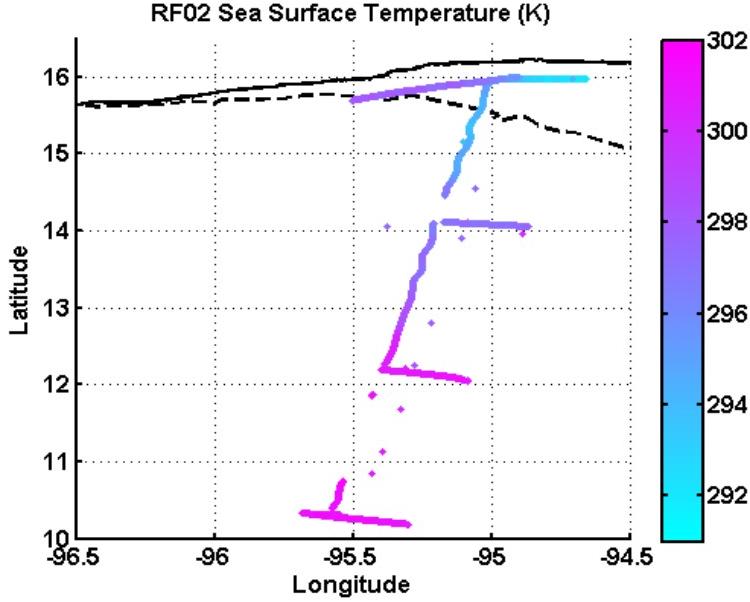
Figure 24.   Sea-surface temperature (K) from RF02 taken from aircraft measurements below 50 m altitude. Separate points indicate the location and SST of the AXBTs.

Flight RF02 recorded seventeen successful AXBTs. The AXBT-measured sea-surface temperature agreed well with the co-located aircraft-measured sea-surface temperature, with a mean difference of only 0.12 K (Figure 24). AXBT locations, color coded by region, and the corresponding temperature profiles are shown in Figure 25. The Nearshore profiles showed the coldest sea-surface temperature and a highly stratified upper-ocean without a mixed layer, as seen in BT01, measured at the beginning of the flight (Figure 25b). This absence of the mixed layer is indicative of coastal upwelling as the thermocline is pushed up to the surface and at the same time, disturbed by the strong surface forcing of turbulence (Gill 1982). Nearshore AXBTs measured at the end of RF02 (BT15, BT16, BT18) showed cool sea-surface temperatures, but unlike BT01, these profiles showed the presence of a mixed layer due to strong turbulent mixing forced by the outflow jet. These AXBTs were east of the jet axis where coastal upwelling was likely weaker.   Within the Nearshore region, the aircraft-measured sea-surface temperature from the lowest-level leg at 50 m was about 1.5 K cooler than measured by AXBT. Measurements from the level leg S32 also showed that the coldest sea-surface temperature was east of the jet axis, with minimum sea-surface temperature located

between 94.8°W to 94.7°W (Figure 24). Moving southward, the sea-surface temperatures increased, and both the thermocline and mixed layer deepened. BT12 and BT14 were located along 14°N to the east and west of the outflow, respectively. BT14 showed slight cooling of the sea-surface temperature and shallower thermocline, similar to other Coupling Zone profiles. BT12, located east of the outflow jet, more closely resembled the Offshore profiles with warm surface temperature, a relatively deep mixed layer, and deeper thermocline, suggesting that the ocean response was weaker to the east of the outflow.
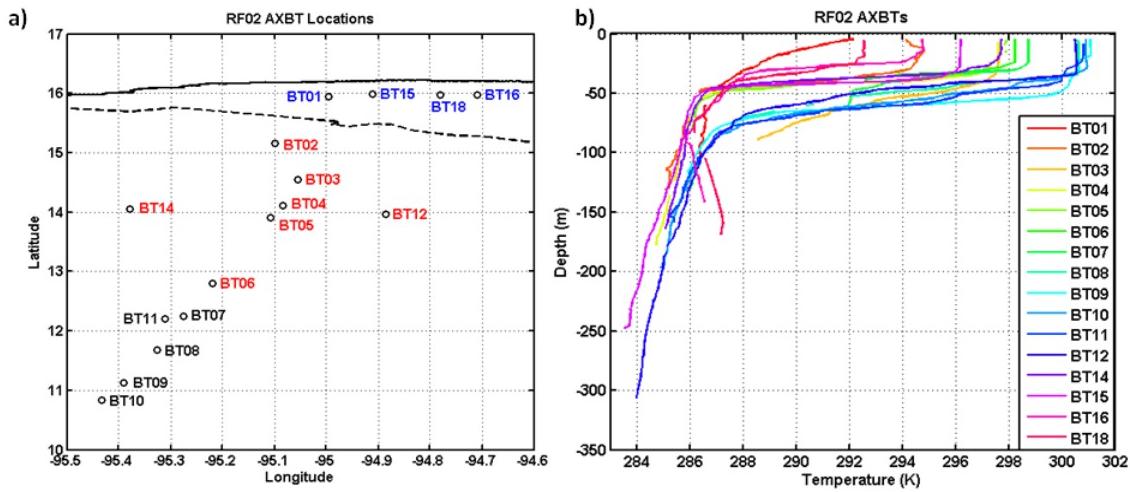
Figure 25.   a) Locations of RF02 AXBTs. NS AXBTs are in blue; CZ are in red; OFF are in black. b) Temperature (K) vs. depth (m) profiles for RF02 ABXTs.

Seven successful AXBTs were recorded during RF03 (Figure 26). These profiles show a clear distinction in the ocean structure between the three regions affected by the outflow. Nearshore, BT01 measured the coldest near-surface waters of RF03, which were an additional 2 K cooler than that measured nearby 24 hours earlier during RF02 (BT01 in Figure 25a). Similar to the temperatures of RF02 BT01, RF03 BT01 showed a raised thermocline with weakened thermal stratification in this region. The weaker thermocline close to the coast could be a result of the interaction between surface-driven entrainment mixing and internal waves that can initiate at the shelf break and become trapped in the coastal continental shelf zone (Gill 1982; Apel and Jackson 2002). Within the Coupling Zone, the temperature of the mixed layer was lower by 3–5 K compared to

Offshore temperatures and 2 K cooler than the RF02 Coupling Zone AXBT measurements. Upwelling within the Coupling Zone raised and strengthened the thermocline. The two Offshore profiles showed a warm, relatively deep OML, and deeper thermocline. The mixed layer depth within the Offshore region was slightly deeper during RF03, than RF02, possibly due to persistent wind forcing but also little to no upwelling in this region as well. The RF03 Offshore profiles are approximately 70 km east of the axis of the outflow jet. These profiles could represent "typical" ocean temperature profiles for the Gulf of Tehuantepec, however, without pre-event AXBTs; this cannot be confirmed from observations. Figure 28c shows the RF03 vertical cross section of temperature from selected RF03 AXBTs. This cross section shows the ocean thermal structure perpendicular from shore, just east of the gap exit. Colder surface temperatures were found from the Nearshore region to almost 300 km offshore, with the coldest temperatures closest to the coast. Upwelling was evident by the raised isotherms and was consistent with previous studies showing strong upwelling from divergent Ekman transport east of the outflow jet.
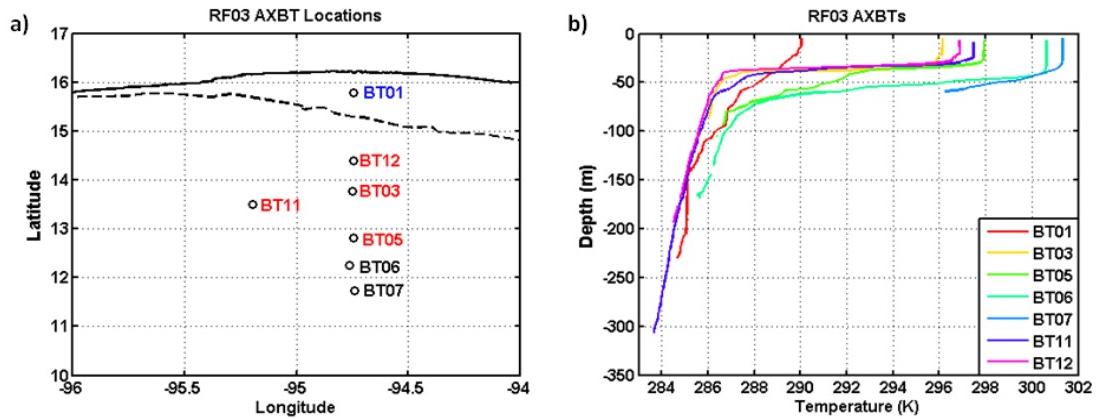
Figure 26. a) Locations of RF03 AXBTs. NS AXBTs are in blue; CZ are in red; OFF are in black. b) Temperature (K) vs. depth (m) profiles for RF03 ABXTs.

RF03 low-level aircraft measurements show the most dramatic sea-surface temperature changes within the Nearshore region. In a narrow strip at the gap exit, sea-surface temperatures cooled significantly overnight while slightly to the east and west of the outflow jet, the RF03 sea-surface temperatures were several degrees warmer. Figure

27 shows sea-surface temperature from level aircraft legs for RF02 and RF03 within the Nearshore region along 16°N, 20 km from the shore. A tongue of very cold surface water (287 K) was located between 94.9°W to 94.75°W, with strong sea-surface temperature gradients to either side. Multiple aircraft legs confirmed the presence of this cold tongue. The location of the sea-surface temperature minimum agrees with measurements from RF02, however, the surface temperatures cooled an additional 5–6 K within 24 hours. This cold tongue was possibly the result of entrainment of cold water due to the strong persistent wind forcing. Previous studies have described the existence of an ageostrophic southward jet near the surface as a result of the outflow forcing (Barton et al. 1993). Since no current measurements were made during GOTEX, the COAMPS/NCOM analysis in Chapter V will provide more insight into this feature.
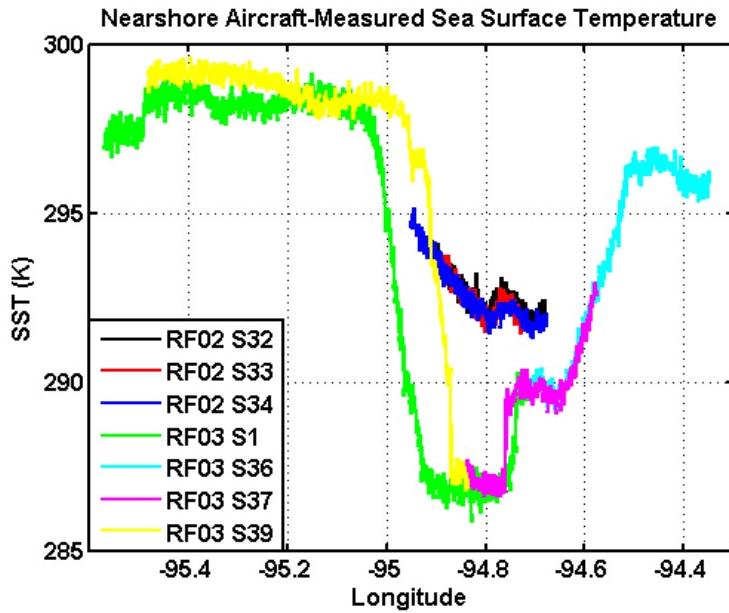
Figure 27.   Aircraft-measured sea-surface temperature (K) within the Nearshore region along 16°N during flights RF02 and RF03.

Some of the AXBTs were deployed nominally along a line in the north-south direction away from the coast. We are able to use these measurements to construct a vertical cross section of ocean temperature to show the change in the ocean thermal structure along each flight track. Figure 28 shows the tracks for the selected AXBTs for both RF02 and RF03, together with the vertical cross sections of temperature contours

along the track. Although the profiles used in the contour plots were included in Figure 25 and 26 individually, the contour plots in Figure 28 b and c are able to show the spatial coherence among neighboring AXBTs, especially below the mixed layer. The RF02 cross section shown in Figure 28b shows two regions of significantly cooler near-surface temperatures. The first cool region was near the coast, mainly due to BT01 (Figure 25b), and the second cold region was between 200 to 350 km offshore. As discussed earlier, the absence of an ocean mixed layer is indicative of coastal upwelling, as well as the interaction between coastal internal waves and entrainment. This contrasts well with the strong stratification of the seasonal thermocline seen in all of the other RF02 AXBTs further offshore. Although the presence of a shallow mixed layer was seen in each of the other individual profiles (Figure 25b), even a shallow mixed layer was not clearly seen in the contour plots, likely a result of the linear interpolation scheme used.

Although the two cross sections from RF02 and RF03 are not from the exact same track, there is still value in comparing the two temperature cross sections; particularly for the deep layers far below the shallow mixed layer. Assuming that the ocean between 50 m and 100 m depth are relatively homogeneous in the E-W direction between the flight tracks, we can compare the contour lines in this depth range between the two flights. For the Coupling Zone, this comparison can be made between the three profiles from RF02 and the two profiles from RF03 within the red dashed oval in Figure 28a. Here the mean contour line for the 288 K isotherm from RF02 was at a mean depth of about 90 m, while for RF03 it was about 60 m. Therefore, we can estimate an upwelling rate within the Coupling Zone of about 30 m day^{-1}. A rough estimate using the 286 K isotherm yields a comparable upwelling rate. The magnitude of upwelling in the Coupling Zone appears to be higher than that estimated by Roden (1961) and Clarke (1988) of 10 m day^{-1} due to forcing from the GoT outflow jet. For the Offshore region, the corresponding AXBTs for RF02 and RF03 (within the green dashed oval) appear to indicate downwelling consistently at multiple levels. In comparing the depth of several contour lines, the average downwelling is on the order of 20 m day^{-1}. These AXBT profiles certainly reveal the variable nature of the mesoscale ocean dynamics under the influence of the gap outflow, which will be seen more clearly from the coupled NCOM results, to be

discussed in Chapter V. The rough estimate of upwelling for Event II is much stronger than estimates from previous studies of this phenomenon (Roden 1961; Clarke 1988). However, it is also important to note that Event II was the strongest event of the five sampled by the C-130 during GOTEX.
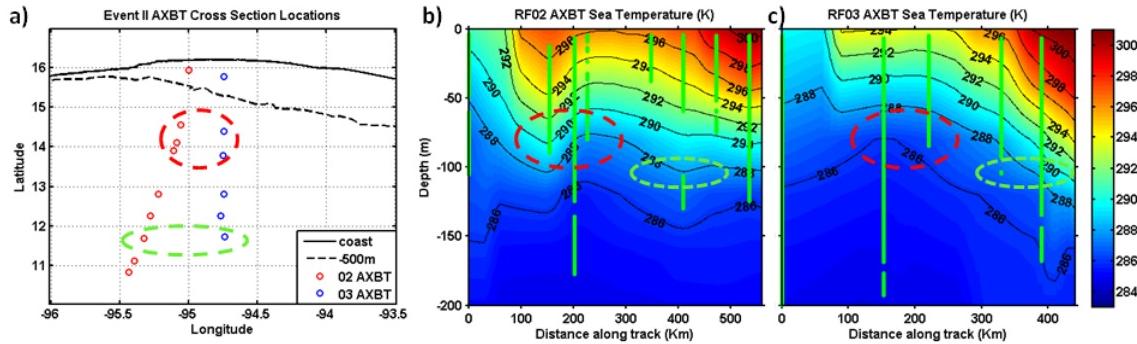
Figure 28.   a) Locations of RF02 (red) and RF03 (blue) AXBTs used for temperature cross sections. The start point of the RF03 cross section is 32 km southeast of the RF02 start point. b) Vertical cross section of sea temperature (K) from select along track RF02 AXBTs. c) Vertical cross section of sea temperature (K) from select along track RF03 AXBTs.

B.   EVENT V: 26–28 FEBRUARY 2004

Three flights measured the boundary layer conditions within the GoT before and during Event V. Figure 29 shows the COAMPS time series of surface wind stress from 00 UTC on 25 February 2004 to 00 UTC on 2 March 2004. RF08 measured the boundary layer conditions approximately 12 hours before the onset of Event V (shaded in green in Figure 29). After a rapid onset, Event V lasted until approximately 2100 UTC on 29 February 2004. Both RF09 and RF10, shaded in red and blue, respectively in Figure 29, measured the ABL and OML after the intensification stage of Event V.
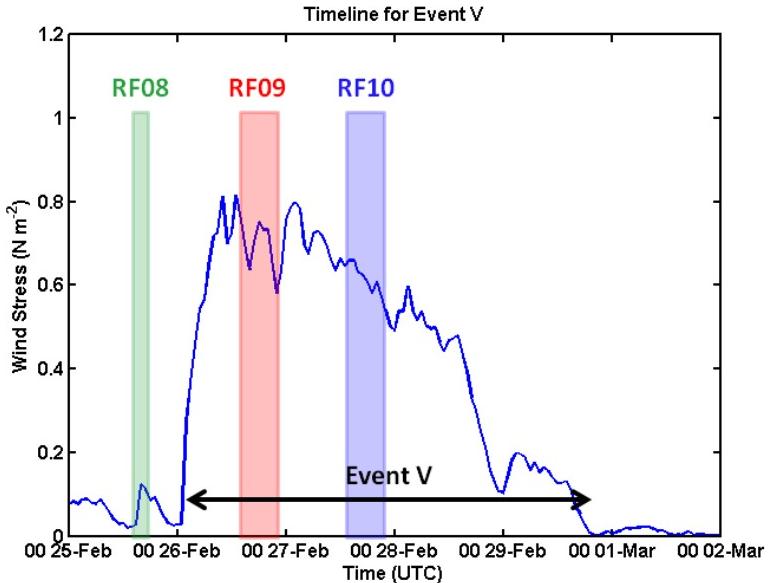
Figure 29. Time series of COAMPS wind stress (N m^{-2}) during Event V, 50 km offshore along 95°W. Event duration and flights times for RF08, RF09 and RF10 are identified by the green, red and blue shaded regions, respectively.

Prior to the onset of Event V, RF08 measured atmospheric conditions within the Nearshore region and along 95.1°W, the axis of the gap exit, southward to 14.3°N. Approximately five days after the end of Event IV and 12 hours prior to the onset of Event V, RF08, on 25 February 2004, provides the only pre-event measurements collected during GOTEX. This flight measured a low-level section parallel to the coast within the Nearshore region, and a second low-level section perpendicular to the coast just beyond the Nearshore boundary. A track of aircraft ascent/descent legs were made on the return leg of the flight. Vertical cross sections of wind speed, potential temperature, and specific humidity from RF08 aircraft soundings made on the return leg perpendicular to the coast are shown in Figure 30. These vertical cross sections show the ABL perpendicular to the coast along 95.1°W, beginning 64 km offshore. The start of the sounding cross section is marked with a blue star in Figure 31. Nearshore, surface winds were weak (less than 5 m s^{-1}) and southwesterly, likely the beginning of the daily sea breeze (Figure 30a, direction not shown). Along the entire RF08 flight track, potential temperature was warm and varied by less than 0.5 K (Figure 30b). Specific humidity was high within the sounding track (16–17 g kg^{-1}, Figure 30c), but relatively

61

lower close to the coast (14–15.5 g kg^{-1}) which was measured by the low-level legs nearshore (not shown). From the low-level measurements parallel to the coast within the Nearshore region, sensible heat flux ranged from 10–60 W m^{-2} and latent heat flux ranged from 25–200 W m^{-2} (not shown). Figure 31 shows the sea-surface temperature during RF08 from aircraft measurements below 50 m altitude. Close to the coast and south of 14.6°N, sea-surface temperatures were very warm (greater than 301 K, Figure 31). A cold pool of sea-surface temperatures, which appears to be persistent based on previous satellite sea-surface temperature studies (Xie et al. 2005), was measured from 15.3°N to 14.6°N, with sea-surface temperatures generally 2–3 K colder than surrounding waters. It is important to note that the coldest sea-surface temperature measured was still warm, 298.6K. The boundary layer was unstable throughout the RF08 flight track except over the cold pool. In an area of weak neutral stability over the cold pool, both sensible and latent heat fluxes were negative (-20 W m^{-2} and -100 W m^{-2}, respectively, not shown).
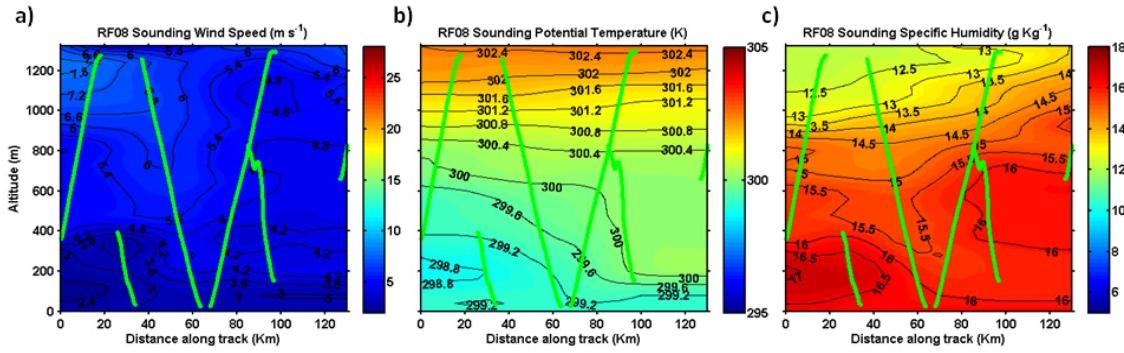
Figure 30.   Vertical cross sections of wind speed (m s^{-1}), potential temperature (K), and specific humidity (g kg^{-1}) along 95.1°W from aircraft soundings during RF08, 25 February 2004. Green vertical lines represent the location and vertical extent of the aircraft soundings. The horizontal axis shows the distance along the track in kilometers from the location of S12, 64 km from shore, and marked by a blue star in Figure 31.
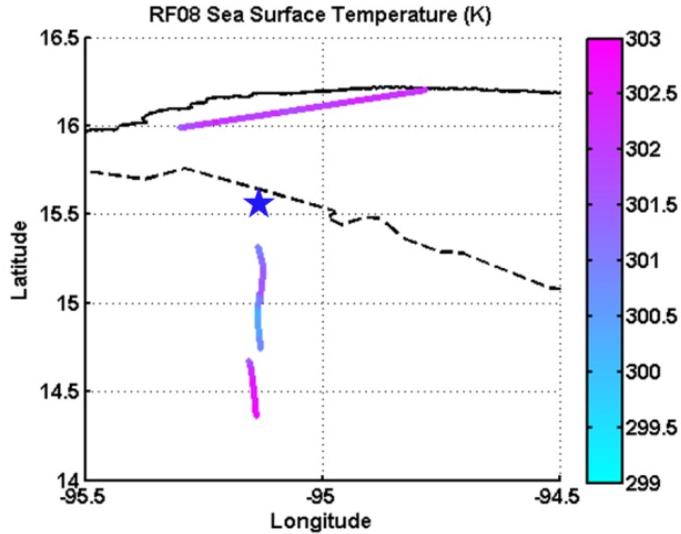
Figure 31.   Sea-surface temperature (K) from RF08 taken from aircraft measurements below 50 m altitude. The blue star denotes the start location of the aircraft sounding vertical cross sections in Figure 30.

Event V began at approximately 0300 UTC on 26 February 2004 and was measured by RF09 approximately eleven hours after onset and RF10 24 hours later (+35 hours), as shown in the event timeline in Figure 29. The general characteristics of Event V are illustrated using vertical cross sections of wind speed, temperature, and specific humidity from two successive flights, RF09 and RF10 (Figure 32 and 33, respectively). The RF09 vertical cross sections, shown in Figure 32, began 20 km from the coast within the Nearshore region. The start location is denoted by a blue star in Figure 34. During RF09, there was an elevated outflow jet, with the jet maximum located slightly offshore (Figure 32a). Roughly 250 km down the flight track, the jet core was at an elevation of approximately 600 m with the maximum velocity reduced to about 20 m s^{-1}. Unlike Event II, the boundary layer top, varying between 200 m and 600 m in depth, was not at the height of the jet core, except within the first 100 km. Above the boundary layer, the potential temperature showed cold, dry air throughout the entire sounding track (Figure 32 b and c). Within the boundary layer, potential temperature seemed to be well-mixed, while specific humidity showed significant vertical stratification. As specific humidity gradually increased downwind, the coldest air extended to 200 km down the track and began to increase afterwards. By the beginning of RF10, at 1430 UTC on 27 February,

63

the gap outflow was beginning to weaken. The RF10 vertical cross sections, which began 4 km from the coast as denoted by the blue star in Figure 41, showed that the outflow jet was weaker in magnitude and lower in elevation than 24 hours before, but the strongest winds reached farther offshore (Figure 33a). The coldest boundary layer air was farther south to 300 km along the dropsonde track (Figure 33b). Throughout the boundary layer, the air was drier during RF10 (Figure 33c), than during RF09. Although Event V began to weaken before the start of RF10, northerly winds flowed through the gap and over the GoT until 1 March 2004.
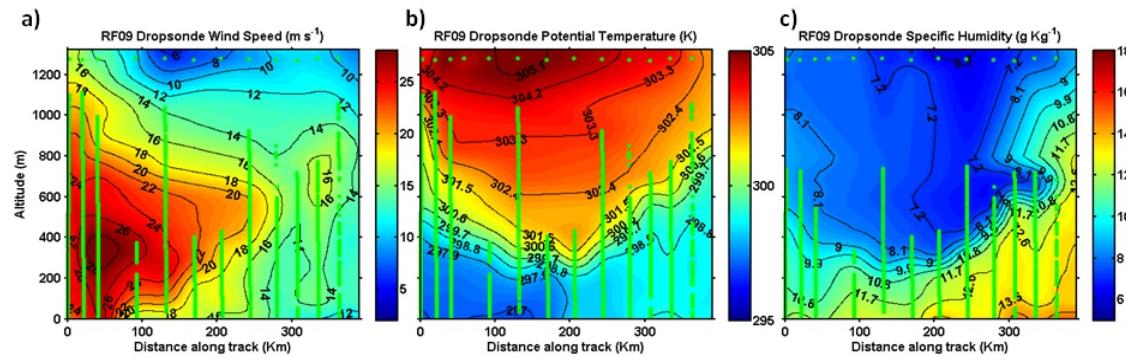
Figure 32.   Vertical cross sections of wind speed (m s⁻¹), potential temperature (K), and specific humidity (g kg⁻¹) from dropsondes during RF09, 26 February 2004. Green vertical lines represent the location and vertical extent of the dropsondes. The horizontal axis shows the distance along the track in kilometers from the location of DS14, 20 km from shore, and denoted with a blue star in Figure 34.
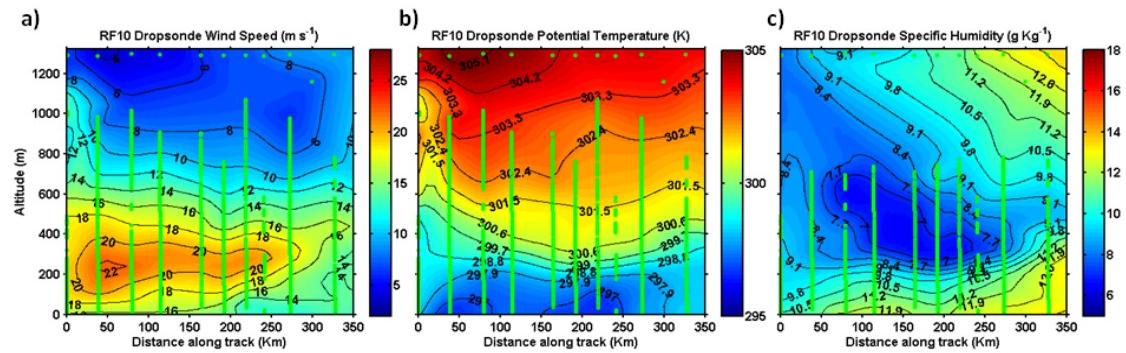
Figure 33.   Vertical cross sections of wind speed (m s⁻¹), potential temperature (K), and specific humidity (g kg⁻¹) from dropsondes during RF10, 27 February 2004. Green vertical lines represent the location and vertical extent of the dropsondes. The horizontal axis shows the distance along the track in kilometers from the location of DS12, 4 km from shore, and denoted with a blue star in Figure 41.

1. Downwind Evolution of the Atmospheric Boundary Layer

In contrast to RF02 and RF03, flights RF09 and RF10 measured a series of repeated low-level legs at each longitudinal cross section, rather than vertical stacks of level legs. Each location of these level legs will be referred to as cross sections (CS), which, along with the dropsondes (DS), AXBTs (BT), and selected aircraft soundings (S) are shown in Figure 34. The blue star marks the start location of the RF09 dropsonde vertical cross sections in Figure 32, and the green star marks the start of the AXBT vertical cross section in Figure 52b.

Figure 34. Locations of aircraft measurements during RF09. Cross sections of low-level legs are shown in red and labeled CS. Aircraft soundings are shown in black and labeled S. The location of the label is the center point of the ascent/descent leg. Dropsonde locations are shown in blue and labeled DS. The blue star denotes the start of the dropsonde cross sections shown in Figure 32. The AXBTs are shown in green and labeled BT. The green star denotes the start of the AXBT cross section shown in Figure 52b.

a.   The Nearshore Region

The Nearshore region of RF09 included two dropsondes, four soundings and two low-level cross sections (CS-A and CS-B) at 40 m altitude. For figure clarity, only selected vertical profiles are shown in this discussion. However, all available vertical profiles were used for the analysis. Along 16°N, CS-A included five level legs. Legs S1 through S4 were measured at the beginning of RF09. Leg S37, which was measured at the end of the flight, will be discussed later. Figure 35 shows the wind speed, potential temperature, sea-surface temperature, air-sea temperature difference, and specific humidity measured by these level legs. The wind speed was strongest east of 95.1°W, and boundary layer air was cooler with slightly higher specific humidity. There was a sea-surface temperature minimum at 95.1°W. West of the axis of the gap exit, potential temperature and sea-surface temperature increased while wind speed and specific humidity decreased. Co-located with CS-A, aircraft soundings S52 and S53 showed cold potential temperature, strong but variable wind, and high variability in specific humidity (Figure 36). These two soundings were measured successively, separated by less than 5 km and only a few minutes, but show a 2 g kg^{-1} difference in specific humidity, with the drier air to the west. This variability is consistent with the spatial variation seen along CS-A, except that the short sounding profiles also suggest weakly stable thermal stratification in a layer deeper than the jet core (DS14, Figure 36). From all soundings along CS-A, only 20 km from the gap exit, the low-level winds were strong throughout the boundary layer, with no apparent elevated jet maximum. DS13, shown in Figure 36, was located along the axis at 15.8°N, 21 km downwind of CS-A. The appearance of an elevated jet max in DS13 suggested that the elevated jet forms 20–40 km from the coast. It is also worth noting that the air-sea temperature difference from these legs consistently indicated an unstable boundary layer at the mouth of the gap.
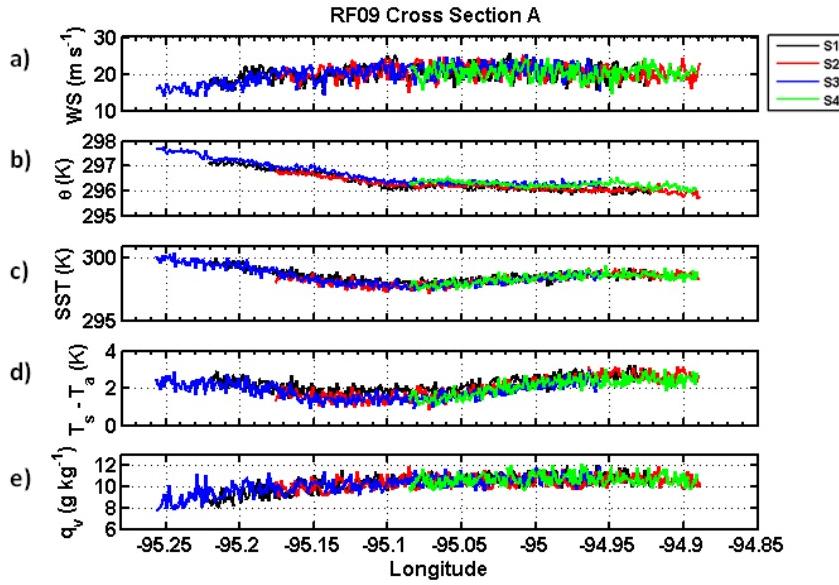
Figure 35.   a) Wind speed (m s^{-1}), b) potential temperature (K), c) SST (K), d) air-sea temperature difference (K), and e) specific humidity (g kg^{-1}) from aircraft level legs at 40 m altitude during RF09. CS-A is located along 16°N. S1-S4 are individual low-level legs within the CS-A group.
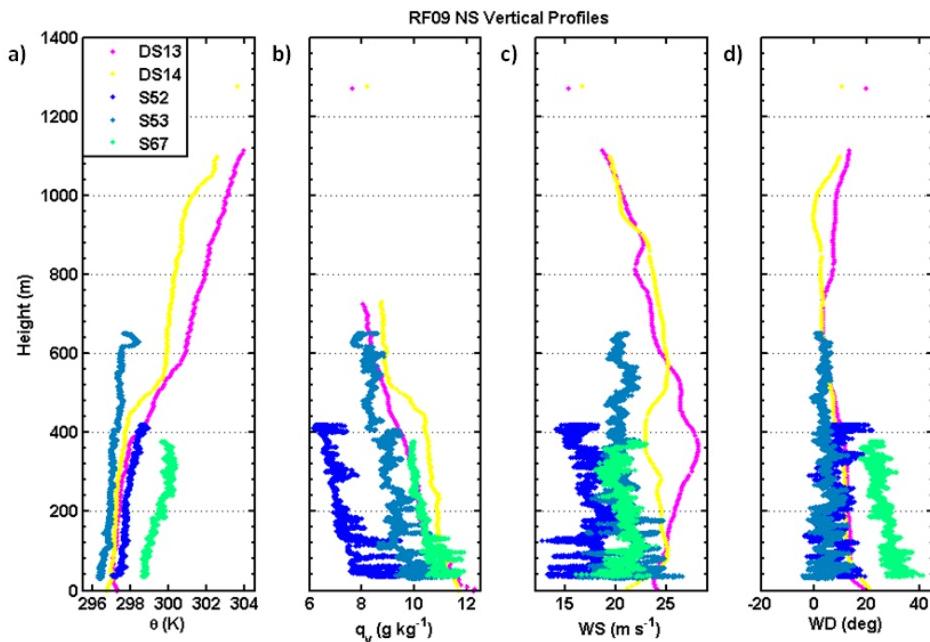
Figure 36.   RF09 vertical profiles of a) potential temperature (K), b) specific humidity (g kg^{-1}), c) wind speed (m s^{-1}), and d) wind direction (deg) in the NS region.

67

CS-B, which consisted of level legs S38 and S39, crossed the 500 m bathymetry contour, and thus the boundary for the Nearshore and Coupling Zone regions. The vertical black line in Figure 37 shows the longitude of the 500 m bathymetry contour along these legs, which coincides with the axis of the gap outflow, and essentially divides the cross section into the Nearshore region (to the right of the black line) and the Coupling Zone region (to the left). The wind speed was slightly stronger to the east, within the Nearshore region and near the jet core. There was no distinct change evident at the location of the NS/CZ boundary, although the mean TKE decreased from 3.31 m^2 s^{-2} within the Nearshore region to 1.98 m^2 s^{-2} within the Coupling Zone region (not shown). The coldest sea-surface temperature was west of the boundary, within the Coupling Zone region, at 95.3°W, where the atmospheric boundary layer became stable. This area of cold sea-surface temperature is also the location of the Middle America Trench which provides a permanent, deep reservoir of cold water beneath the ocean mixed layer.
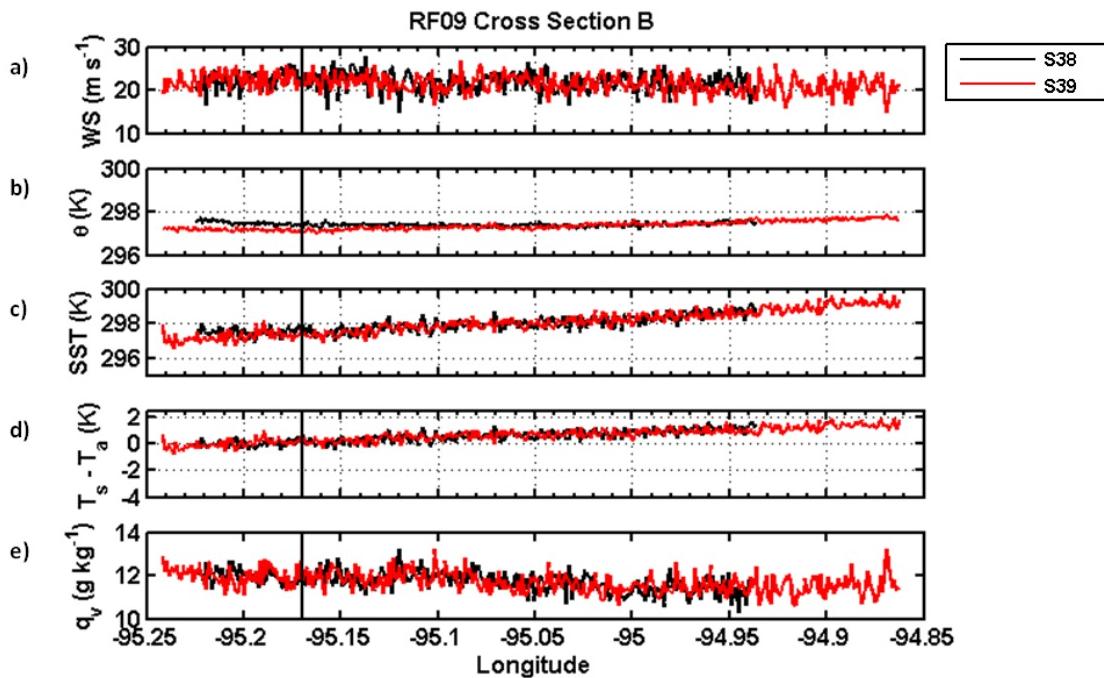
Figure 37.   a) Wind speed (m s^{-1}), b) potential temperature (K), c) SST (K), d) air-sea temperature difference (K), and e) specific humidity (g kg^{-1}) from aircraft level legs at 40m altitude during RF09. CS-B is located along 15.68°N and crosses the 500 m bathymetry contour at 95.17°W, marked by the vertical black line.

b. *The Coupling Zone Region*

The Coupling Zone region for RF09 contained five dropsondes, five soundings, and two low-level cross sections (CS-C and CS-D). The vertical profiles are shown in Figure 38. DS12, the northernmost vertical profile within the Coupling Zone region, measured a jet maximum of 29.6 m s^{-1} at 343 m altitude, with wind speed weakening to the south. To the west of the jet axis, S68 and S54 showed warmer boundary layer air. S54, approximately 40 km west of the axis, measured the lowest near-surface specific humidity and the weakest wind a stronger easterly wind component than others. CS-C, which consisted of legs S6 and S7, showed the western extent of the outflow jet (Figure 39). Spanning from the jet axis approximately 80 km to the west, CS-C showed that wind speed decreased toward the west continuously from the axis to 95.85°W, with a stronger and persistent decrease west of 95.53°W, accompanied by increases in both sea-surface and air temperature. The sea-surface temperature minimum was located at 95.4°W. The boundary layer was stable over the area of minimum sea-surface temperature along the western edge of the outflow jet. Based on Figure 39, the western extent of the outflow jet at this latitude was between 95.5°W to 95.4°W, with a gradual decrease in atmospheric outflow effects west of this boundary. The high frequency perturbations east of this boundary, most apparent in wind speed, suggest a strong turbulence field near the outflow axis, which also had stable thermal stratification. The stronger turbulence must have been generated by the near-surface vertical wind shear.
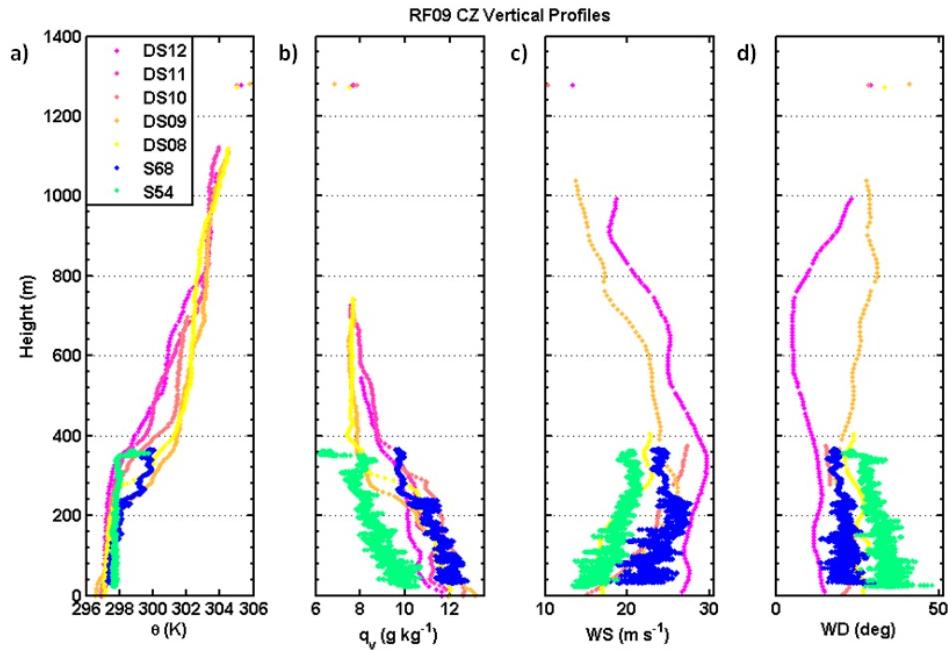
Figure 38.   RF09 vertical profiles of a) potential temperature (K), b) specific humidity (g kg^{-1}), c) wind speed (m s^{-1}), and d) wind direction (deg) in the CZ region.
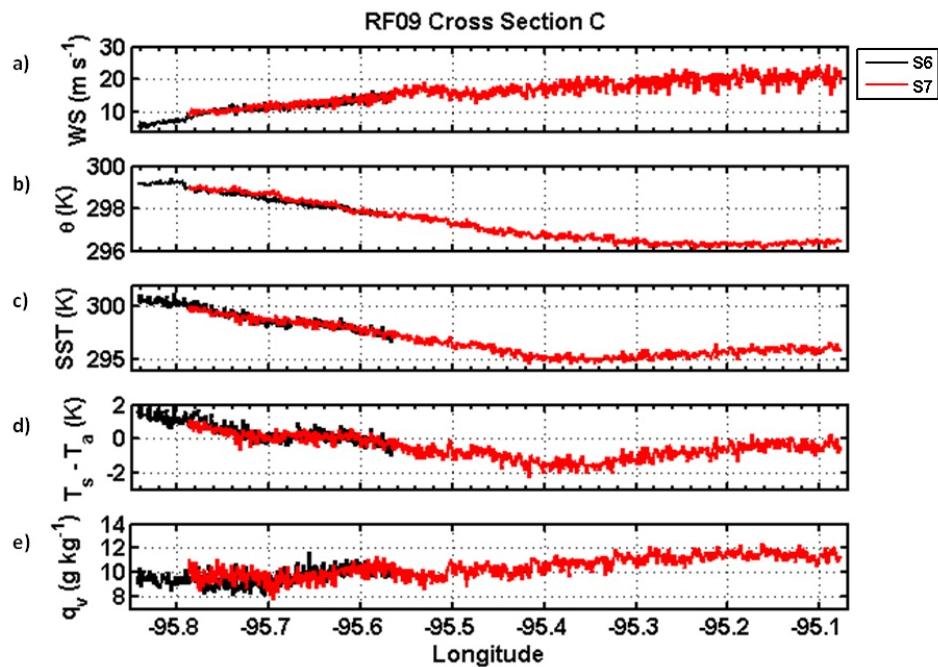
Figure 39.   a) Wind speed (m s^{-1}), b) potential temperature (K), c) SST (K), d) air-sea temperature difference (K), and e) specific humidity (g kg^{-1}) from aircraft level legs at 40m altitude during RF09. CS-C spans diagonally from 15.6°N at the west end to 15.2°N at the east end.

The second Coupling Zone cross section, CS-D, was measured as the flight track turned toward the southwest to follow the anticyclonic turning of the outflow jet. The consistent wind speed, potential temperature and specific humidity along this cross section indicated that the entire section was within the outflow jet as it turned (not shown). The RF09 Coupling Zone region had slightly weaker winds, warmer potential temperature, and higher specific humidity than the Nearshore region. The coldest sea-surface temperatures were found along CS-A and the CZ (western) side of CS-B, located over the deep trench.

c. The Offshore Region

The Offshore region of RF09 includes seven dropsondes, eight soundings, and four low-level cross sections, and spanned from approximately 200 km to 400 km offshore. The aircraft soundings all had a maximum altitude of less than 400 m, but were still able to provide information about the ABL conditions. These soundings measured a warm, moist and well-mixed boundary layer, with consistent wind speed which weakened with distance from shore (Figure 40). The dropsondes were released on the return leg of the flight so that DS01 was the southernmost vertical profile, while DS07 was the northernmost profile within the Offshore region. These dropsondes agree well with the aircraft soundings within the boundary layer and show that the height of the top of the boundary layer varied significantly in this region from 225 m at 14.25°N (DS07) to 800 m at 12.8°N (DS01). The warmest potential temperature, highest specific humidity and weakest winds were found the furthest offshore. The four low-level cross sections (CS-E through CS-H in Figure 34) show almost no horizontal variability. Throughout the entire Offshore region, the boundary layer was unstable due to very warm sea-surface temperature (greater than 300K). Potential temperature and specific humidity increased to the south, as expected with warm sea-surface temperature and unstable boundary layer conditions. Both the vertical profiles and the low-level cross sections showed that wind speed continued to weaken with increased distance from shore.
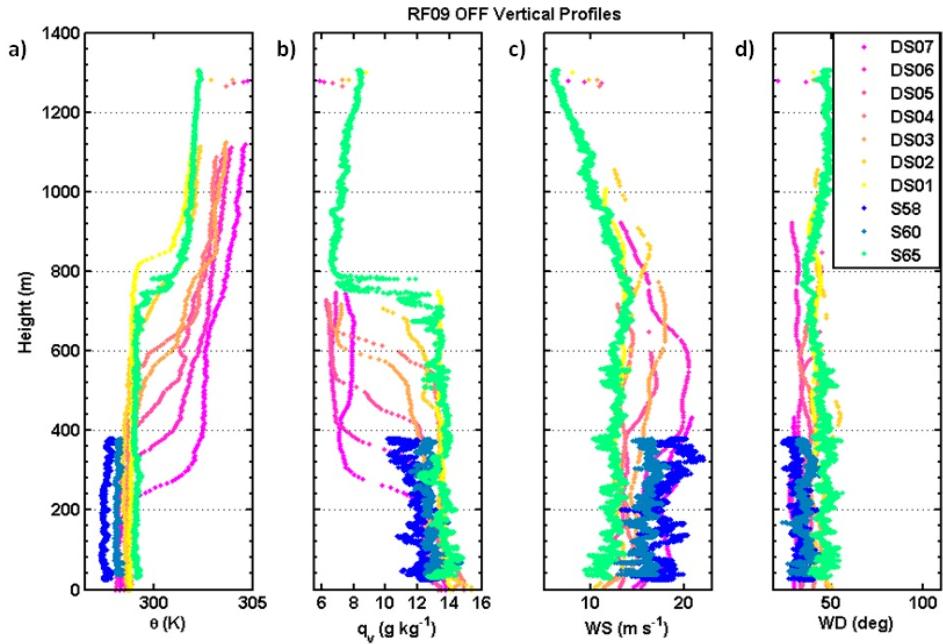
Figure 40.   RF09 vertical profiles of a) potential temperature (K), b) specific humidity (g kg^{-1}), c) wind speed (m s^{-1}), d) wind direction (deg) in the OFF region.

2.   Temporal Evolution of the Atmospheric Boundary Layer

Within the Nearshore and Coupling Zone regions, measurements taken at the beginning and end of flight RF09 showed the temporal evolution of the MABL on the time scale of a few hours. Flight RF10 measurements showed the temporal evolution 24 hours later, after Event V began to weaken. Figure 41 shows the locations of the low-level cross sections, dropsondes, AXBTs, and selected aircraft soundings for RF10. The start locations of the dropsonde (Figure 33) and AXBT (Figure 52c) vertical cross sections are marked by the blue and green stars, respectively.
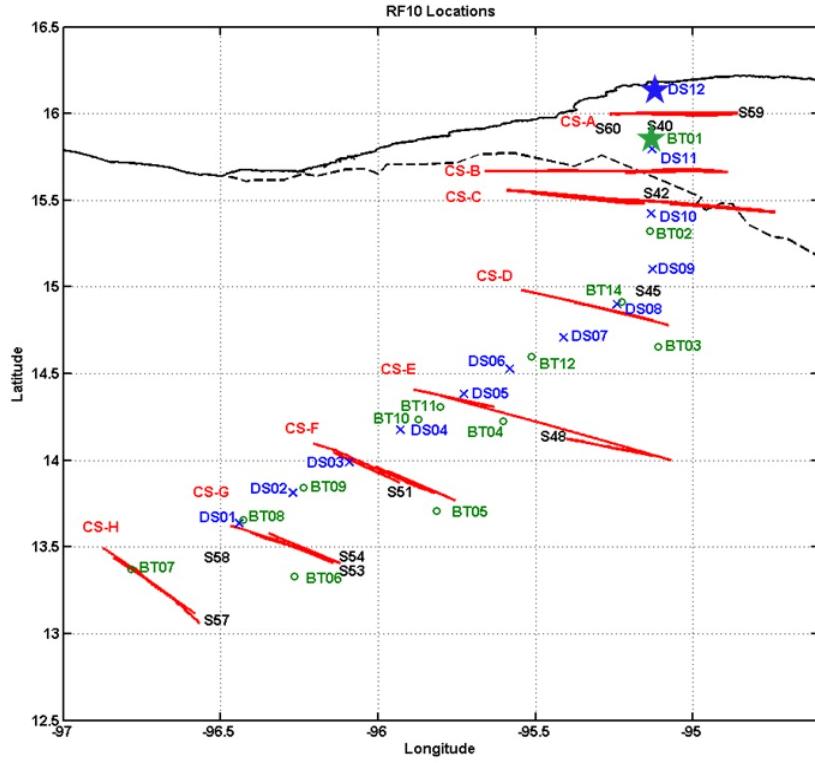
Figure 41.   Locations of aircraft measurements during RF10. Cross sections of low-level legs are shown in red and labeled CS. Aircraft soundings are shown in black and labeled S. The location of the label is the center point of the ascent/descent leg. Dropsonde locations are shown in blue and labeled DS. The blue star denotes the start of the dropsonde cross sections shown in Figure 33. The AXBTs are shown in green and labeled BT. The green star denotes the start of the AXBT cross section shown in Figure 52c.

a.   The Nearshore Region

The Nearshore region was measured at the beginning and end of flights RF09 and RF10. Low-level legs S1 and S37 of CS-A (RF09) measured across the outflow axis at 40 m altitude along 16°N. RF10 CS-A was co-located with that of RF09. Legs S1 and S36 measured the same location six hours apart on 27 February 2004. Figure 42 shows the wind speed, potential temperature, sea-surface temperature, air-sea temperature difference, and specific humidity for these four legs. Wind stress, TKE, sensible heat flux, and latent heat flux for these legs are shown in Figure 43. During RF09, potential temperature increased due to a combination of strong positive sensible heat flux and diurnal heating effects which warmed the boundary layer air overland

before it was advected over the GoT. Specific humidity increased due to strong positive latent heat flux. Throughout the flight, the air temperature warmed and sea-surface temperatures cooled which reduced the air-sea temperature difference and the atmospheric boundary layer became weakly unstable to near-neutral. As a result of changing stability during RF09, both sensible and latent heat fluxes were reduced. Although there was no significant change in wind speed, wind stress and TKE decreased.

Twenty-four hours later at 1427 UTC on 27 February 2004, RF10 began to measure the gap outflow along the same track as RF09. Due to continuous turbulent mixing inducing entrainment mixing at the bottom of the ocean mixed layer, the sea-surface temperatures at the beginning of RF10 were colder by approximately 4.5 K than at the end of RF09 (S37), giving a cooling rate of 4.5 K day^{-1}. The cooler sea-surface temperature resulted in a stable to near-neutral boundary layer (Figure 42). During RF10, the boundary layer became increasingly stable as the air temperature rose. Due to the stable boundary layer, sensible heat flux was negative (Figure 43). The increased potential temperature was likely due to warm air advection from diurnal heating over land, which had a stronger effect than the sensible heat-flux divergence, so that the boundary layer continued to stabilize.

Latent heat flux was significantly weaker during RF10 than RF09 due to colder sea-surface temperatures as well as the stable boundary layer. Warming of the sea-surface temperatures to the west during RF10 resulted in a slight increase in latent heat flux, while across the rest of the cross sections, the sea-surface temperatures remained cold and the latent heat flux continued to decrease. In fact, by the time of leg S36 during RF10, the sea-surface temperature, especially to the west, had already started to rebound.
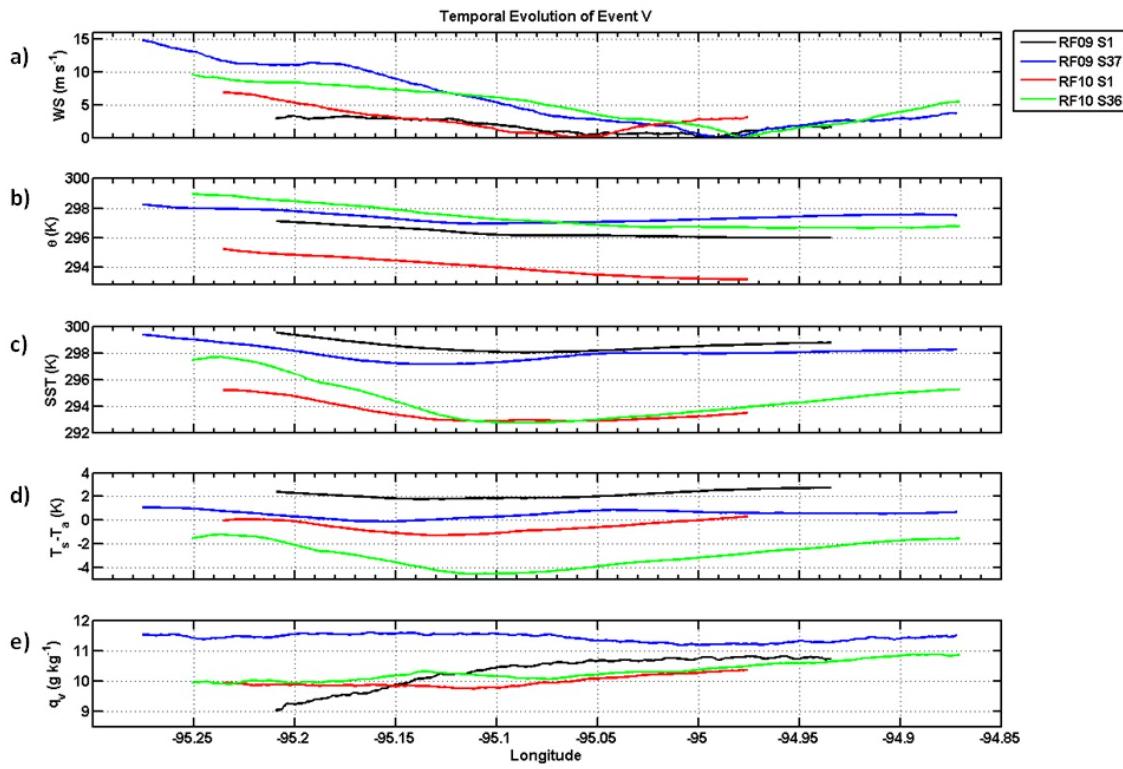
Figure 42. Aircraft measurements of a) wind speed (m s^{-1}), b) potential temperature (K), c) SST (K), d) air-sea temperature difference (T_s-T_a, K), and e) specific humidity (g kg^{-1}) from level legs at 40m altitude during RF09 and RF10 located along 16°N.
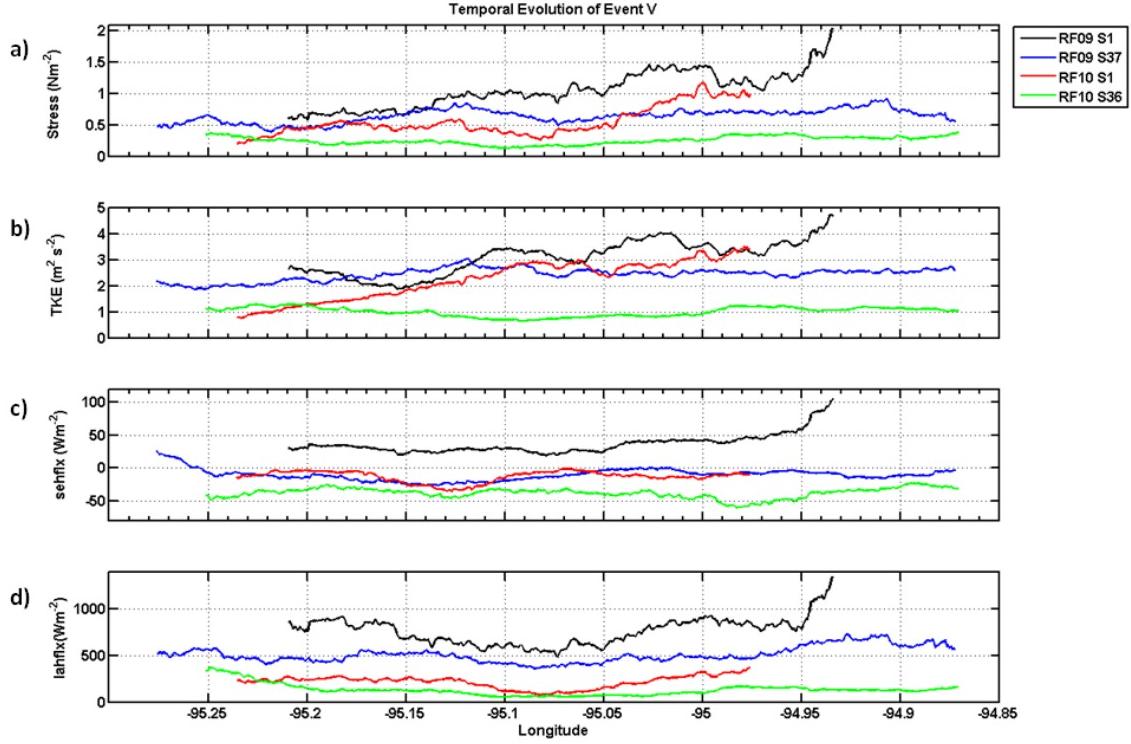
Figure 43.   Aircraft measurements of for a) wind stress (N m^{-2}), b) turbulent kinetic energy (TKE, m^2 s^{-2}), c) sensible heat flux (W m^{-2}) and d) latent heat flux (W m^{-2}) from level legs at 40m altitude during RF09 and RF10 located along 16°N.

Within the RF10 Nearshore region, there were two dropsondes, three soundings and one low-level cross section (CS-A). Sounding S40, located at the axis of the gap exit, was the only vertical profile in the Nearshore region measured at the beginning of RF10. Compared to nearby RF09 vertical profiles, the boundary layer was 2 K colder, 2 g kg^{-1} drier, and wind speed had weakened (Figure 44). Six hours later, DS12 (pink) and DS11 (yellow) measured the boundary layer conditions at the axis 4 km and 44 km from the coast, respectively (Figure 44). Closest to the coast (DS12), the boundary layer air was 1.5–2 K warmer and slightly drier (less than 0.5 g kg^{-1}) than at DS11. With there was strong wind shear from the surface to approximately 150 m, the wind speed was more consistent than in previous flights. East of the axis (S59, green), the wind speed was slightly weaker. The potential temperature was consistent with the dropsondes near the axis, but the specific humidity was higher. Similar to S59, S60 (dark blue) showed weaker winds to the west away from the outflow axis. The warmest, driest

76

boundary layer air was measured west of the outflow. It is also noted that the wind direction here showed northerly wind at the jet core (S40, light blue), while the soundings to the east (S59, green) and west (S60, dark blue) showed westerly and easterly components, respectively. Thus, fanning of the surface wind began within 25 km of the coast.
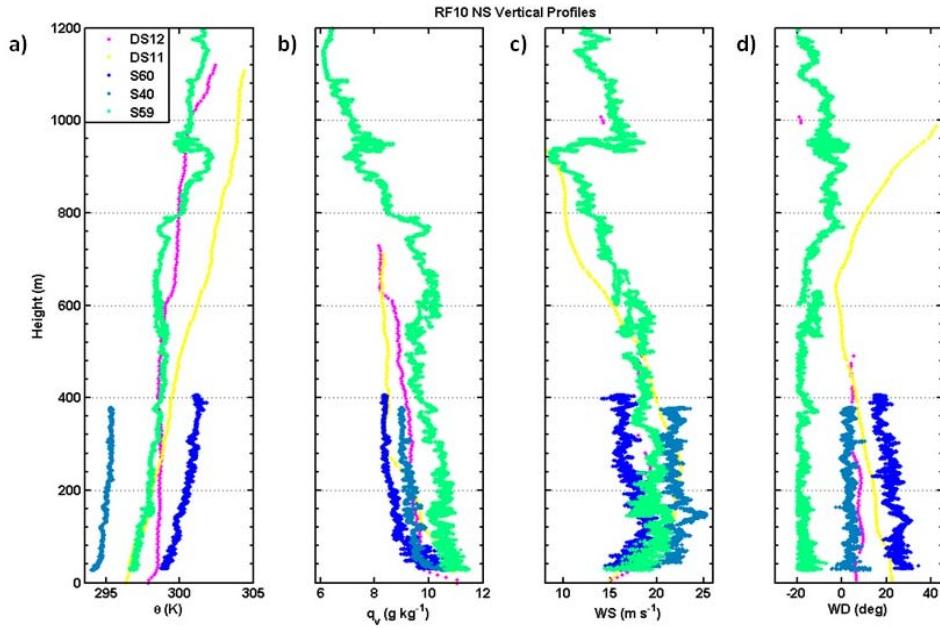
Figure 44.   RF10 vertical profiles of a) potential temperature (K), b) specific humidity (g kg^{-1}), c) wind speed (m s^{-1}), d) wind direction (deg) in the NS region.

Within the Nearshore region, east of 95.2°W, potential temperature, sea-surface temperature and specific humidity varied little from RF09, legs S38 and S39 (shown in Figure 37). Similar to RF09, TKE was stronger over the shelf, shoreward of the 500 m bathymetry contour. The mean TKE on the NS (eastern) side of the cross section was 1.96 m^2 s^{-2}, while on the CZ (western) side, TKE decreased to 0.94 m^2 s^{-2} (not shown). To the west, within the Coupling Zone region, sea-surface temperature showed the most notable difference. Instead of a minimum sea-surface temperature at 95.4°W, sea-surface temperatures to the west were approximately 3 K cooler than during RF09. Lower specific humidity in this region was a result of negligible latent heat flux due to the cold sea-surface temperatures. Again, there was no distinct change at the

location of the NS/CZ boundary. However, there did appear to be a boundary in wind speed, potential temperature and specific humidity at 95.4°W, which could indicate where the western extent of the outflow was during this flight.
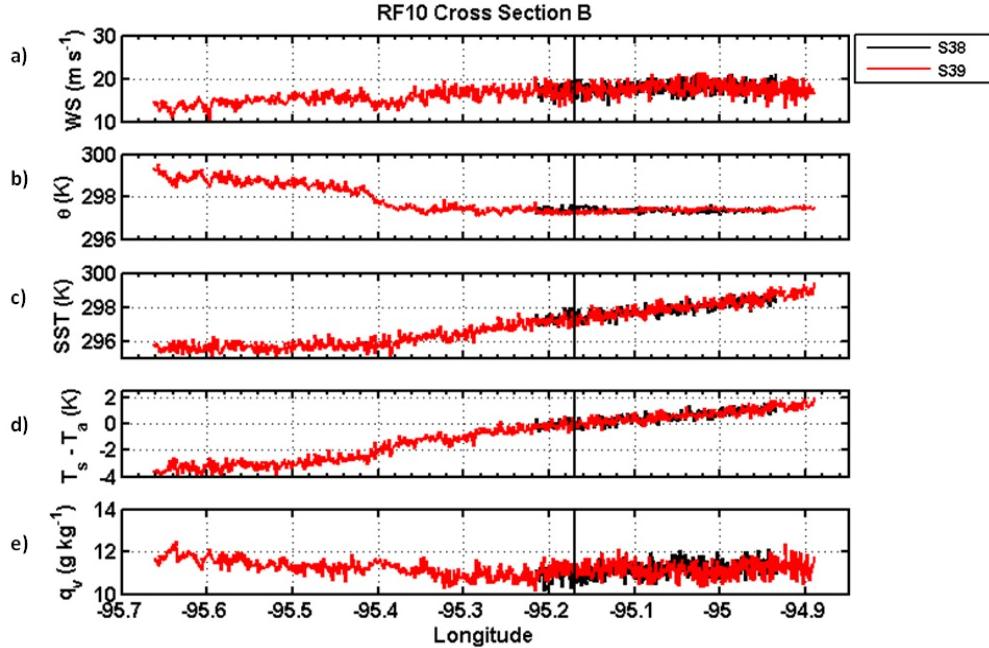

Figure 45.   a) Wind speed (m s^{-1}), b) potential temperature (K), c) SST (K), d) air-sea temperature difference (K), and e) specific humidity (g kg^{-1}) from aircraft level legs at 40m altitude during RF10. CS-B is located along 15.68°N and crosses the 500 m bathymetry contour at 95.17°W, marked by the vertical black line.

b.   The Coupling Zone Region

The Coupling Zone region of RF10 covered over 150 km in along track distance. This region included seven dropsondes, nine soundings and three low-level cross sections (CS-C, CS-D and CS-E). Selected vertical profiles are shown in Figure 46. The dropsondes (green) measured the boundary layer five hours after the aircraft soundings (blue). During these five hours, the boundary layer within the Coupling Zone warmed by approximately 2 K, while the maximum wind speed weakened by approximately 5–8 m s^{-1}. The remained low-level cross sections (not shown) measured consistent warming and moistening of the boundary layer, with little variability across the low-level legs.
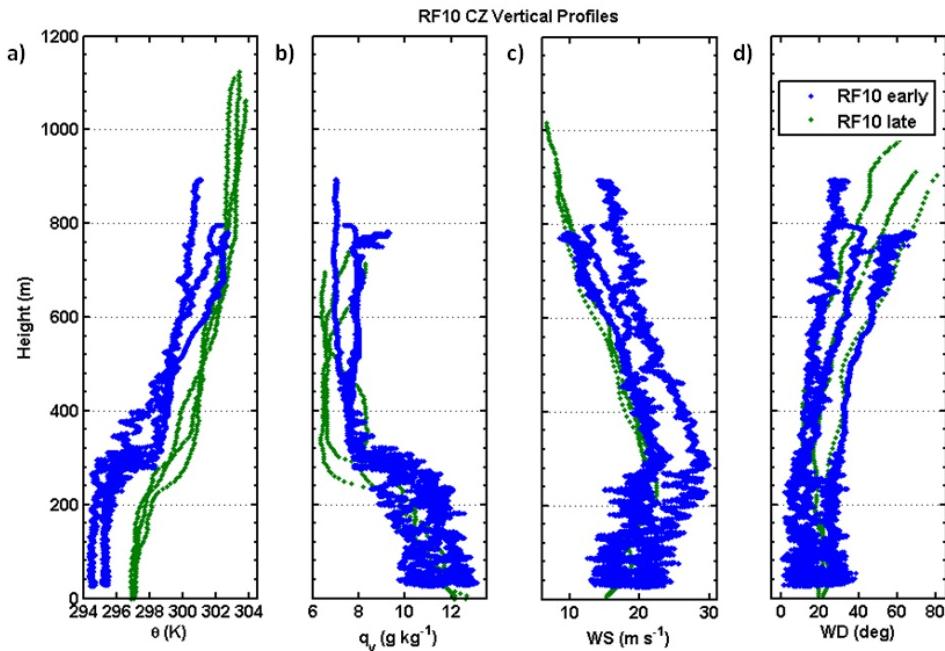
Figure 46.   Selected RF10 vertical profiles of a) potential temperature (K), b) specific humidity (g kg^{-1}), c) wind speed (m s^{-1}), d) wind direction (deg) in the CZ region.

c.   The Offshore Region

Three low-level cross sections (CS-F, CS-G and CS-H), eight soundings and two dropsondes were measured within the Offshore region of RF10. The vertical profiles showed a warm, moist ABL with a stable, highly variable layer above (Figure 47). Wind speed decreased offshore, while temperature and specific humidity increased. Boundary layer winds were weaker than during RF09, but temperature and specific humidity remained the same. The southernmost profile of RF09 was approximately 55 km to the SW of the end of the RF10 flight track, which accounts for the slightly higher maximum potential temperature and specific humidity of RF09 S65 (Figure 40). The three low-level cross sections showed little variability in either potential temperature or sea-surface temperature (less than 0.25 K), and consistently high specific humidity. Wind speed decreased with distance offshore. As with previous flights, the gap outflow resulted in slightly increased variability within the Offshore region with distance from shore, but overall this region remained relatively homogeneous.
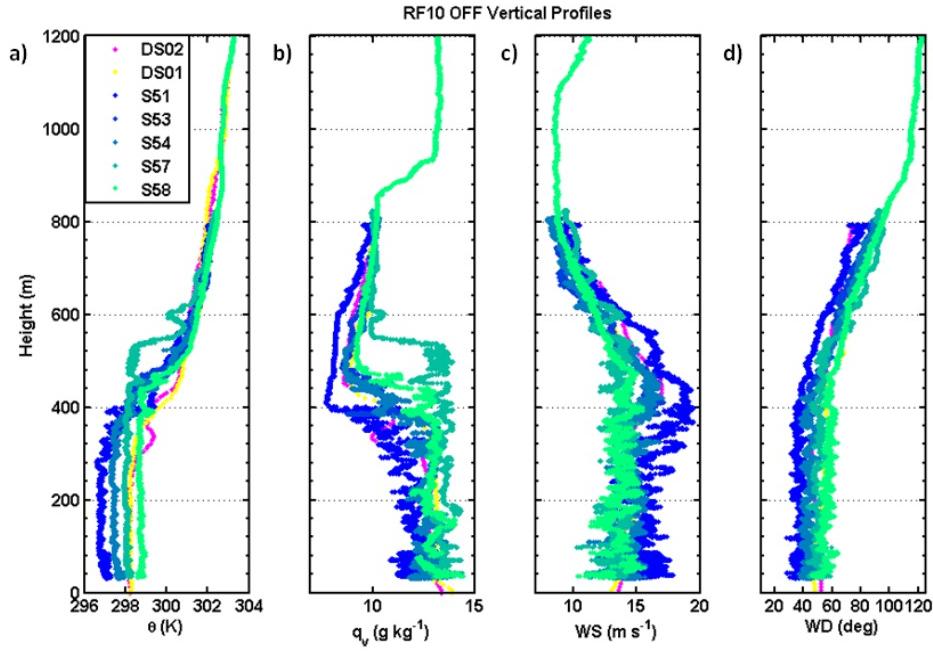
Figure 47.   RF10 vertical profiles of a) potential temperature (K), b) specific humidity (g kg^{-1}), c) wind speed (m s^{-1}), d) wind direction (deg) in the OFF region.

3.   Evolution of the Ocean Mixed Layer

Ocean measurements for Event V are limited to aircraft-measured sea-surface temperature and temperature profiles from AXBTs.   Figure 48 shows the sea-surface temperature from the onboard radiometer at aircraft altitudes less than 50 m for flights RF09 (a) and RF10 (b).   Individual points in the figures are sea-surface temperatures from AXBTs.   For both flights, AXBT sea-surface temperatures agree well with aircraft-measured sea-surface temperatures.

During RF09, the coldest sea-surface temperatures were found just offshore of the NS/CZ boundary and slightly west of the axis of the gap exit.   The ocean response to the gap outflow, which is represented by cooling sea-surface temperatures, was limited to within 185 km of the coast.   South of 14.5°N, no appreciable cooling of sea-surface temperatures was measured.   Closest to the coast, sea-surface temperatures cooled approximately 4 K within the Nearshore region, compared to the pre-event sea-surface temperatures measured during RF08 (Figure 31).   Between RF09 and RF10, the OML

cooled an additional 5–6 K along 16°N (Table 2). Within the Coupling Zone region, the coldest sea-surface temperatures from RF09 (292 K) were found along the eastern side of CS-C, the third line from the coast in Figure 48a.

By RF10, the sea-surface temperatures in this area had rebounded by approximately 4 K (Figure 48b). With the persistent influence of the gap outflow continuing to progress farther offshore, the southward limit of the ocean response has extended down to 14°N, an additional 55 km offshore. The nominal boundary between the Coupling Zone and Offshore regions is apparent in these sea-surface temperature maps, marked by the black arrows (Figure 48). The Coupling Zone extends over the area where the ocean response to the gap outflow results in cooler sea-surface temperatures. Beyond that area is the Offshore region, where the influence of the outflow is limited to the atmospheric boundary layer.
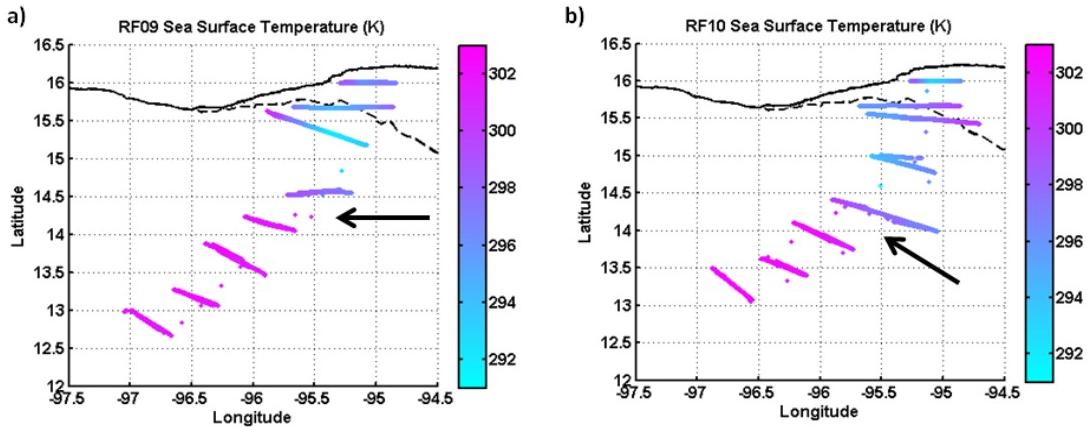
Figure 48.   Sea-surface temperature (K) measured by the C-130 from below 50 m altitude during a) RF09, and b) RF10. Individual points represent the SST from AXBTs.

Similar to the Nearshore region of very cold sea-surface temperatures measured in Event II (Figure 27), a sea-surface temperature minimum was measured during Event V centered at 95.1°W. Figure 49 shows the sea-surface temperature from low-level aircraft legs along 16°N during flights RF09 and RF10. Cooling sea-surface temperatures were centered along the axis of the gap exit and had cooled 1–2 K by RF09, compared with pre-event conditions measured during RF08. Twenty-four hours later, the Nearshore sea-surface temperatures had cooled another 4–5 K. The magnitude of continued cooling is

comparable to the cooling between RF02 and RF03, although the minimum temperature during this event is warmer. A first guess as to the warmer minimum sea-surface temperature is the relative strength of the event. Event V was weaker than Event II in maximum wind speed and stress. However, Event V was of longer duration. The sea-surface temperature minimum was at the axis of the gap exit during Event V, rather than to the east as in Event II. During both events, significant cooling of surface waters occurred within the Nearshore region, and continued to cool as the event progressed. As mentioned in section A.3, this narrow tongue of cold water may be indicative of a narrow surface current forced by the outflow jet. However, since no *in situ* current measurements were made, further investigation using the coupled NCOM simulations is necessary.
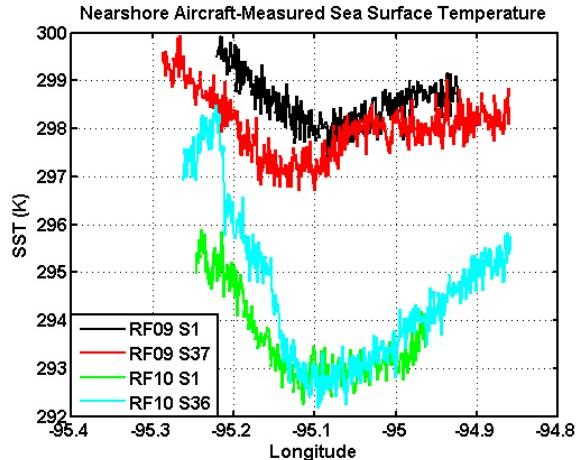
Figure 49.   Aircraft-measured sea-surface temperature (K) within the Nearshore region along 16°N during flights RF09 and RF10.

Available AXBTs from RF09 are limited to the Coupling Zone and Offshore regions. Figure 50a shows the location of the ten successful RF09 AXBTs. The corresponding temperature profiles are shown in Figure 50b. These AXBT profiles clearly show the difference in ocean structure between the Coupling Zone and Offshore regions. The two Coupling Zone profiles, BT14 and BT13 measured colder near-surface waters, a shallower mixed layer, and a raised thermocline. The raised thermocline is indicative of upwelling while the colder mixed layer temperature is indicative of

entrainment mixing of cold water at the bottom of the OML or cooling by surface processes. The Offshore profiles show a warm, deeper OML and deeper thermocline.
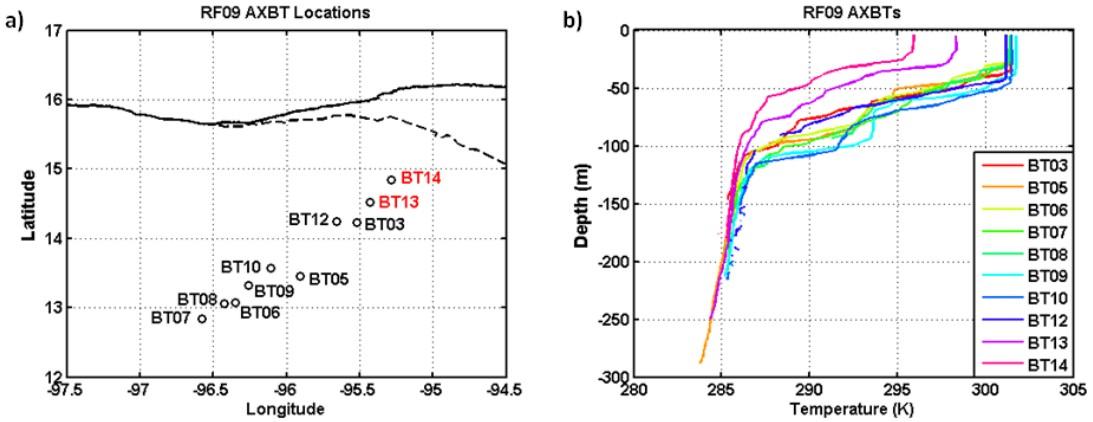
Figure 50.   a) Locations of RF09 AXBTs. CZ AXBTs are in red; OFF are in black. b) Temperature (K) vs. depth (m) profiles for RF09 ABXTs.

AXBTs from RF10 are available from all three outflow regions and support the evolution of the ocean structure between the three regions consistent with RF09 AXBTs (Figure 51). BT01 provides the only Nearshore ocean temperature profile for this event. The ocean mixed layer was approximately 6 K colder and 40 m shallower than the Offshore OML. Six AXBTs were recorded within the Coupling Zone region. BT02, BT03, and BT14, along the axis of the gap exit, each measured a cold, shallow OML, with a very strong, shallow thermocline. Along the axis, the OML cooled 4–5 K, only slightly less than within the Nearshore region. The strength and depth of the thermocline between the Nearshore profile (BT01) and these three Coupling Zone profiles suggest the influence of upwelling from the strong forcing of the outflow jet. The other three Coupling Zone profiles, BT04, BT11 and BT12, were located along the southwest turn in the flight track. Only BT11 recorded a complete profile. BT11 showed that the OML was cooler than the Offshore region by about 2 K, but not as cool as the other Coupling Zone profiles. Similarly, the thermocline was shallower than Offshore, but deeper than within the Nearshore region or the Coupling Zone along the axis of the gap exit. BT11 and BT10 were located 10 km apart on either side of the CZ/OFF boundary and illustrate the strong heterogeneity that existed within the outflow region.

83

Based on the subjective criterion that the Offshore region begins where there is no change in sea-surface temperature, as measured from the aircraft radiometer, BT10 was located within the Offshore region. The OML temperature measured by BT10 was consistent with the very warm OML measured by the Offshore profiles. However, the BT10 profile showed a raised and strengthened thermocline consistent with the BT11 profile measured within the Coupling Zone. It is likely that upwelling raised the thermocline, but the entrainment mixing had weakened enough between these two profiles that there was no noticeable cooling of the OML. Similar to BT10, all six Offshore AXBTs show a very warm OML of approximately 301 K, with a range of less than 1 K. Entrainment mixing was minimal within the Offshore region as shown by the consistently warm OML temperatures. These profiles do show that there was some variability in thermocline and OML depth. Since the depth of the thermocline appeared to show spatial coherence with distance from shore, the change in thermocline depth was likely the result of progressively weaker upwelling, rather than internal waves which can also significantly affect thermocline depth, especially shoreward of the shelf break.
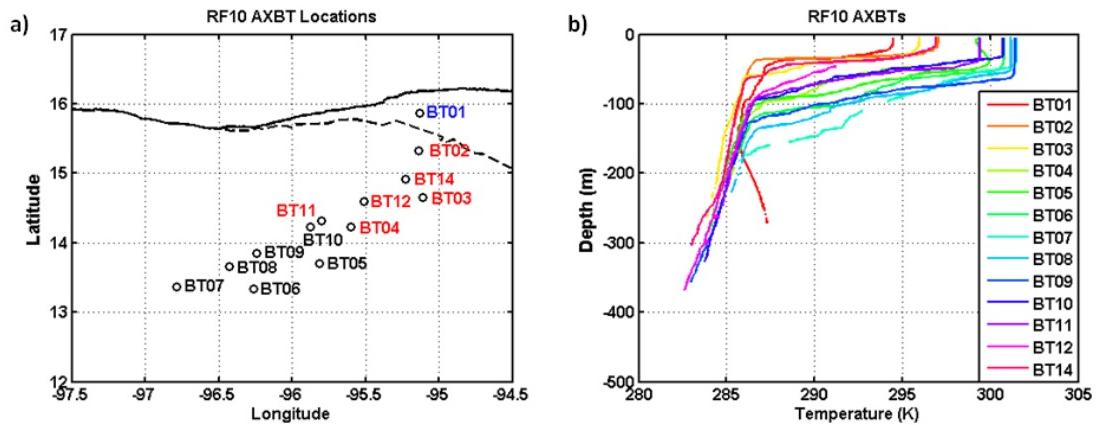
Figure 51.   a) Locations of RF10 AXBTs. NS AXBT is in blue. CZ are in red; OFF are in black. b) Temperature (K) vs. depth (m) profiles for RF10 ABXTs.

Vertical cross sections of ocean temperature from RF09 and RF10 AXBTs are shown in Figure 52. Figure 52a shows the locations of the AXBTs selected for the cross sections. The RF09 cross section (Figure 52b) began in the middle of the Coupling Zone. However, the first ABXT of the cross section showed cold near surface temperatures and no well-mixed layer. The RF10 cross section began within the Nearshore region, where

near-surface temperatures had cooled significantly (Figure 60c). The anomalously cold surface temperature at 150 km was confirmed by co-located aircraft radiometer measurements. A comparison of nearby AXBTs from RF09 and RF10 within the Coupling Zone showed a very different response than during Event II. The Event II response was strong upwelling, while the Event V AXBTs within the red dashed oval in Figure 52 measured very little change in the depth of the 286 K isotherm. The likely reason for this difference between the Coupling Zones of Event II and Event V is location with respect to the core of the outflow jet. Ekman divergence is expected to cause upward Ekman pumping, upwelling, to the east of the outflow jet. To the west, Ekman convergence is expected to cause downwelling. Naturally, there is a region beneath the outflow jet where Ekman transport is relatively constant and therefore vertical motion approaches zero. Both Event II flight tracks were farther to the east than those of Event V. The AXBTs from Event II, which showed strong upwelling, were within the area of Ekman divergence, while the Event V AXBTs within the Coupling Zone were located closer to the axis of the jet. Further offshore, the downwelling response during Event V was similar to that of Event II. The depth of the 286 K isotherm increased by 45–70 m over the last 100 km of each flight track, giving an estimated downwelling rate of 58 m day^{-1}, almost three times as strong as during Event II. The estimated downwelling during both events was due to convergence near the leading edge of the outflow jet.
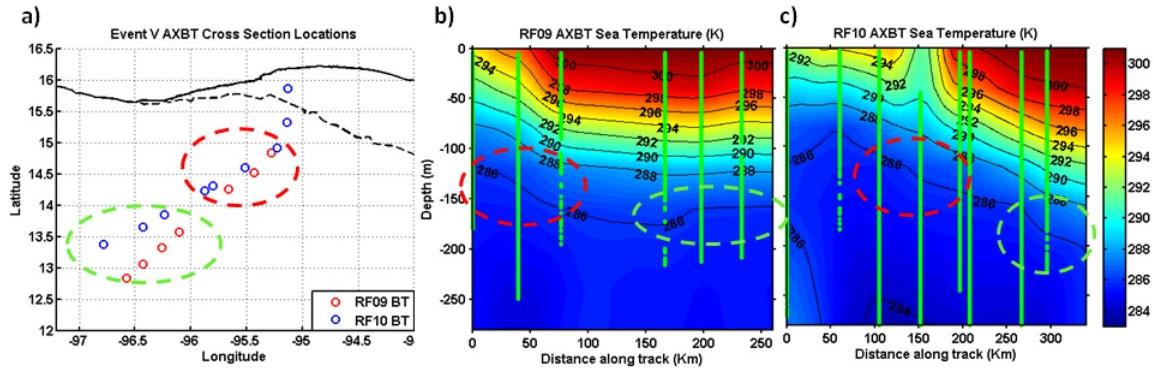
Figure 52.   a) Locations of RF09 (red) and RF10 (blue) AXBTs used for temperature cross sections. b) Vertical cross section of sea temperature (K) from select along track RF09 AXBTs. c) Vertical cross section of sea temperature (K) from select along track RF10 AXBTs.

C. SUMMARY OF CASE STUDIES

Large-scale differences between Events II and V, such as the pressure gradient along the gap, or the maximum wind speed within the outflow, are driven by differences in the synoptic forcing of the gap winds through the Chivela Pass. QuikSCAT imagery of surface winds from 48 hours after the onset of each event (best pass available) showed that Event II outflow winds remained strong and covered most of the GoT, while Event V winds were weaker and covered a much smaller area within the GoT (Figure 53). The maximum jet wind speed was 35 m s^{-1} during Event II, compared with 28 m s^{-1} during Event V. Boundary layer air was colder during Event II and sea-surface temperatures experienced more significant cooling. However, the boundary layer air throughout all three outflow regions was drier during Event V. Despite these differences, some general patterns exist in the downwind development and temporal evolution of both the atmospheric boundary layer and ocean mixed layer.
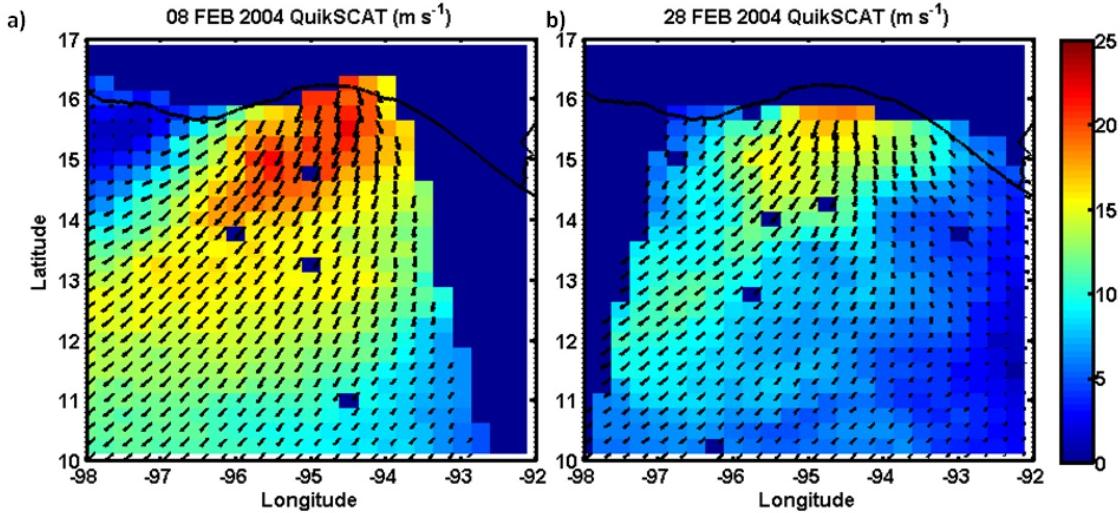
Figure 53. Surface wind speed and direction from the SeaWinds on QuikSCAT Level 3 Daily, Gridded Ocean Wind Vectors data set for a) 08 February 2004, and b) 28 February 2004. Available from the Physical Oceanography Distributed Active Archive Center at the NASA Jet Propulsion Laboratory (http://podaac.jpl.nasa.gov/quikscat/).

As gap winds flow from the gap exit over the Gulf of Tehuantepec, an elevated outflow jet forms along the axis of the gap exit. The reduced surface roughness of the ocean results in acceleration of the winds and an elevated jet maximum, which forms

approximately 40 km from the coast. From this jet maximum, wind speed decreases with distance from shore. The top of the boundary layer, just above the elevated jet, is highest at the coast and along the jet axis. Away from the jet axis, and away from shore, the boundary layer height decreases, until it reaches a minimum. The minimum coincides with the minimum cooling of sea-surface temperatures. Following the wind speed pattern, the wind stress and turbulent kinetic energy decrease away from the coast. The coldest, driest boundary layer air is found closest to the coast and centered along the axis of the gap exit.

Sea-surface temperatures in some areas cool dramatically in response to the gap outflow within the Nearshore and Coupling Zone regions. Initially, the outflow was divided into three regions based on the cooling of sea-surface temperatures. However, it is evident from observations that the response of the ABL differs among these three regions as well.

To summarize the characteristics of each region from the aircraft observations discussed, the mean properties and fluxes are given in Table 2 and Table 3. These values were calculated from low-level aircraft measurements within each region. Table 2 lists the mean wind speed, potential temperature, sea-surface temperature, and specific humidity by region and flight. Because of the high variability in sea-surface temperature, the minimum value of sea-surface temperature is listed in parentheses. Table 3 lists the mean wind stress, TKE, sensible heat flux and latent heat flux by region and flight. The temporal changes to each property during each event vary by region, with exception of the minimum sea-surface temperature, which cools in all regions.

Table 2.   Mean values of wind speed (m s^{-1}), potential temperature (K), sea-surface temperature (K), and specific humidity (g kg^{-1}) by region and flight.

Region	Variable	Event II		Event V	
		RF02	RF03	RF09	RF10
NS	WS (m s^{-1})	24.8	15.0	20.5	10.2
	ϴ (K)	293.4	296.4	296.7	294.9
	SST (K)	292.6 (291.3)	293.7 (289.2)	298.3 (297.2)	293.8 (292.6)
	q_v (g kg^{-1})	10.7	10.9	10.7	10.2
CZ	WS (m s^{-1})	20.2	17.2	17.2	18.9
	ϴ (K)	295.8	295.3	297.1	295.1
	SST (K)	297.2 (296.5)	296.5 (295.1)	298.3 (295.1)	296.1 (293.9)
	q_v (g kg^{-1})	12.6	12.3	11.1	11.1
OFF	WS (m s^{-1})	12.0	12.4	12.4	13.5
	ϴ (K)	298.6	297.2	298.5	297.4
	SST (K)	301.1 (300.1)	301.3 (300.0)	301.8 (301.2)	300.2 (296.1)
	q_v (g kg^{-1})	15.7	14.8	13.0	12.5

Table 3.   Mean values of wind stress (N m^{-2}), TKE (m^2 s^{-2}), sensible heat flux (W m^{-2}) and latent heat flux (W m^{-2}) by region and flight.

Region	Variable	Event II		Event V	
		RF02	RF03	RF09	RF10
NS	stress (N m^2)	1.36	0.06	0.83	0.47
	TKE (m^2 s^{-2})	4.14	0.58	2.83	1.84
	sehflx (W m^{-2})	-29.6	-14.9	19.3	-20.9
	lahflx (W m-2)	286.1	46.3	654.8	191.0
CZ	stress (N m^2)	1.09	0.39	0.55	0.67
	TKE (m^2 s^{-2})	3.33	2.76	1.84	2.16
	sehflx (W m^{-2})	23.5	-1.1	9.1	10.1
	lahflx (W m-2)	480.2	246.8	439.2	348.5
OFF	stress (N m^2)	0.24	0.12	0.31	0.41
	TKE (m^2 s^{-2})	0.86	0.49	1.05	1.19
	sehflx (W m^{-2})	14.0	13.3	31.8	28.6
	lahflx (W m-2)	302.9	139.8	468.6	465.8

The Nearshore region, shoreward of the 500 m bathymetry curve, responded quickly to the influence of the gap outflow. During the first flight of each event, this region was the location of the coldest, driest boundary layer air, strongest winds and surface wind stress. The TKE was also strongest within this region during the first flight due to strong vertical wind shear, although in generally stable boundary layer conditions. The jet was at its highest elevation at the gap exit. The variability of potential temperature was highest within the Nearshore region.

The minimum sea-surface temperatures are listed in Table 2 because the mean value does not adequately convey the strong cooling that takes place within the Nearshore region. Because of the high spatial heterogeneity of sea-surface temperature within this region, the coldest sea-surface temperatures were often found in a very narrow region along the axis of the outflow. Sea-surface temperatures began cooling immediately within the Nearshore, but were coldest during the second flight. Coastal upwelling and entrainment of cold water from below the thermocline due to offshore forcing resulted in the continued cooling of sea-surface temperatures during the event development stage, until wind stress began to weaken. The deepening of the OML due to persistent wind forcing is not conclusive. The Nearshore AXBT profiles showed a combination of shallow, but very cold, mixed layers, and several profiles where the upwelling had raised the thermocline to the surface resulting in no mixed layer.

The generally stable boundary layer conditions, especially during the daytime, were the result of cold sea-surface temperatures and relatively warm air advection due to diurnal heating of the boundary layer air over land. Sensible heat flux was negative due to the stable surface layer. The Nearshore region generally had the weakest latent heat flux of the three regions due to the coldest sea-surface temperatures, and driest air within the boundary layer. Comparison of the moistening rates due to the latent heat-flux divergence and the horizontal advection found that they were of similar magnitude and therefore resulted in a fairly constant water vapor specific humidity within the Nearshore region from the first flight to the second. Additionally, the latent heat flux was weaker during the second flight due to the continued sea-surface temperature cooling and increased boundary layer stability. Although no current measurements were made,

Nearshore aircraft legs parallel to the coast measured strong sea-surface temperature gradients, and a region of very cold sea-surface temperatures that may have resulted from the presence of a southward coastal jet near the surface and the associated upwelling at the coastline.

The exception within the Nearshore region was flight RF09 when the sea-surface temperatures had not yet cooled significantly and the boundary layer remained unstable. Although the wind speed, wind stress and TKE were high, the sensible heat flux was weakly positive and upward latent heat flux was very strong due to warm sea-surface temperatures and an unstable boundary layer. Because RF09 was measured very shortly after the onset of Event V (11 hours), it is possible that the OML, which drives the boundary layer stability and thus the sensible and latent heat fluxes, had not responded as much as measured in the first flight of Event II.

The Coupling Zone region begins at the 500 m bathymetry contour where the bottom begins to slope sharply down to the deep Middle America Trench and continues to the furthest offshore extent of measured sea-surface temperature cooling. During the first flight, the wind speed, wind stress, and TKE were slightly lower than within the Nearshore region. However, during the second flight, the strongest winds, highest wind stress and TKE were within the Coupling Zone, suggesting that during the decay stage of the outflow event, the strongest forcing on the upper-ocean was within this region. Boundary layer air within this region warmed from the Nearshore to the Coupling Zone, but was cooler during the second flight. The latent heat flux was at a maximum within this region, while the specific humidity increased slightly, suggesting a slight imbalance between latent heat-flux divergence and horizontal advection to the net moistening rate of the boundary layer.

The elevation and strength of the jet decreased from the first to second flight and with increasing distance offshore. The boundary layer height decreased away from the coast, with the minimum located at the boundary of the Coupling Zone and Offshore regions. The anticyclonic turning of the jet generally occurred within this region. Weak variability across aircraft cross sections from Event V suggests that these cross sections were mostly contained within the outflow jet so no conclusions can be made about the

ABL response to either side of the jet for this event. This, however, does imply that the aircraft track successfully followed the turning of the jet. Flight tracks for Event II were oriented more N-S and did not closely follow the turning of the jet.

Sea-surface temperatures also cooled significantly within the Coupling Zone region. A persistent cold pool was located within the Coupling Zone and resulted in weak negative sensible heat flux between outflow events. The gap outflow events induced even more cooling of the OML. In general, the Coupling Zone sea-surface temperatures did not cool as much as within the Nearshore region, but did continue to cool from the first to the second flight. However, there were some small areas where the sea-surface temperature was colder than within the Nearshore region and showed a fast rebound response by the second flight. The coldest sea-surface temperatures within this region were generally closer to shore near the Middle America Trench, with the magnitude of cooling decreasing offshore. Upwelling and entrainment appeared to be strong mechanisms of OML cooling in this region based on the general decrease in thermocline depth and OML temperature. Unlike the Nearshore region, a well-defined ocean mixed layer remained throughout the event, but was generally shallower than within the Offshore region. The Coupling Zone remained slightly unstable throughout the events. Latent heat flux weakened from the first to second flight, and sensible heat flux was highly variable.

Within the Offshore region the atmospheric boundary layer was warmer and more moist than the other two regions, with much less spatial variability. Northerly winds continued to flow through this region, with wind speed weakening with distance offshore. The wind speed within this region increased from the first to the second flight which may be due to large-scale forcing. Sensible heat flux remained weakly positive throughout the events and latent heat flux weakened from the first to the second flight due to slightly cooler sea-surface temperatures. The ocean response was minimal in this region. The mean sea-surface temperatures changed by less than 0.2 K for Event II and cooled by 1.6 K during Event V. During Event II, the change to the minimum sea-surface temperature was only -0.2 K, while during event V, the minimum sea-surface temperature cooled by

5.1 K. The mixed layer depth remained fairly consistent, but there was some variability within the thermocline that could be due to weak upwelling or internal waves.

The co-located air and ocean measurements from GOTEX provide a detailed view of the observed phenomena of gap outflow events. While most of the ABL and OML characteristics agree well with previous studies of Tehuano events, the differences in the air-ocean boundary layer response between the three regions has not been previously identified. During the intensification stage of the outflow event, the strongest forcing of the upper-ocean is within the Nearshore region. During the decay stage, the strongest forcing is within the Coupling Zone. Moistening processes are generally balanced by latent heat-flux divergence and advection of dry air. Sea-surface temperatures cool the most within the Nearshore region, resulting in increased stability of the boundary layer. Coastal upwelling due to ageostrophic forcing that raises the thermocline, and entrainment mixing due to turbulence that cools the OML are believed to be the dominant mechanisms for cooling of the sea-surface temperature. Mesoscale horizontal advection may also contribute. Within the Coupling Zone and Offshore regions, entrainment mixing, which decreases with turbulence offshore, cools the OML temperature by mixing cool water from the base of the thermocline into the sustained ocean mixed layer. Analysis of the fully coupled COAMPS/NCOM simulations for these events will provide insight into the evolution of the ABL and OML within each of these regions beyond the limits of the available GOTEX data.

V. SIMULATED EVOLUTION WITH COAMPS/NCOM

A. SIMULATED GAP WIND AND GAP OUTFLOW

Although this study does not include a comprehensive analysis of the synoptic conditions initiating each gap wind event, it is helpful to begin the analysis of the simulated event evolution by looking at the sea level pressure (SLP) and wind speed along the gap for the entire GOTEX simulation period. Figure 54 shows the sea level pressure and wind speed at the entrance and exit of the Chivela Pass, and 50 km offshore in the Gulf of Tehuantepec. Five periods of high SLP occurred at the gap entrance during February 2004. During each period, an along-gap pressure gradient formed, which induced accelerated winds through the gap. Each of these corresponds to a gap outflow event measured by GOTEX. For all events, the strongest pressure gradient was between the entrance and exit of the gap, as expected, while the SLP difference between the gap exit and 50 km offshore was much smaller.

Based on wind speed at the gap entrance, and the pressure-gradient difference, the estimated wind speed at the gap exit without frictional effects is approximately 37 m s^{-1} for Event II and 32 m s^{-1} for Event V, which is highly over-estimated (Overland and Walter 1981). The time series of wind speed shows some acceleration of winds along the gap, but the significant increase in magnitude occurred between the gap exit and 50 km offshore, where frictional effects and surface roughness decrease as the air column moved over the water. The strongest event was Event II, from 6–8 February 2004, with maximum 10 m winds of 22.4 m s^{-1} and an along-gap pressure gradient of 8 mb.
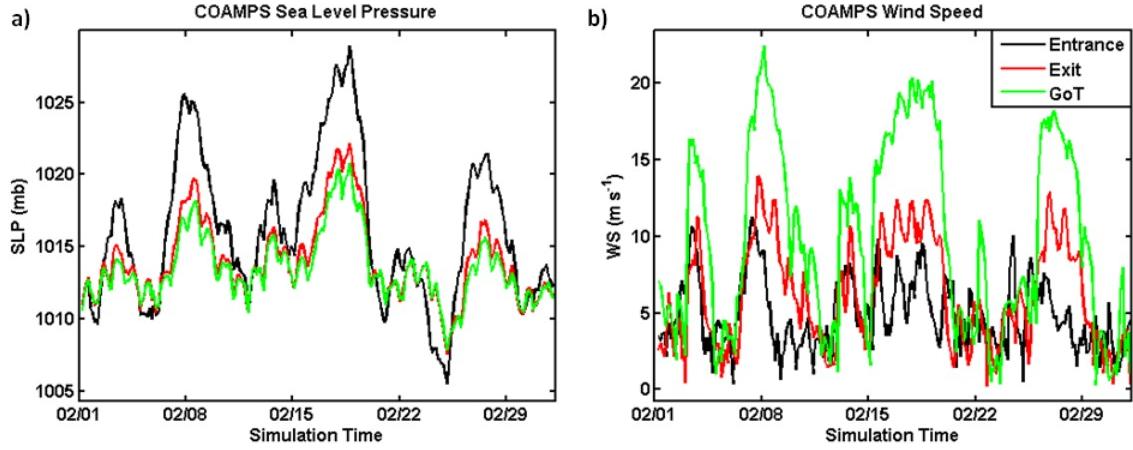
Figure 54.   Time series of COAMPS a) sea level pressure (mb) and b) 10 m wind speed
(m s⁻¹) at the gap entrance, exit, and 50 km offshore in the Gulf of Tehuantepec
(GoT) for February 2004.

Based on the aircraft observations, which were limited in spatial and temporal coverage, three regions were identified within the gap outflow. Here, these three regions will be examined using COAMPS/NCOM simulations, which provide continuous spatial coverage and greater temporal detail to further analyze differences in the atmospheric response within each of these regions. For each outflow region, the time evolution of surface fluxes and boundary layer properties for the entire GOTEX time period were evaluated using a 'regional' average (Figure 55). Because the aircraft observations showed that the response within the Nearshore region varied greatly from the coast to the edge of the continental shelf, averages along two distinct latitudinal lines were used to illustrate the variability. Within the Coupling Zone and Offshore regions, larger areas were averaged together to quantify the overall response within each region. Figure 55 shows the longitudinal lines and areas used for averaging in the mean time series that follow in Figures 56, 57, and 58.

94
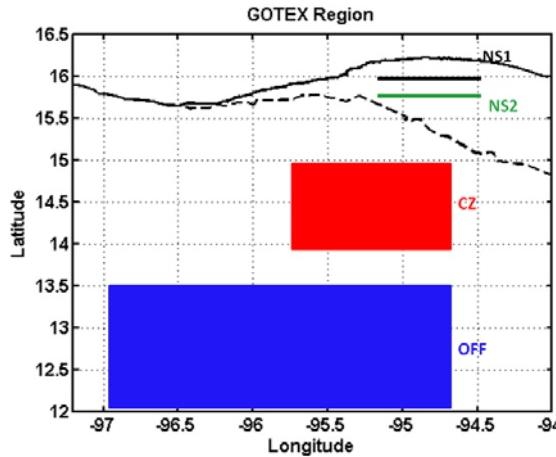
Figure 55.   Map of the GOTEX region. NS1 (black), NS2 (green), CZ (red) and OFF (blue) denote the four locations from which COAMPS model output were used in the temporal variations from the Nearshore (NS1 and NS2), the Coupling Zone, and the Offshore regions. Two latitudinal lines were chosen in the Nearshore due to large spatial variability. Broader regions were used for the CZ and OFF regions.

Figure 56a clearly shows the strong typical diurnal variations of 2–3 K seen in potential temperature between events, which decreases in magnitude further offshore. The weaker gap outflow events, such as Event I and Event II are masked by the diurnal variability and only the three strongest (coldest) outflow events can be clearly identified from the temporal variation of the 10 m potential temperature (Figure 56a).   During events, the diurnal variation persisted but was slightly weaker.   The coldest mean potential temperature was from the two Nearshore locations, warming with distance from shore, which is consistent with the aircraft observations (Chapter IV). This temperature variation with distance offshore is only apparent during the strong gap events.   The specific humidity also decreased significantly during the development stage of each event as expected (Figure 56b).   The driest air was within the Nearshore region, with little difference between NS1 and NS2. The Coupling Zone and Offshore regions showed a progressive increase in moisture. In all three regions, the mean specific humidity shows much greater variability than the aircraft observations.
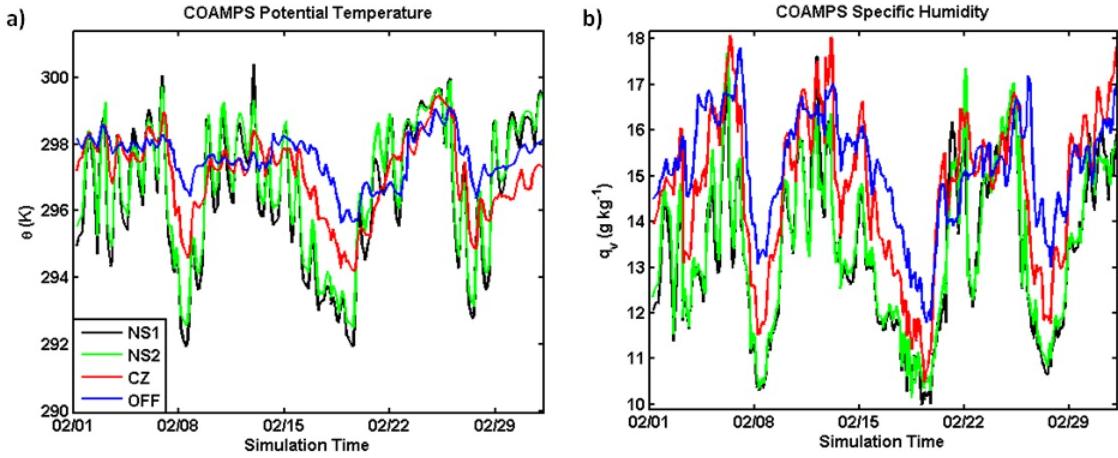
Figure 56.   Time series of COAMPS a) 10 m potential temperature (K) and b) 10 m specific humidity (g kg^{-1}) averaged for the regions shown in Figure 55 during February 2004.

Strong wind stress continued from the Nearshore region through the Coupling Zone for all simulated events (Figure 57a). The maximum wind stress was actually along NS2, just before the NS/CZ boundary for every strong event. Often, the wind stress within the Coupling Zone was comparable to both NS1 and NS2 and may exceed those from NS1 at the peak of jet development for the stronger events (Events II, IV, and V). There was a significant decrease in wind stress within the Offshore region. Between outflow events, wind stress was weak throughout the GoT. Low-level (10 m) wind speed (not shown) showed a similar pattern. As expected, sea-surface temperatures cooled dramatically during each gap outflow event (Figure 57b). In all events, cooling sea-surface temperatures are the most apparent in the Nearshore and Coupling Zone regions, while in general, the Coupling Zone had a slower rebound than the Nearshore region. In fact, in Events IV and V, the Coupling Zone in the model saw the coolest water in the entire region. Cooling in the Offshore region is most apparent during the stronger events (II, IV, and V). There also appears to be a lag of 18 hours on average between the minimum sea-surface temperature from the coast to the Coupling Zone and a longer time lag, sometimes 24 hours, to the Offshore region.

Within both the Nearshore and Coupling Zone regions, the sea-surface temperatures began to rebound as soon as the wind stress weakened. The speed with

96

which the sea-surface temperatures rebound depends on the region and is event specific. The Nearshore locations appear to rebound much more quickly than the Coupling Zone during the first four events, while all regions rebound slowly during Event V, in which the modeled sea-surface temperature is much colder than all other regions.
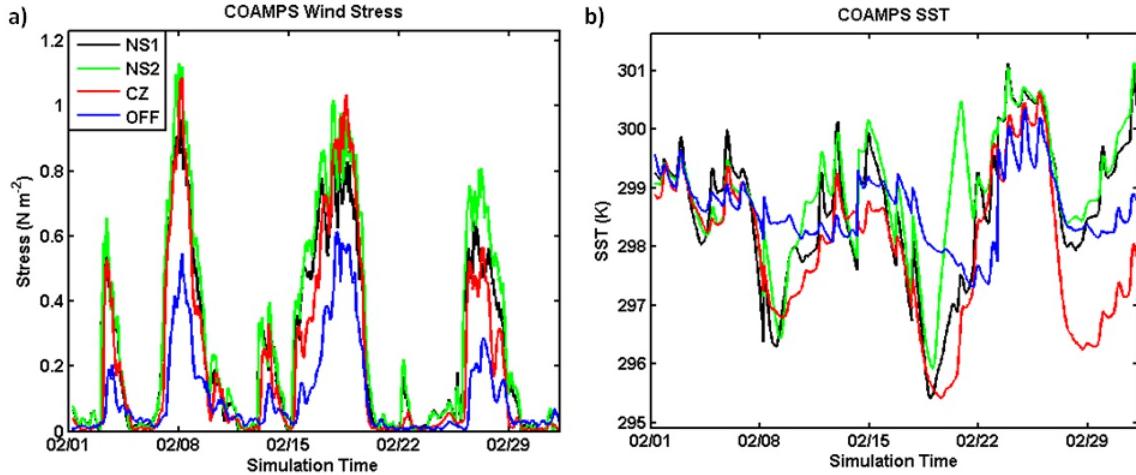
Figure 57.   Time series of COAMPS a) surface wind stress (N m^{-2}) and b) sea-surface temperature (K) averaged for the regions shown in Figure 55 during February 2004.

Sensible and latent heat fluxes over the Gulf of Tehuantepec changed significantly during the gap outflow events (Figure 58). Between outflow events, sensible heat flux was generally negative and small in the Coupling Zone and nearly zero in the Offshore region due to weak wind and relatively small air-sea temperature difference. Nearshore, sensible heat flux showed small diurnal fluctuations between events. During gap outflow events, there was strong upward sensible heat flux within the Nearshore and Coupling Zone regions modified by diurnal variations on the smaller magnitudes. However, negative sensible heat flux may be present at the decaying stage of the outflow in the Coupling Zone, extending to one to three days after the end of the event. Latent heat flux remained positive throughout the simulation period. When sea-surface temperatures cooled significantly the corresponding boundary layer air was very dry, resulting in consistent upward latent heat flux. Between events, latent heat flux ranged from 50–200 W m^{-2}. During events, latent heat flux within the Nearshore and Coupling Zone regions increased to 400–700 W m^{-2}, while the Offshore region increased

97

to 200–400 W m^{-2}. The strongest latent heat flux was almost always along NS2 at the boundary between the Nearshore and Coupling Zone regions.
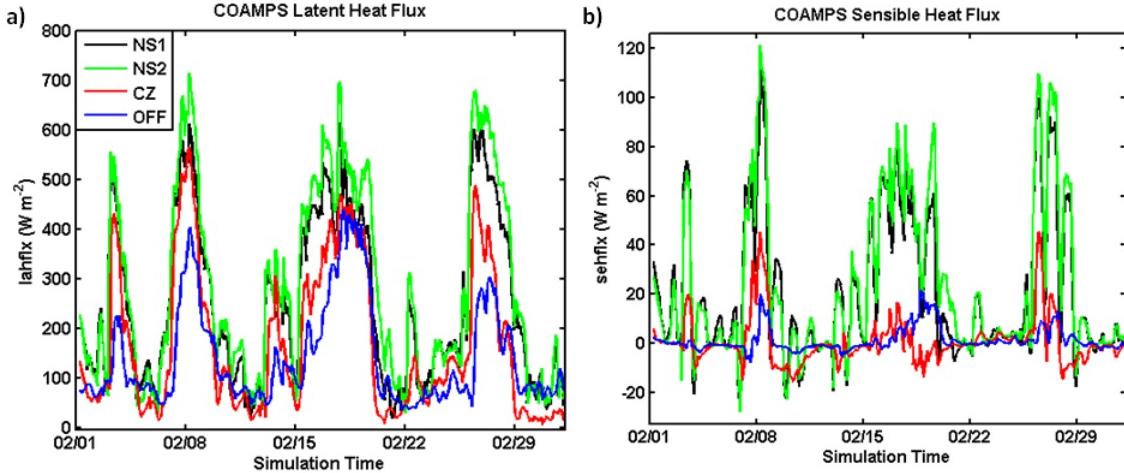
Figure 58.   Time series of COAMPS a) latent heat flux (W m^{-2}), and b) sensible heat flux (W m^{-2}) averaged for the regions shown in Figure 55 during February 2004.

The COAMPS time series show the general patterns of boundary layer properties and surface fluxes during the GOTEX simulation period. Differences between the identified outflow regions seen in the aircraft observations are supported by the COAMPS simulations. Further details of the simulated evolution of the outflow are presented in the following sections for Events II and V.

B.   EVENT II: 6–10 FEBRUARY 2004

1.   Simulated Evolution of the Atmospheric Boundary Layer

Event II began at approximately 1800 UTC on 6 February 2004 and lasted until 0300 UTC on 08 February 2004. This relatively short event was the strongest during the GOTEX period, February 2004. Wind speed and direction at heights of 30 m, 365 m, and 660 m for 1500 UTC on 7 and 8 February are shown in Figure 59 and correspond to the beginning of flights RF02 and RF03, respectively. At 30 m, a broad wind jet with winds greater than 20 m s^{-1} flowed offshore along the axis of the gap exit. Along the core of the jet, northerly winds reached south to 12.5°N before beginning to turn anticyclonically. At the outer edges of the outflow jet anticyclonic (cyclonic) turning began just offshore to the west (east) of the jet. To the east, there was an area of weak wind speed and

convergence where the east edge of the outflow jet appeared to merge with a secondary jet. A secondary wind maximum east of the Chivela Pass jet at 365 m and 660 m confirmed that this secondary jet was a separate feature from the main jet. No previous studies have been documented on the existence of a secondary jet east of the Chivela Pass. However, it is apparent that the flow of this secondary jet affects the downwind evolution on the east side of the main jet. Further discussion on this subject will be presented in Chapter VII.

The wind fields from 365 m and 660 m show that the outflow jet strengthened with height and the strongest winds were within a narrow core at the axis of the gap exit, especially nearshore (Figure 59). The lower panels in Figure 59 show the wind fields 24 hours later corresponding to the beginning of RF03, when the outflow began to weaken. Although the maximum wind speed decreased by only 4 m s^{-1}, the area of the wind maximum decreased and the degree of curvature to the west also decreased.
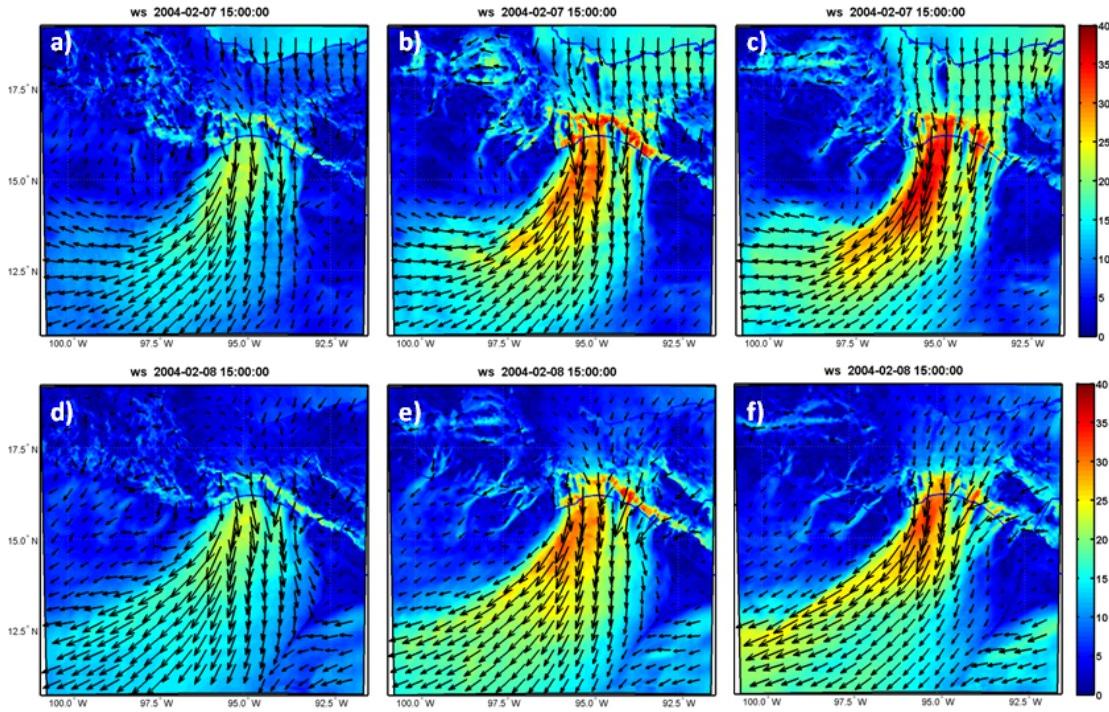
Figure 59.   COAMPS wind speed (m s^{-1}) with wind vectors at 1500 UTC on 7 February 2004 at a) 30 m , b) 365 m , and c) 660 m and on 8 February 2004 at d) 30 m , e) 365 m , and f) 660 m.

Figure 60 depicts the longitudinal-height cross section of wind speed and potential temperature from COAMPS along 16°N in the Nearshore region. The Nearshore structure of the simulated outflow jet was similar to that observed during GOTEX. The outflow jet has an elevated maximum of 32 m s^{-1} at 800 m, just east of the axis of the gap exit. The cold air mass extended from the surface to the level of maximum winds and expanded slightly farther east. Minima in both wind speed and potential temperature suggest that the secondary jet to the east was a distinct feature. During RF02, on 7 February, the eastern edge of maximum winds and the coldest air temperatures have fairly strong horizontal gradients where the model shows abrupt wind reduction accompanied with a warming of a reasonably well-mixed boundary layer east of the jet core. By 8 February, the jet maximum had decreased in strength and elevation. Although the eastern boundary of the jet is still near 60 km east of the axis of the gap exit, the wind speed is reduced and there is strong vertical wind shear above the shallow atmospheric boundary layer.
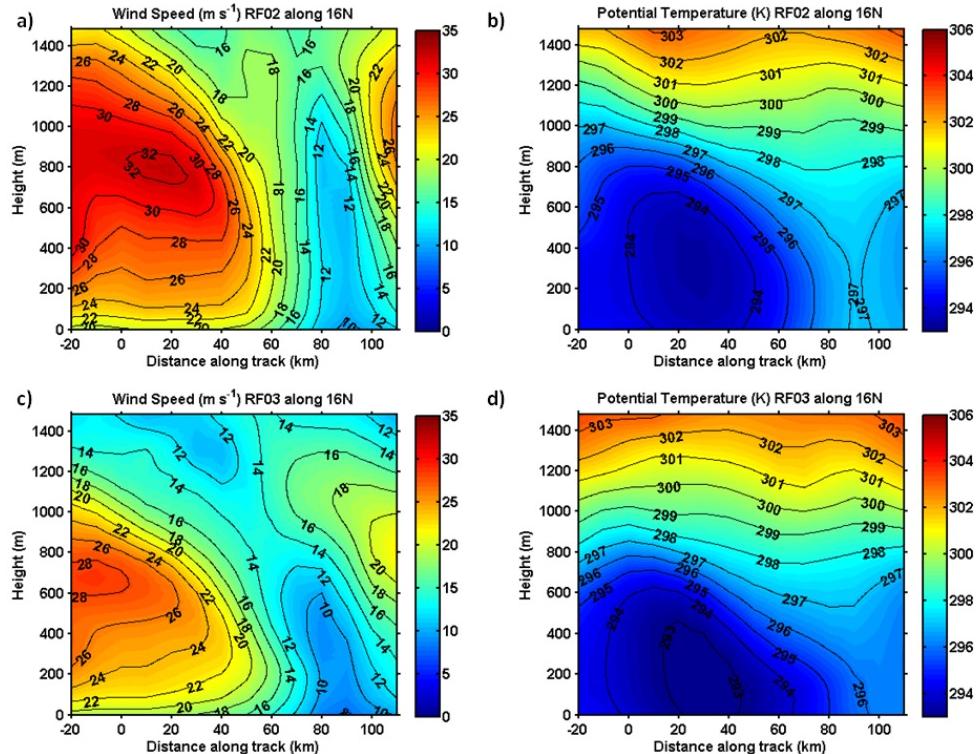
Figure 60. Cross sections along 16°N at 1800 UTC on 7 February 2004 of COAMPS a) wind speed (m s^{-1}) and b) potential temperature (K); and at 1800 UTC on 8 February 2004 of COAMPS c) wind speed (m s^{-1}) and d) potential temperature (K). The 0 km point on the horizontal axis identifies the axis of the gap exit.

As suggested by the temporal evolution of wind speed in along the gap and just offshore (Figure 54b), the jet wind speed increased as it moved over the Nearshore and sometimes the Coupling Zone regions within the GoT. Figure 61 shows the COAMPS cross sections of wind speed (upper) and potential temperature (lower) at 15.5°N, 14.5°N, and 13.5°N at 1500 UTC on 7 February 2004. Although slightly lower in elevation, the jet maximum increased in strength from 15.5°N to 14.5°N. Moving offshore, the location of the jet moved west away from the axis of the gap exit. Zonal (*u*-component) wind speed also increased as the jet turned anticyclonically (not shown). The TKE was strongest within the lowest 100 m and moved westward under the jet maximum. Unlike the strongest winds, the cold air remained centered along the axis of the gap exit within the Nearshore and Coupling Zone regions, but spread out horizontally and warmed throughout the event. The gap outflow brought dry air into the region, with the driest air slightly to the west of the gap exit (not shown). Specific humidity was lowest within the Nearshore region, and continued to increase in all regions throughout the event. At 15.5°N, the west side of the outflow was defined by very strong horizontal wind gradient and a very strong temperature gradient. The east side of the outflow was not as clearly defined. It is likely that the asymmetry in the outflow structure is due to the asymmetric topography to either side of the Chivela Pass. To the west, higher mountains block the cold northerly flow more than the slightly lower mountains to the east. Additionally, to the east there is a second, smaller gap which funnels cold air and strong winds into the GoT and creates a smaller jet which paralleled the main jet beyond approximately 100 km offshore.
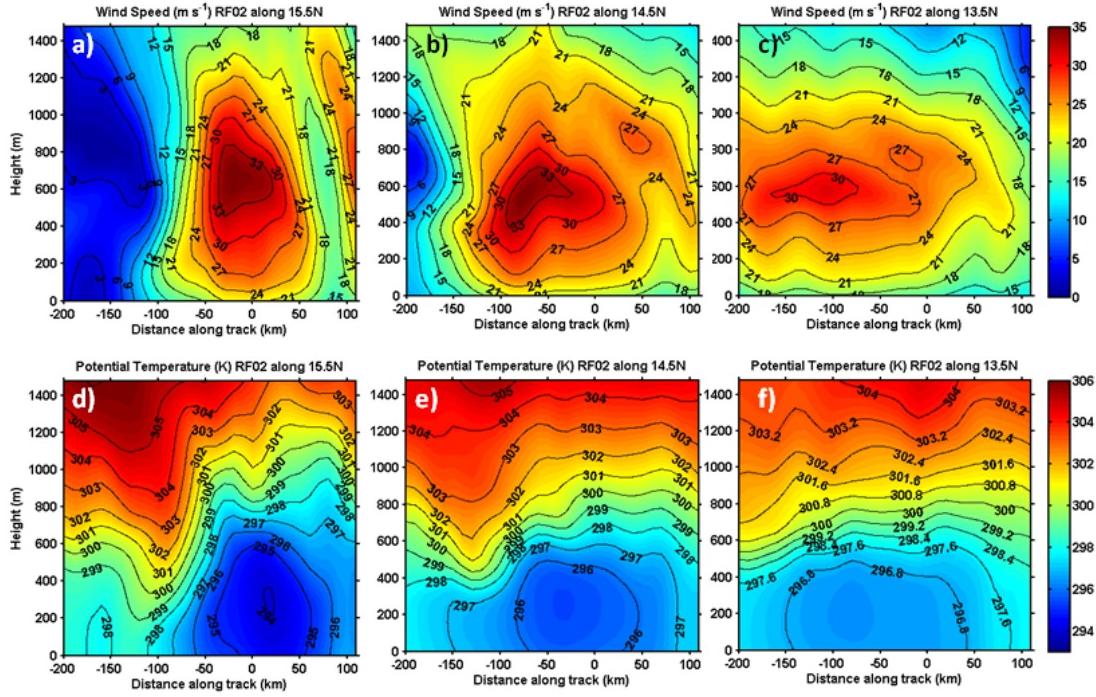
Figure 61.   Cross sections along 15.5°N (a, d), 14.5°N (b, e) and 13.5°N (c, f) of COAMPS wind speed (m s^{-1}, a-c) and potential temperature (K, d-f) at 1500 UTC on 7 February 2004. The 0 km point on the horizontal axis identifies the axis of the gap exit.

2.   Simulated Evolution of the Ocean Mixed Layer

Previous studies of the ocean response to gap outflow events have discussed the formation of an anticyclonic ocean eddy, without the symmetric dipole response of a cyclonic eddy. Twenty-four hours prior to the onset of Event II, three major features were present in the surface current fields of NCOM. Surface current speed and direction are shown in Figure 62 for approximately 24 hours prior to event onset (5 February, Figure 62a), three hours after event onset (6 February, Figure 62b), at the beginning of RF02 (7 February, Figure 62c), and at the beginning of RF03 (8 February, Figure 62d). Prior to the event, three distinct features were present in the surface circulation. A large anticyclonic eddy to the west centered at 14.5°N, 99°W, with currents from 0.5–0.8 m s^{-1}. A second large anticyclonic eddy was located just beyond the southeast extent of the domain, with the NW quadrant visible in the NCOM fields. Covering most of the persistent cold pool in sea-surface temperature, a large, cyclonic circulation was centered

at 14°N, 95°W. As the outflow event began, the NE quadrant of the circulation strengthened, increasing the alongshore flow toward the head of the Gulf, while the eastward flow along the southern portion of the circulation weakened (Figure 62b). By the beginning of RF02 (Figure 62c), strong SW currents had formed beneath the outflow. Only a weak cyclonic circulation remained, with the eastward return branch very weak. By the beginning of RF03 (Figure 62d), westward surface currents dominated the majority of the GoT.
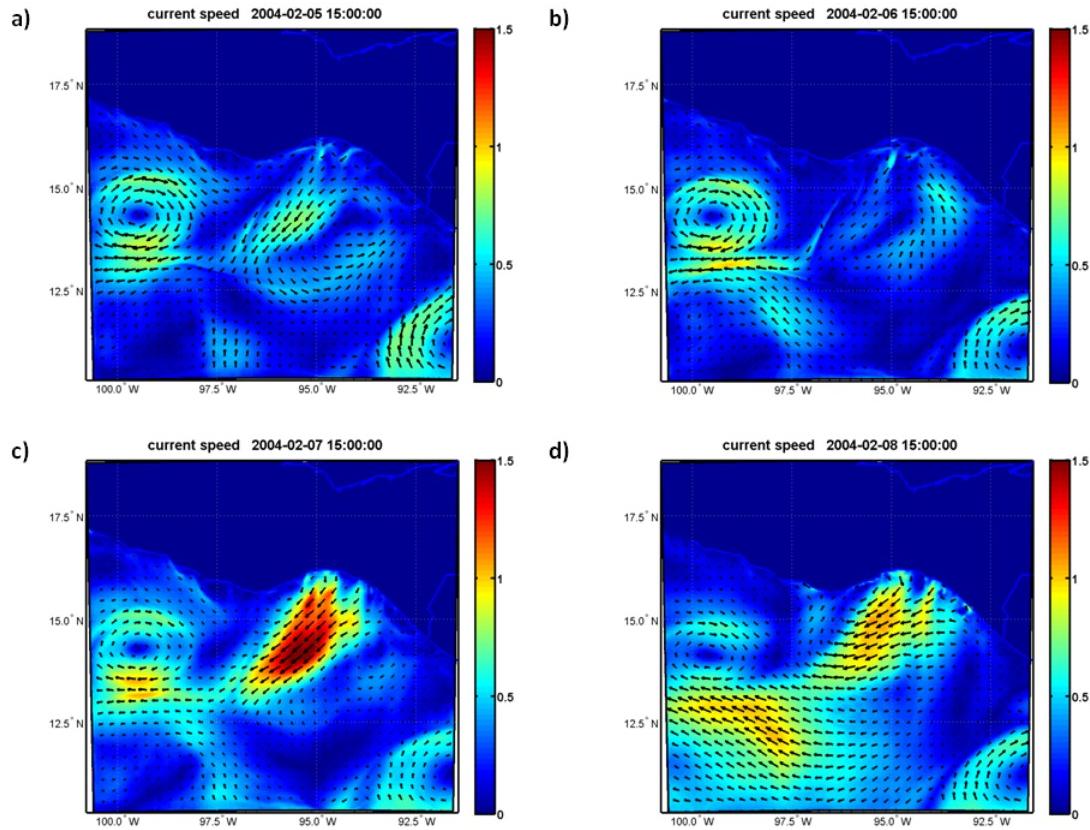
Figure 62.   NCOM surface current speed (m s^{-1}) and direction at 1500 UTC on 5 (upper left), 6 (upper right), 7 (lower left), and 8 (lower right) February 2004.

As seen in Figure 62, strong surface currents formed beneath the gap outflow during Event II which significantly affected the evolution of the ocean mixed layer. Figure 62c shows strong offshore flow within the Nearshore and Coupling Zone regions on 7 February at the beginning of RF02. By 7 February, a strong surface current had developed which was dominantly southward. The raised thermocline and cool near-

surface temperatures along 16°N, from 40 km east of the gap exit to 20 km west, suggest coastal upwelling was already in progress (Figure 63a). By 8 February, upwelling continued to raise isotherms and bring cool water to the surface within a 40 km wide region east of the gap exit (Figure 63b).
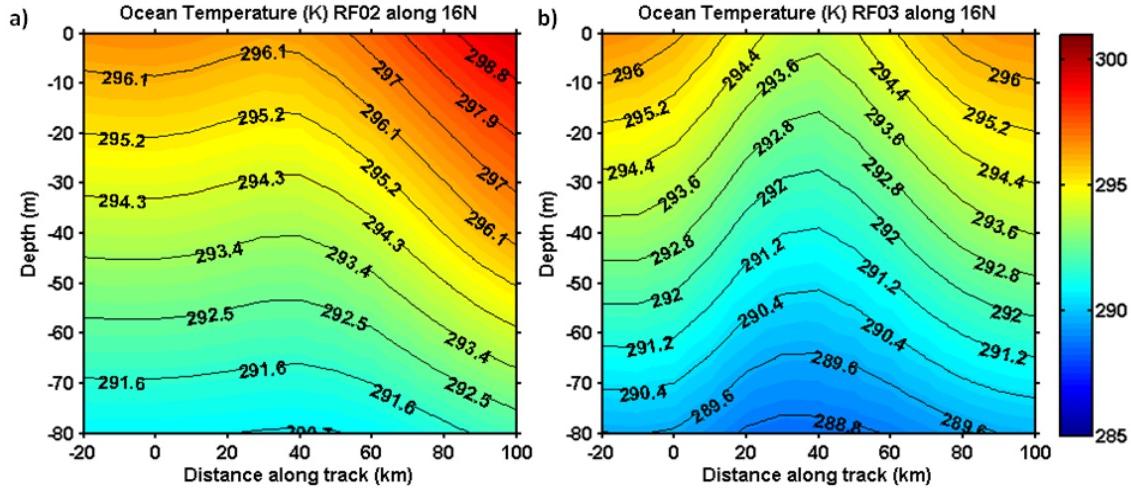
Figure 63. Vertical cross sections of NCOM ocean temperature (K) along 16°N at 1500 UTC on a) 7 February 2004 and b) 8 February 2004. The 0 km point on the horizontal axis identifies the axis of the gap exit.

Previous studies that discuss the disappearance or weakening of the cyclonic circulation to the east did not analyze simulated currents beneath the surface. Although westward surface currents dominated most of the GoT once Event II began, the cyclonic circulation to the east of the outflow jet remained strong beneath the surface. Figure 64 shows current speed and direction at 20 m depth for the same time as Figure 62d, 1500 UTC on 8 February 2004, during the decay stage of Event II. Below the surface, the cyclonic circulation was clearly identifiable in the 20 m currents. Although the eastward branch of the circulation was weak, the return flow to the north was relatively strong. The anticyclonic circulation was strong at 20 m depth, with current speeds exceeding 1 m s^{-1}.
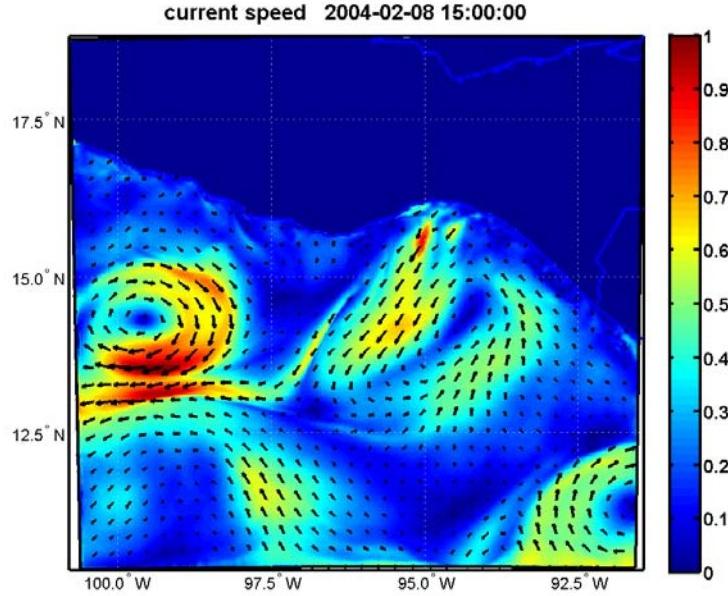
Figure 64.   NCOM current speed (m s^{-1}) and direction at 20 m depth at 1500 UTC on 8 February 2004.

As the outflow moved offshore, the surface currents developed in response to the surface wind stress. The surface current speed reached an offshore maximum along 14.5°N, while the longitudinal location of the maximum current moved westward along with the outflow jet. The current structure remained similar in depth and location but decreased in speed from 7 February to 8 February. The direction of the current shifted from southwestward to predominantly westward south of 14.5°N by 8 February, strengthening the southern branch of the anticyclonic eddy.

C.   EVENT V: 26–29 FEBRUARY 2004

1.   Simulated Evolution of the Atmospheric Boundary Layer

Northerly winds over the Gulf of Tehuantepec began at 0300 UTC on 26 February 2004. Within three hours, an outflow jet with low-level winds greater than 15 m s^{-1} was present along 95°W, extending beyond 15°N. Anticyclonic and cyclonic turning of the outflow winds were apparent on the west and east sides of the outflow, respectively. Similar to Event II, the flow on the east side of the jet appeared to merge with a secondary jet centered along 93.8°W. A wind speed minimum and converging

wind vectors that persisted throughout Event V suggest that these two low level jets remained separate and that the east side of the main jet (the Chivela Pass jet) was influenced by the presence of this secondary jet. Figure 65 shows the wind speed and direction at heights of 30 m, 365 m, and 660 m at 1500 UTC on 26 February 2004 (upper panels) and 27 February 2004 (lower panels), corresponding to the beginning of flights RF09 and RF10, respectively. By 1500 UTC on 26 February, the outflow jet exceeded 25 m s^{-1} at 365 m and above. The jet was elevated with strong shear-induced turbulence from the surface to the jet level. By 1500 UTC on 27 February, the jet had weakened slightly at 660 m, but the strongest winds were spread over a larger area at 365 m. The south and southwestward extent of the outflow has expanded between flights RF09 and RF10, in accordance with the expected progression of the leading edge of the outflow.
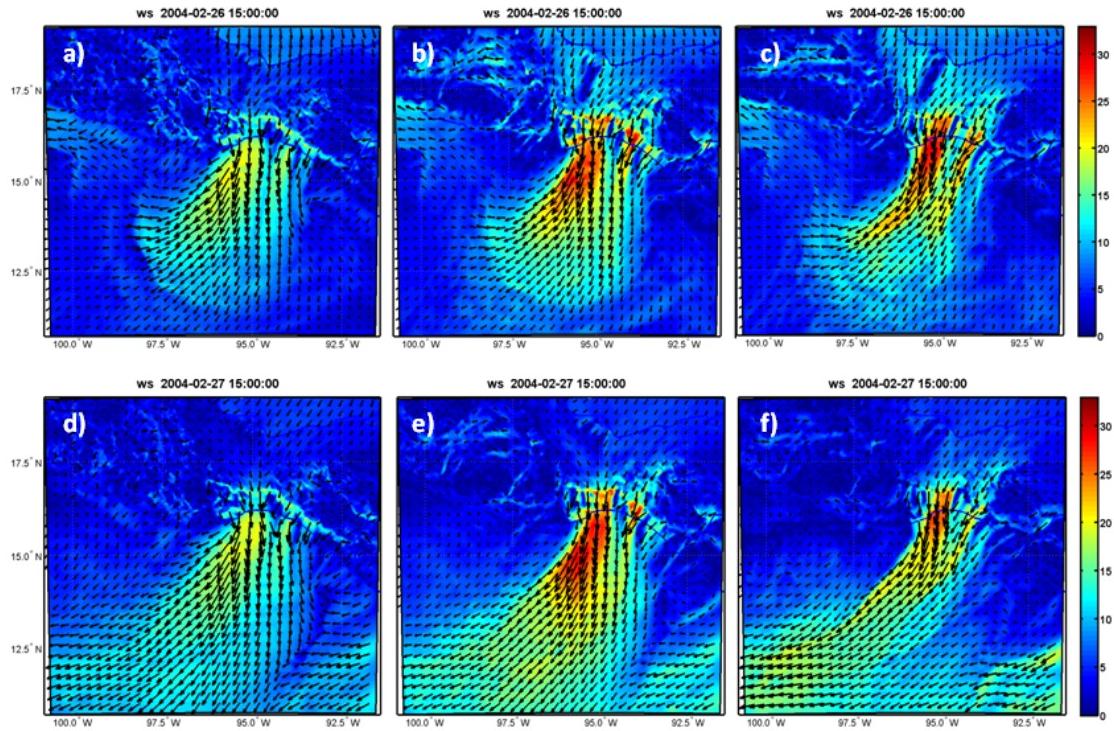

Figure 65.   COAMPS wind speed (m s^{-1}) with wind vectors at 1500 UTC on 26 February 2004 at a) 30 m , b) 365 m , and c) 660 m and on 27 February 2004 at d) 30 m , e) 365 m , and f) 660 m.

East-west cross sections from 16°N to 13.5°N show the vertical structure of the lower 1400 m of the atmosphere across the outflow jet moving away from the coast

(Figures 66 and 67). Just offshore, along 16°N on 26 February 2004, there was an elevated jet at 700 m height, which was centered along the gap exit with a maximum wind speed of 26 m s^{-1} (Figure 66a). The maximum wind speed within the jet was approximately 6–8 m s^{-1} faster than near the surface, suggesting the strong vertical wind shear as a source of turbulence in the boundary layer. The boundary layer here is topped by the jet core with the coolest well-mixed boundary layer beneath the jet core (Figure 66b).
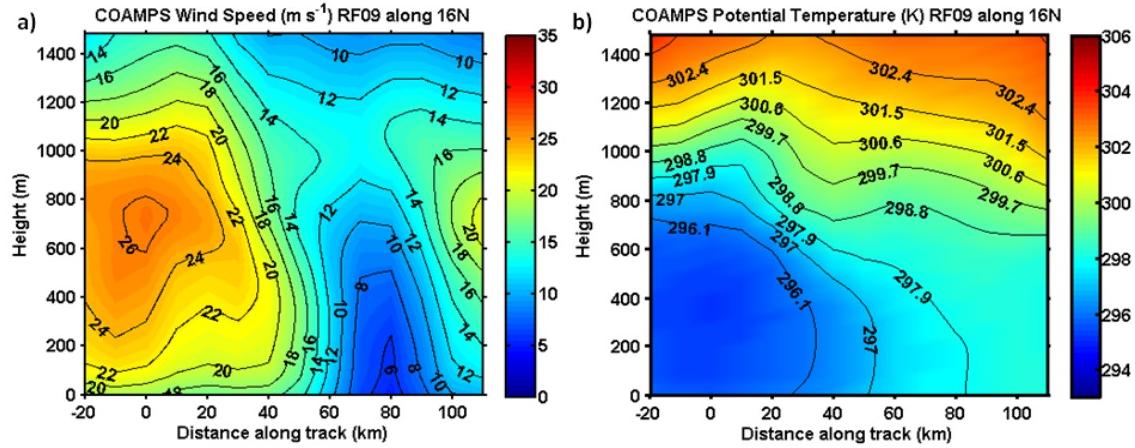
Figure 66.   Cross sections along 16°N of COAMPS a) wind speed (m s^{-1}) and b) potential temperature (K). The 0 km point on the horizontal axis identifies the axis of the gap exit.

Moving southward (Figure 67), the elevation of the jet core decreased in the Coupling Zone and returned to 600 m in the Offshore region. The strength of the jet core is similar between cross sections at 15.5°N and 14.5°N, but less spread out at 14.5°N compared to 15.5°N. The center of maximum winds also moved to the west away from the axis of the gap exit, while the negative *u*-component speed increased, consistent with anticyclonic turning south of 15.5°N. Turbulent kinetic energy (not shown) was high within the boundary layer and centered about 5 km west of the jet axis. Further to the south, the TKE maximum moved westward remaining beneath the outflow jet.
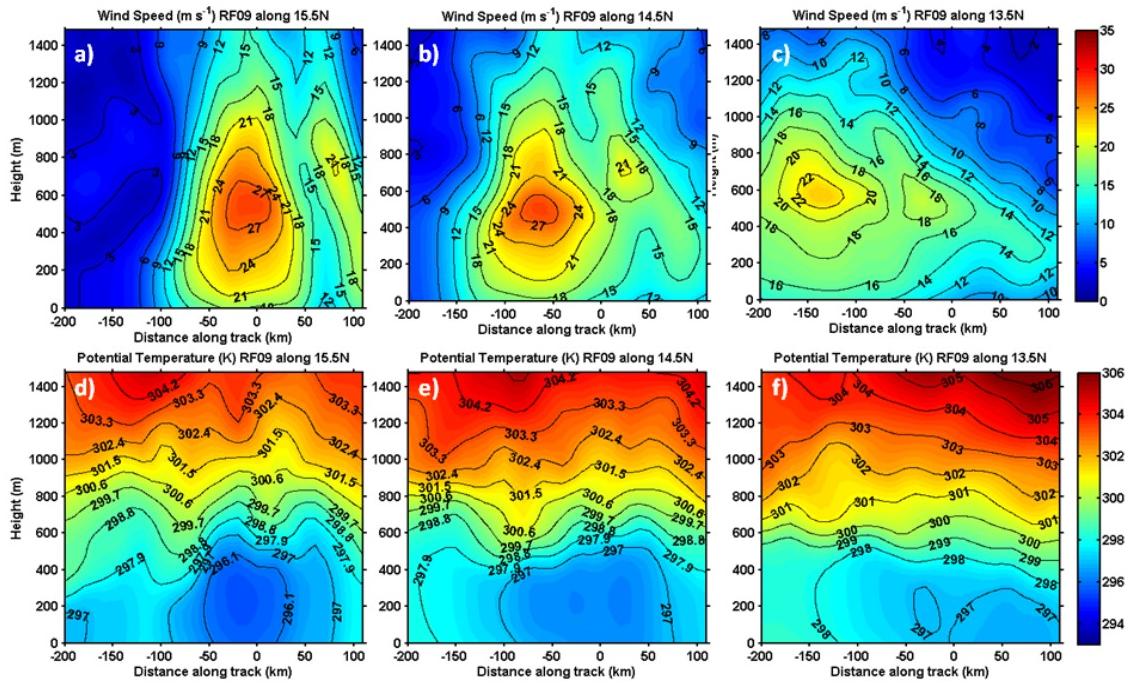
Figure 67.   Cross sections along 15.5°N (a, d), 14.5°N (b, e) and 13.5°N (c, f) of COAMPS wind speed (m s⁻¹, a-c) and potential temperature (K, d-f). The 0 km point on the horizontal axis identifies the axis of the gap exit.

Unlike the wind jet and TKE maximum, relatively cold air expanded westward, while the coldest air mass remained centered at the axis of the gap exit (Figure 66b and Figure 67, lower panels). Specific humidity (not shown) decreased throughout the GoT, with the driest conditions co-located with the outflow jet. The boundary layer air was approximately 6 g kg-1 drier than pre-event conditions.

Twenty-four hours later, the outflow jet maximum weakened by 2–3 m s-1 at each cross section location. The elevation of the jet maximum decreased by 200 m at 16°N, and approximately 100 m at each of the other three cross section locations (15.5°N, 14.5°N, 13.5°N). The depth of the cold air mass decreased slightly while the horizontal extent expanded, and the boundary layer potential temperature decreased by an additional degree throughout the entire outflow region. Specific humidity decreased throughout the outflow within and above the boundary layer. Overall, the behavior of the outflow jet and the evolution of the boundary layer properties agree well with the ABL evolution

seen in the GOTEX observations. Some of the direct inter-comparisons will be presented in Chapter VI as part of the model evaluation.

2. Simulated Evolution of the Ocean Mixed Layer

While AXBTs provide critical single-point measurements of the ocean thermal structure, NCOM simulations can provide much more detail in the evolution of the ocean mixed layer. Figure 68 shows the zonal (*u*-component) and meridional (*v*-component) ocean current, and ocean temperature along 16°N for 26 and 27 February 2004. This relatively shallow cross section is only 20 km south of the shore and spans the entire width of the GoT at this latitude. The surface current was negligible along 16°N on 25 February, the day prior to the onset of Event V (not shown). By the beginning of RF09, a strong surface current, greater than 0.25 m s^{-1}, flowed beneath the outflow jet from the surface down to approximately 50 m depth. The cross sections of the zonal and meridional current show a stronger westward component that agrees with the expected Ekman transport associated with a northerly wind jet (Figure 68a and b). By 27 February, 36 hours after onset, the SW current weakened by 50% from one day earlier (Figure 68d and e).
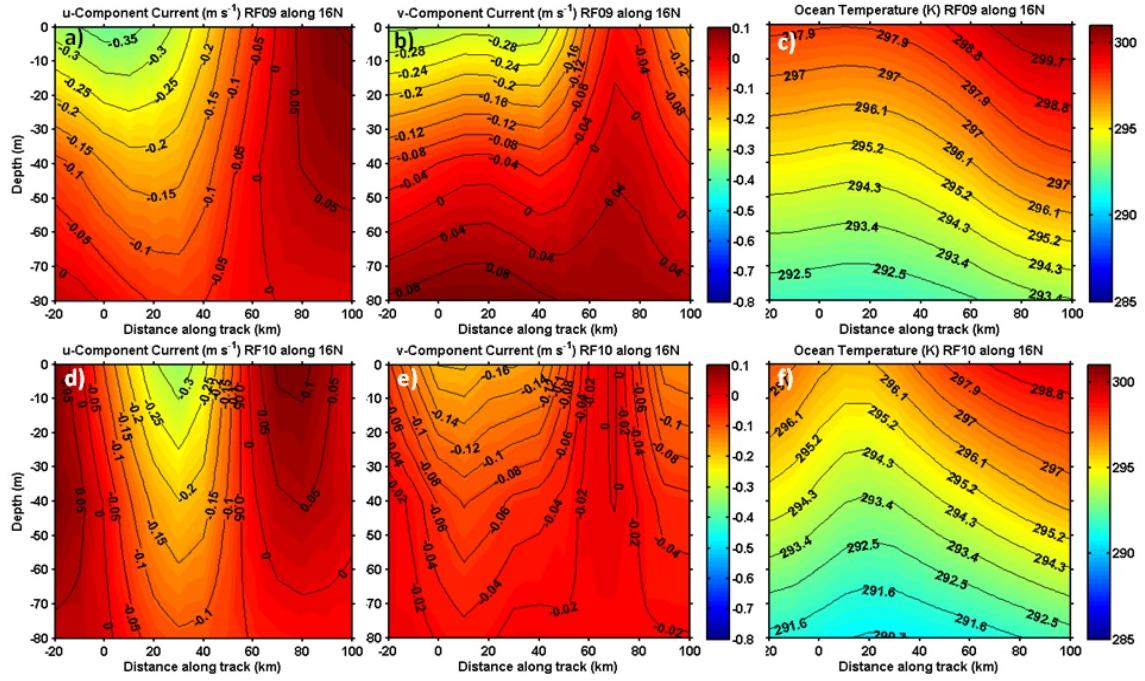
Figure 68.   Cross sections of *u*-component (a, d) and *v*-component (b, e) current speed (m s^{-1}) and ocean temperature (K, c, f) along 16°N on 26 February 2004 (a-c) and 27 February 2004 (d-f). The 0 km point on the horizontal axis identifies the axis of the gap exit.

Near-surface temperatures were slightly cooler on 26 February due to a raised thermocline within the area of the strong surface current (Figure 68a-c), which corresponds to the narrow region of cold sea-surface temperatures measured by the level aircraft legs (Figure 49). The upper-ocean was stratified except for a shallow, warm mixed layer to the east. Compared with 24 hours previous (not shown), the near-surface temperatures across the entire cross section have cooled, with the strongest cooling (1–1.5 K) centered along the axis of the gap exit. By 27 February, the near-surface temperatures along the axis cooled an additional 2 K (Figure 68f). Strong upwelling is evident by the raised isotherms centered approximately 15 km east of the gap exit. The region of coolest near-surface temperature and raised thermocline is narrower than on 26 February. To the east, the very shallow mixed layer was still present, but the temperature there also cooled by 1 K. The location of the SW current and cooling of near-surface

110

waters agrees well with aircraft measurements within the Nearshore region which showed continued cooling of sea-surface temperatures from RF09 to RF10 (Figure 49).

The gap outflow event triggered strong surface currents beneath the outflow jet, especially within the Nearshore region. Figure 69 shows surface currents at 1500 UTC from 25 February until 28 February. Aircraft measurements of cold sea-surface temperature with very strong gradients correspond to the location of the strong ocean current (Figure 49). However, the NCOM current fields prior to the onset of Event V suggest that three prominent features already existed within the GoT region (Figure 69a). An anticyclonic eddy was centered at 14°N, 97°W, with strong surface currents along the southern half of the eddy. A small, weak cyclonic eddy was centered at 14°N, 94°W. These two eddies are often discussed in studies of the GoT outflow because of the asymmetric response associated with them. More often, the anticyclonic eddy to the west is observed, while the cyclonic eddy to the east does not always form as a response to the outflow. Barton et al. (1993), for example, discussed the persistence and strengthening of the anticyclonic eddy from frequent outflow events. By 25 February, four outflow events had been measured within the GoT area which may have resulted in these persistent eddies. The third feature was another anticyclonic eddy located in the SW corner of the domain, and centered at 10.5°N, 93°W. Northwestward along-shore flow toward the head of the Gulf was present prior to onset of the northerly winds (Figure 69a). This convergent flow is noted in previous studies (McCreary et al. 1989; Trasviña et al. 1995) and will be important when discussing the heat budget in Section D.
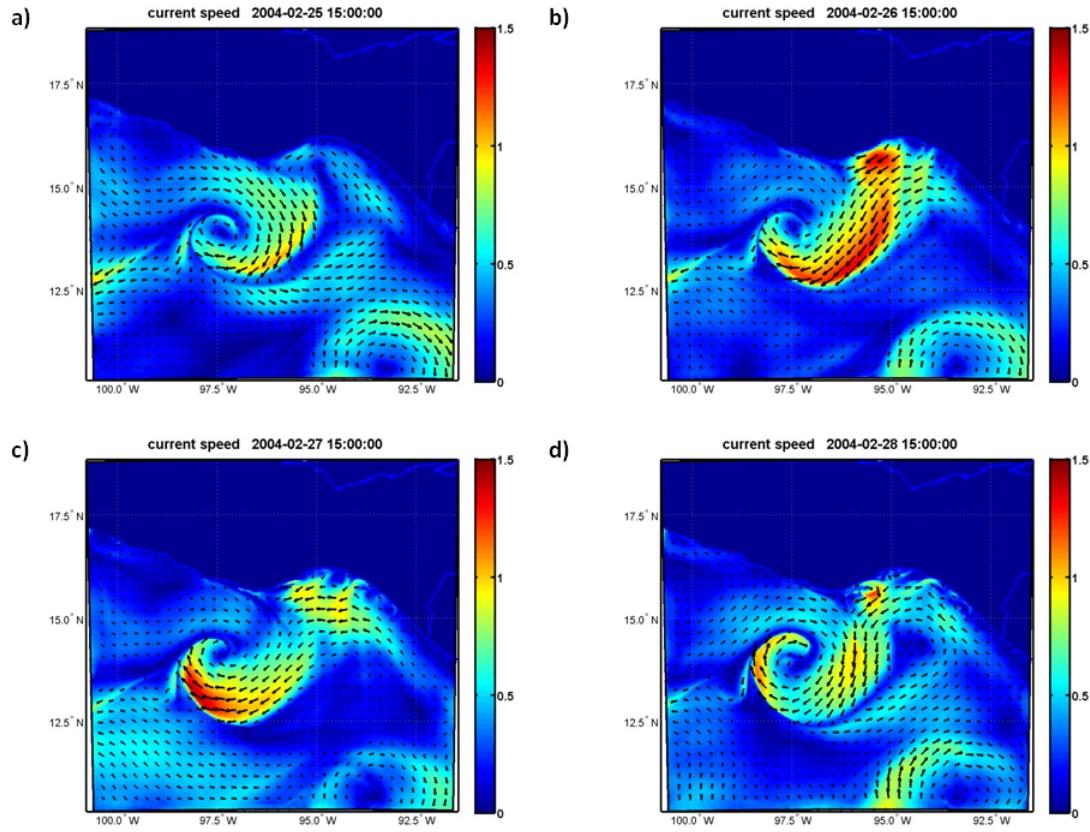
Figure 69.   NCOM surface current speed (m s^{-1}) at 1500 UTC on a) 25 February, b) 26 February, c) 27 February, and d) 28 February 2004. Black arrows represent current magnitude and direction.

As a result of the strong outflow jet formed during Event V, the general pattern of surface currents within the GoT before the event onset was greatly enhanced. Figure 69a, b, and c show the development of surface currents during Event V. Within twelve hours of onset, at the beginning of RF09, strong surface currents had formed within the Nearshore and Coupling Zone regions. Just beyond the Nearshore boundary, there are very strong southwestward surface currents, exceeding 1.2 m s^{-1} (Figure 69b). Further offshore, but still within the Coupling Zone, the strong currents are almost entirely southward. As Event V was decaying at the beginning of RF10 (Figure 69c), strong westward currents flowed across the Coupling Zone just shoreward of the shelf break clearly showing the Ekman response, 90° to the right of the strong wind forcing, while there was an area of weak currents centered at 15°N 95°W. The resurgence of the

southward current along the jet axis on 28 February (Figure 69d) suggests that there is some short-time scale temporal variability of the surface currents during the outflow event.

A vertical cross section along 14°N from 100°W to 92.25°W shows the presence of both circulations after the onset of Event V (Figure 70a). Regions of positive *v*-component current to the west (-300 km, 97.76°W) and east (+200 km, 93.13°W) show the northward branches of the anticyclonic and cyclonic eddies, respectively. The temperature cross section shows the strong upwelling induced by the outflow jet along the axis of the gap exit, while the depressed isotherms at -300 km suggest downwelling west of the outflow due to Ekman convergence. The wrapping of warm and cold filaments into the anticyclonic eddy as suggested by Barton et al. (1993) is evident in the variability in the OML within this cross section (Figure 70b), and the sea-surface temperature field (Figure 70c).
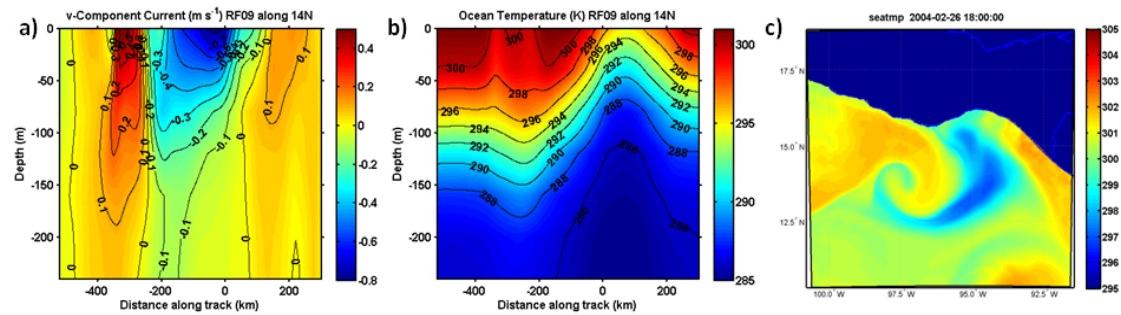
Figure 70. NCOM variables of a) *v*-component current speed (m s^{-1}, left), b) ocean temperature (K), and c) sea-surface temperature (K) at 1800 UTC on 26 February 2004.

D. HEAT BUDGET OF THE OCEAN MIXED LAYER

The heat budget of the ocean mixed layer was calculated to better understand the contributions to the significant cooling of sea-surface temperatures during outflow events. Figure 71 shows the mixed layer depth within the GOTEX domain at 1500 UTC on 07 February and 08 February 2004. The method of diagnosing the MLD from NCOM temperature and salinity is described in Chapter III. At the beginning of RF02 (1500 UTC on 07 February), the NCOM mixed layer depth had not changed significantly from

113

pre-event conditions (Figure 71a). A deep mixed layer was present within the anticyclonic eddy centered at 14.5°N 99.5°W and along 96°W nearly perpendicular to the coast. The rest of the GoT had a relatively shallow mixed layer that was 20–30 m deep. By 08 February, the persistent outflow wind led to deepening of the mixed layer throughout the Gulf, although the general pattern remained unchanged (Figure 71b).
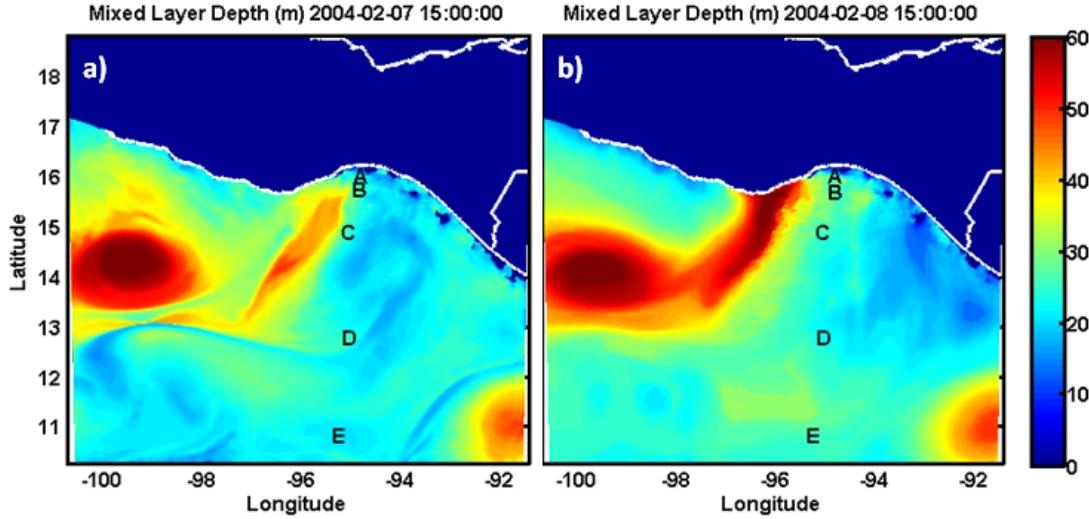
Figure 71.   Mixed layer depth (m) diagnosed from NCOM temperature and salinity at 15 UTC on a) 07 February 2004 and b) 08 February 2004. The letters represent locations for NCOM profiles in Figure 72.

The letters in Figure 71 correspond to the locations of NCOM profiles of temperature, salinity, potential density and u and v current components (Figure 72). Each location is represented by a different color. The solid profiles correspond to 07 February and the dashed profiles correspond to 08 February. All of these profiles show the persistence of an OML of at least 20 m throughout Event II. The coldest OML temperature was within the Coupling Zone at location C on 08 February. The Nearshore and Coupling Zone profiles (A, B, and C) all show OML cooling from 07 to 08 February. The difference between the temperatures profiles below the thermocline on the two successive days at locations A, B, and C also indicate upwelling. Locations D and E were within the offshore region and east of the outflow jet. These locations show warmer temperatures and very little change during this two day period. All five locations show a slight increase in salinity within the mixed layer, especially at location C in the Coupling

Zone, consistent with strong entrainment of salty water from below the mixed layer as well as evaporation of water at the surface. The potential density profiles show slightly higher density within the mixed layer corresponding to cooler, saltier surface waters. The profiles of the u and v current components show large variability in the surface currents, although the magnitude at each location remains fairly constant through the mixed layer, dropping off rapidly at the thermocline depth.
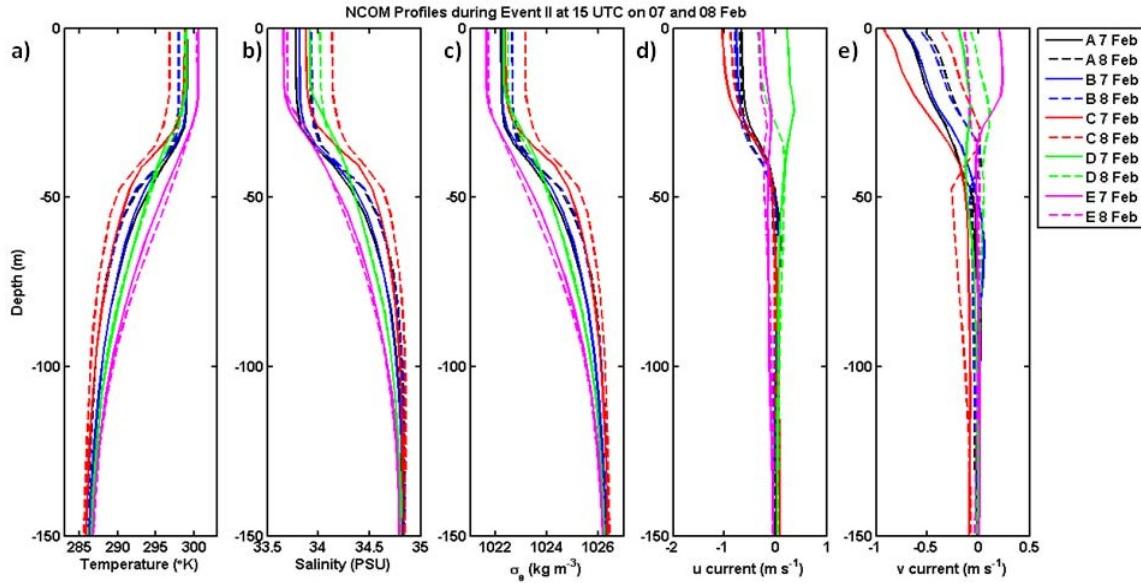
Figure 72. Vertical profiles of NCOM a) temperature (K), b) salinity (PSU), c) potential density (kg m^{-3}), d) u component current (m s^{-1}), and e) v component current (m s^{-1}) at the five locations labeled in Figure 71. Solid profiles are from 1500 UTC on 07 February 2004. Dashed profiles are from 1500 UTC on 08 February 2004.

The terms of the heat budget were calculated over the GOTEX domain. Figure 73 shows the spatial distribution of the terms of the heat budget equation (Eq. 11) at 1500 UTC on 08 February 2004. The area along the gap outflow shows the most significant cooling with a maximum cooling rate of -0.2 °C hr^{-1} closest to the coast. The horizontal advection (top, middle) shows a warming effect between the anticyclonic eddy and the offshore current beneath the outflow jet. This warming is attributed to converging coastal currents that bring warm surface water toward the mouth of the Gulf, which are then entrained into the offshore flow and wrap into the anticyclonic eddy. From Figure 73, it

is clear that the major contribution to cooling within the mixed layer is within the residual term, which is mostly attributed to entrainment mixing at the bottom of the mixed layer. The residual term remains strongly negative along the radius of jet turning and the westward branch of the anticyclonic eddy where current speed remains strong and turbulent mixing within the OML is enhanced.
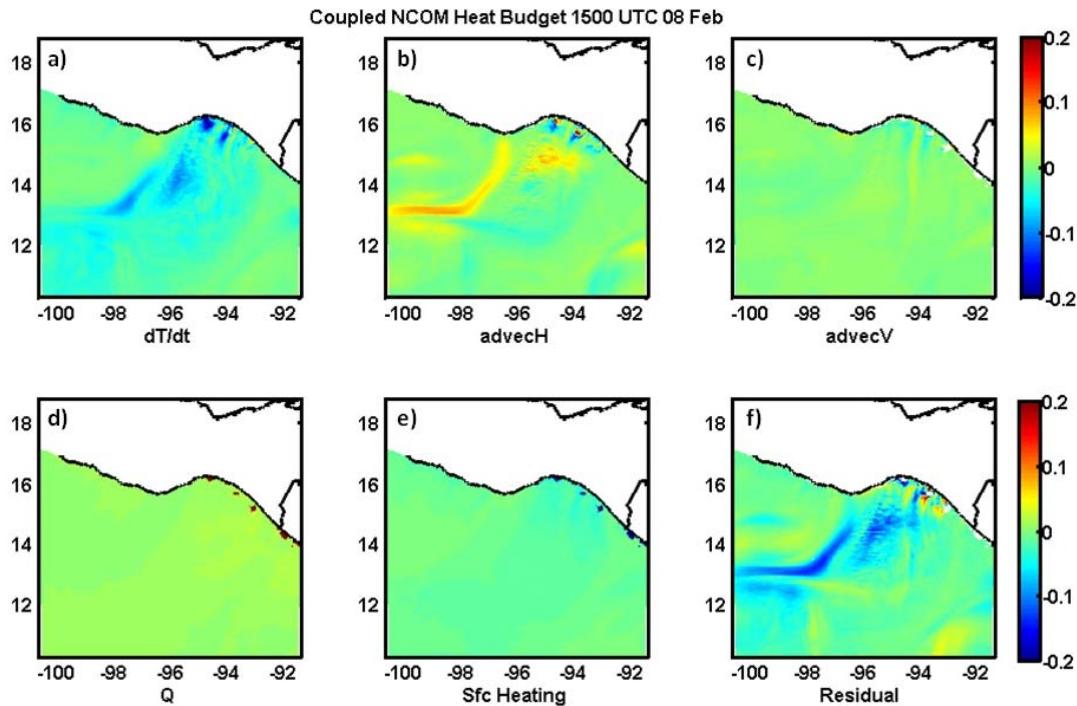
Figure 73.   Heat budget terms (°C hr^{-1})calculated from NCOM of the a) heating rate, b) horizontal advection, c) vertical advection, d) solar flux heating, e) surface heating due to sensible, latent and longwave heat fluxes, and f) the residual heating at 1500 UTC on 8 February 2004.

The temporal evolution of the OML heat budget terms from Event II are shown in Figure 74 from 1200 UTC on 6 February to 0300 UTC on 10 February for each of the four regions previously described (NS1, NS2, CZ and OFF). This figure show the average heating rate of the respective terms over the entire region; along the lines of NS1 and NS2, or over the boxed area of CS and OFF (Figure 55). The start, peak and end time of this event are also denoted in this figure by the vertical lines. The solid black lines note the start and end times, while the dashed line notes the peak wind stress during the event. The sign and magnitude of each term are clear in Figure 74. Figure 75 shows

116

the corresponding air-sea temperature difference, latent heat flux, sensible heat flux, solar flux, and wind stress for the same period.
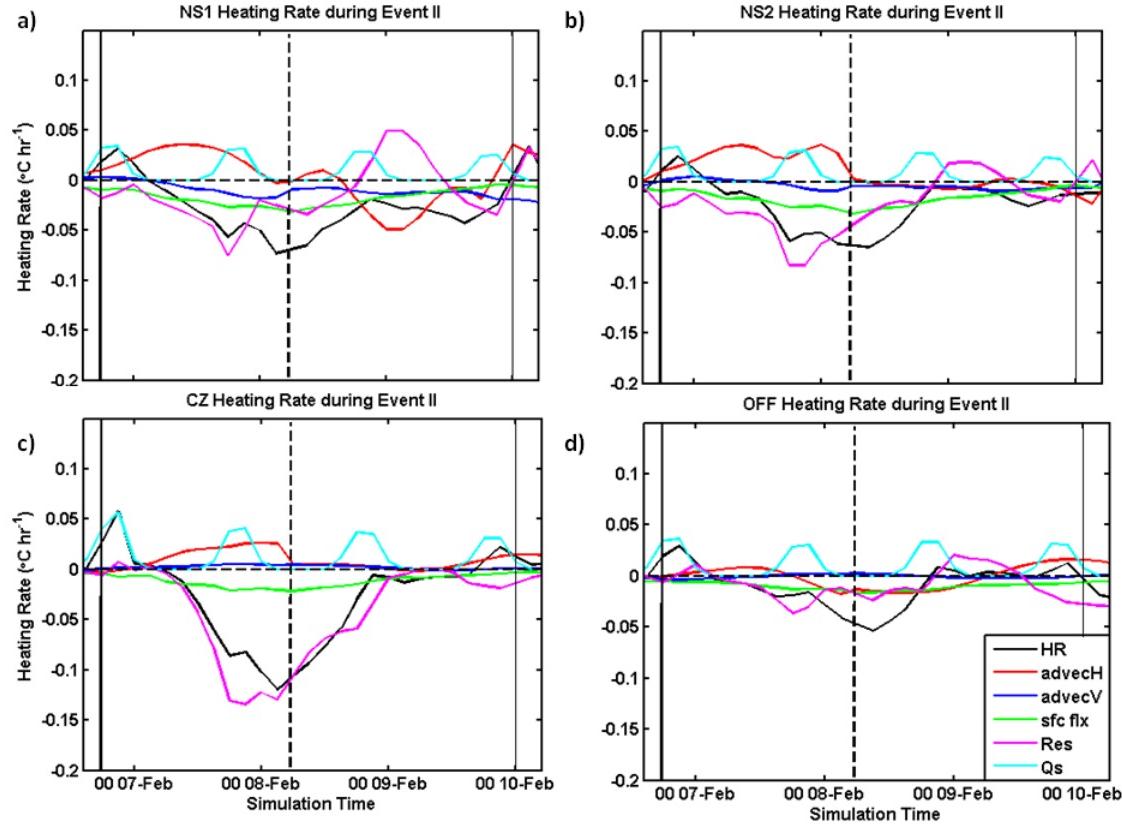
Figure 74.   Time variation of heating rate (black), horizontal advection (red), vertical advection (blue), surface flux heating (green), residual heating (pink) and solar radiation heating (cyan) in °C hr^{-1} for a) NS1, b) NS2, c) CZ, and d) OFF from 12 UTC on 06 February to 03 UTC on 10 February 2004.

117
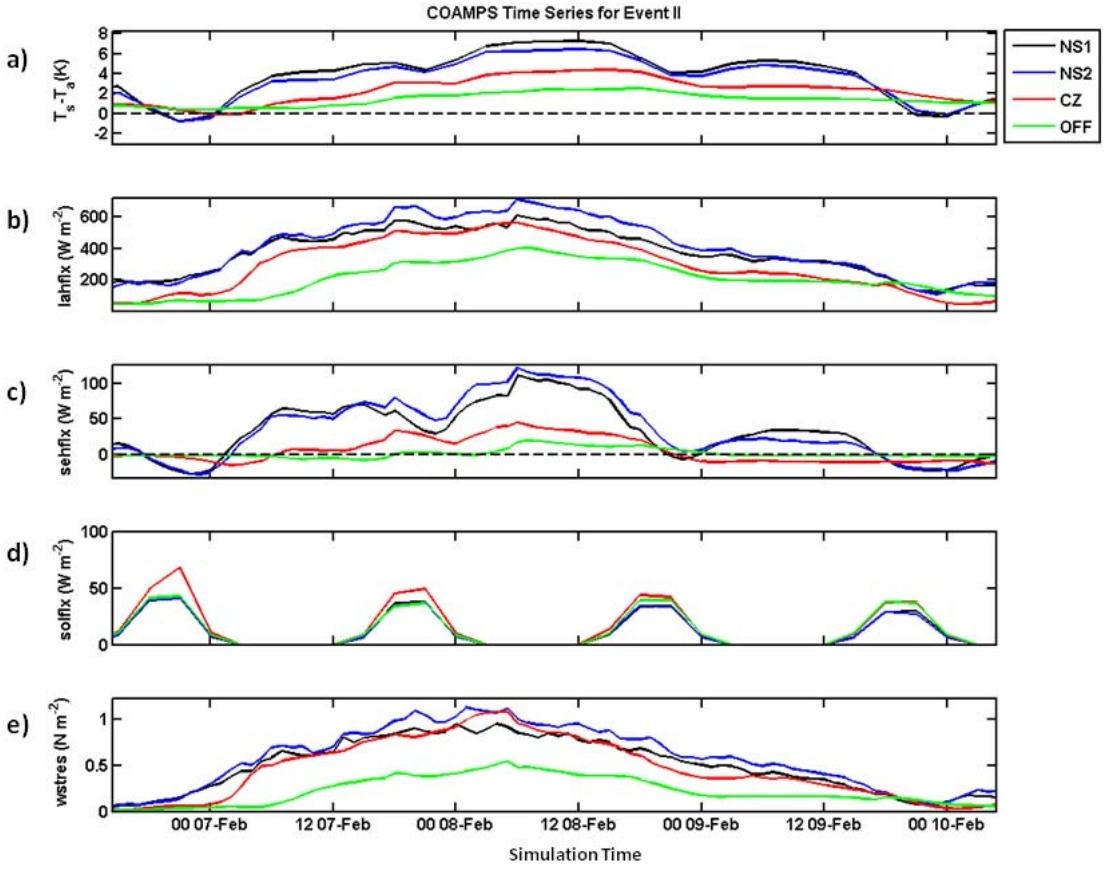
Figure 75.   COAMPS/NCOM a) air-sea temperature difference (T_s-T_a, K), b) latent heat flux (W m^{-2}), c) sensible heat flux (W m^{-2}), d) solar heat flux (W m^{-2}), and e) wind stress (N m^{-2}) for NS1 (black), NS2 (blue), CZ (red), and OFF (green) regions from 12 UTC on 06 February to 03 UTC on 10 February 2004.

Before discussing the results, we should look into the sources of error in the calculation of the heat budget terms. A quick inspection of the results in Figure 74 reveals a time period around 00 UTC 9 February when the residual term became positive. There are other time period in Event II (as well as Event V, to be shown later) with positive residual terms as well, mostly in the Nearshore and Coupling Zone regions. This is not physically plausible, considering the residual term is the entrainment cooling as seen in Equation 20. However, here, the residual term is in fact the sum of cooling from entrainment and any errors in the budget calculation. The budget terms shown in Figure 74 are vertically averaged in the mixed layer and were also horizontally averaged over the lines of NS2 and NS2, or the areas of the CZ and OFF. The averaging process may

118

introduce differences from the model physics that were applied to each grip point. This is especially true in the case of strong variability such as in the Nearshore and Coupling Zone regions and/or when the budget terms are small. Such differences should show up in our budget analyses as 'error' in the residual term. Error may also result when there is large variability in the MLD as the terms are vertically averaged as well. This type of error is most likely to happen to the nonlinear advection term. It also shows up more apparently during the later part of the temporal evolution shown in Figure 74, after the gap outflow event begins to weaken and when all the terms are relatively small. Hence, our discussion should be limited to periods of intensive cooling to avoid relatively large errors, which is during the early part of the outflow events.

A few significant features of the heat budget terms are worth mentioning. First, the significant cooling of the OML is clear in all regions during the development stage of the gap event. For this event, daytime warming of the upper-ocean, which is still dominant at the beginning of the event. However, from the onset of the event, entrainment cooling and cooling from surface fluxes (pink and green in Figure 74) are consistent with the enhanced turbulence in the mixed layer as a result of the large surface wind stress and loss of heat from the ocean surface to the atmosphere (Figure 75). The Nearshore locations (Figure 74a and b) show similar response within the OML. In the Nearshore and Coupling Zone regions, entrainment cooling became the dominant process once significant cooling began. However, the averaged heat budget terms of entrainment and surface flux cooling intensify toward the peak of the event and gradually decreased in magnitude of the cooling rate (weaker, but still cooling) toward the end of the event in all regions. Cooling continued beyond the peak of the wind stress through the end of the event at a slower cooling rate during the decay stage.

During the development stage of the gap outflow, horizontal advection served to warm up the OML in the Nearshore (Figure 74a and b) and the Coupling Zone (Figure 74c). This pattern continued until the peak of the event near 00 UTC on 8 February, after which this term became variable and relatively small. The upwelling term (advecV) is very small in the Coupling Zone and Offshore regions, but consistently cooling in the coastal waters of NS1. The upwelling velocity in NS1 and NS2 are considerable larger

119

than the other two regions (not shown), which is associated with the ageostrophic flow away from the coast at the mouth of the Gulf. This upwelling, together with the small vertical gradient of mixed layer temperature, resulted in sizable cooling only near the coast.

Within the Offshore region, the cooling rate is less than half of the cooling rate within the Coupling Zone. The cooling in this region is entirely due to the combination of heat loss at the surface and entrainment mixing, while the horizontal and vertical advection terms are negligible. After the gap event, the CZ and OFF regions clearly show warming in concert with solar heating while all other terms are relatively small.

Event V resembles Event II in many ways, but shows some significant differences as well. By the beginning of Event V on 26 February, the pattern of the mixed layer depth changed significantly within the GoT (Figure 76) compared to those in Event II (Figure 71). Now, shallower MLDs persisted throughout much of the central GoT, but the MLD within the anticyclonic eddy showed increased variability. Although the wrapping of cold and warm water into the eddy does lead to differences in density and therefore the mixed layer, it is likely that the pattern shown in Figure 76 is greatly enhanced.
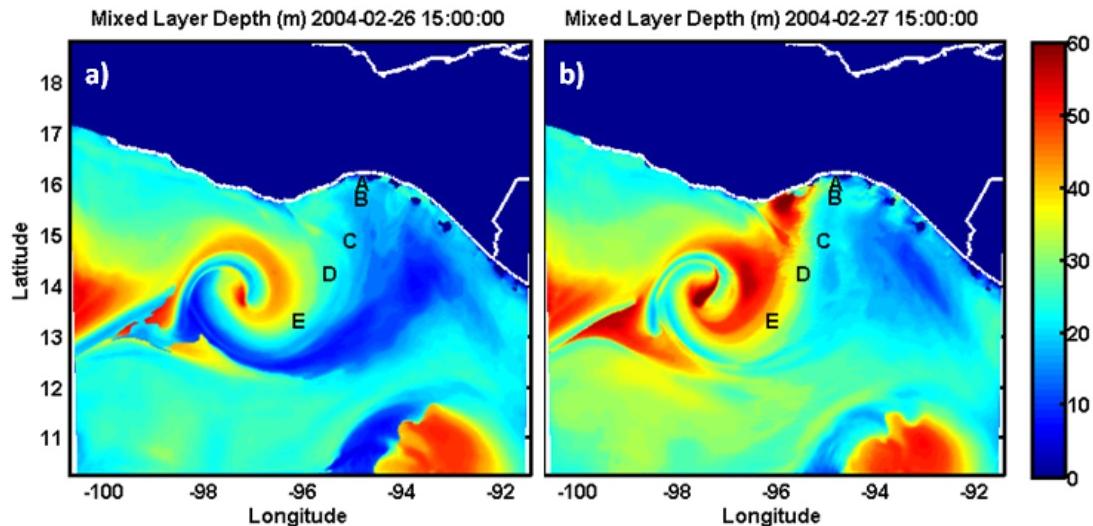
Figure 76.   Mixed layer depth (m) diagnosed from NCOM temperature and salinity at 15 UTC on a) 26 February 2004 and b) 27 February 2004. The letters represent locations for NCOM profiles in Figure 77.

Profiles from five locations within the outflow jet, labeled in Figure 76 indicated more coherent structure as a result of mesoscale dynamic organization. Profiles from five locations within the outflow, labeled in Figure 76, are shown in Figure 77. It is seen that the anticyclonic eddy has moved eastward, with the center located at 97°W. Along the outflow axis and east of the Gulf, the MLDs are shallow at 10–20 m. The shallow MLDs within the anticyclonic eddy are likely from the advection of water within the outflow current wrapping around the eddy. Figure 77 shows that the coldest and saltiest water was within the Coupling Zone (C). Both the thermocline and pycnocline within the Nearshore and Coupling Zone (A-C) are raised due to upwelling of cold, higher-saline water. Throughout the domain, the mixed layer deepens as a result of the outflow forcing by 27 February.
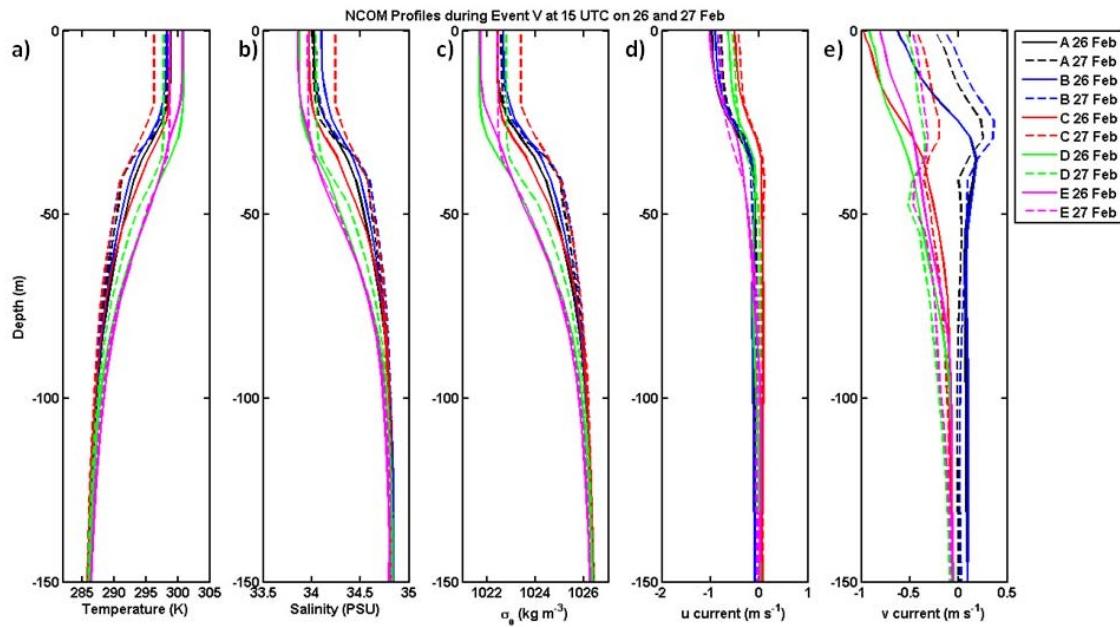
Figure 77. Vertical profiles of NCOM a) temperature (K), b) salinity (PSU), c) potential density (kg m^{-3}), d) u component current (m s^{-1}), and e) v component current (m s^{-1}) at the five locations labeled in Figure 76. Solid profiles are from 1500 UTC on 26 February 2004. Dashed profiles are from 1500 UTC on 27 February 2004.

The spatial distribution of OML heat budget terms at 1500 UTC on 26 February 2004 for Event V is given in Figure 78. The cooling rate at this time was strong throughout the central Gulf along the axis of the gap exit from the coast down to

121

approximately 13°N. Horizontal advection contributed to warming along the shelf break and cooling within the offshore current beneath the outflow jet. This term has the largest spatial variability and may become rather substantial at various locations.   Vertical advection remained weak. There was some slight solar warming to the east of the jet axis where MLDs were shallow. The surface flux heating rate was slightly negative, but the dominant contributor to the cooling was the residual, or entrainment cooling (Figure 78f) at the base of the mixed layer, which very much resembles the total cooling rate (Figure 78a).
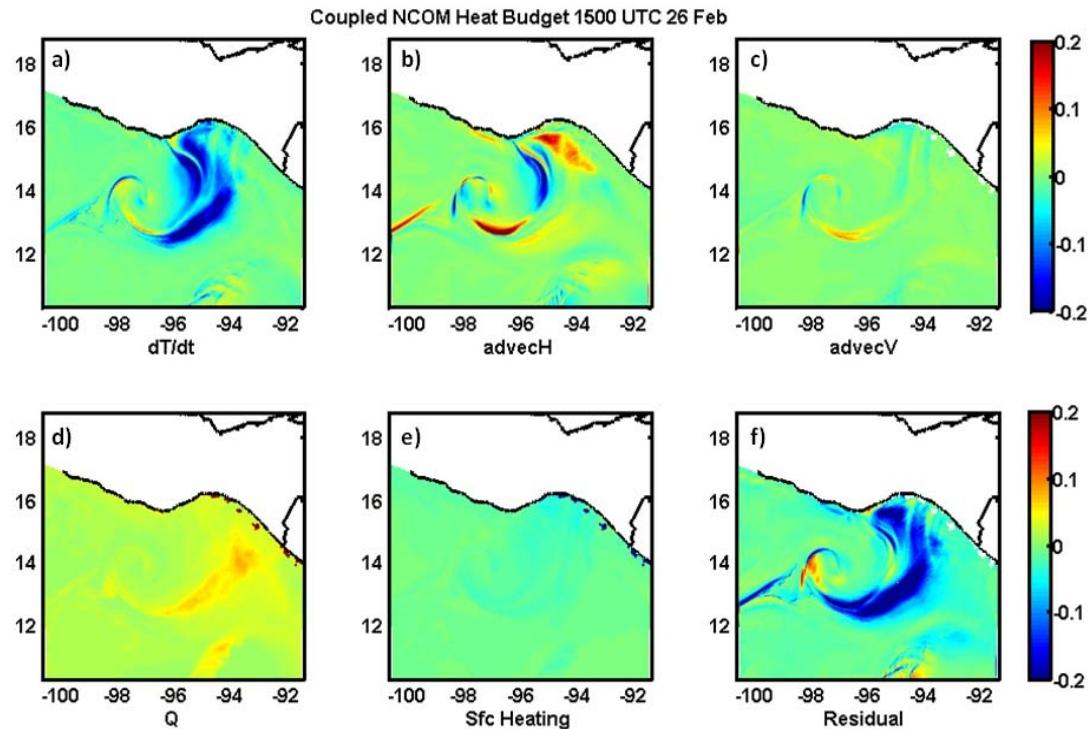
Figure 78.   Heat budget terms (°C hr^{-1})calculated from NCOM of the a) heating rate, b) horizontal advection, c) vertical advection, d) solar flux heating, e) surface heating due to sensible, latent and longwave heat fluxes, and f) the residual heating at 1500 UTC on 26 February 2004.

The Event V temporal variation of the heat budget terms and COAMPS/NCOM surface variables are shown in Figure 79 and Figure 80, respectively. Unlike Event II, cooling within the OML in the Nearshore and Coupling Zone regions began immediately. The strongest cooling rate was again within the Coupling Zone region. In the Nearshore

region (Figure 78a and b), horizontal advection warmed the surface layer by advecting warm surface water toward the mouth of the gap exit. Within the Coupling Zone, the horizontal advection contributed to the cooling of the OML. The role of horizontal advection is apparently more significant in Event V than in Event II. This event lasted much longer, nearly three days longer. The developing stage and the decaying stage of the event were very asymmetric with rapid development and an extended and slow decay stage through 21 UTC on 29 February.

The OML recovery process began as the outflow jet began to weaken. For all regions, the cooling rate approached zero by 06 UTC on 18 February. Within the Offshore region, the limited cooling within the OML recovered quickly, and showed a negligible heating/cooling rate after the event. NS1 and NS2 showed a quick recovery. Although the heating/cooling rate within the Coupling Zone region was close to zero after the end of Event V, the horizontal advection term remained negative. If the balance of the OML heat budget still holds, this cold horizontal advection could be the reason for the slow recovery of sea-surface temperatures within the Coupling Zone after Event V, as seen in the time evolution of COAMPS/NCOM sea-surface temperature in Figure 57b.
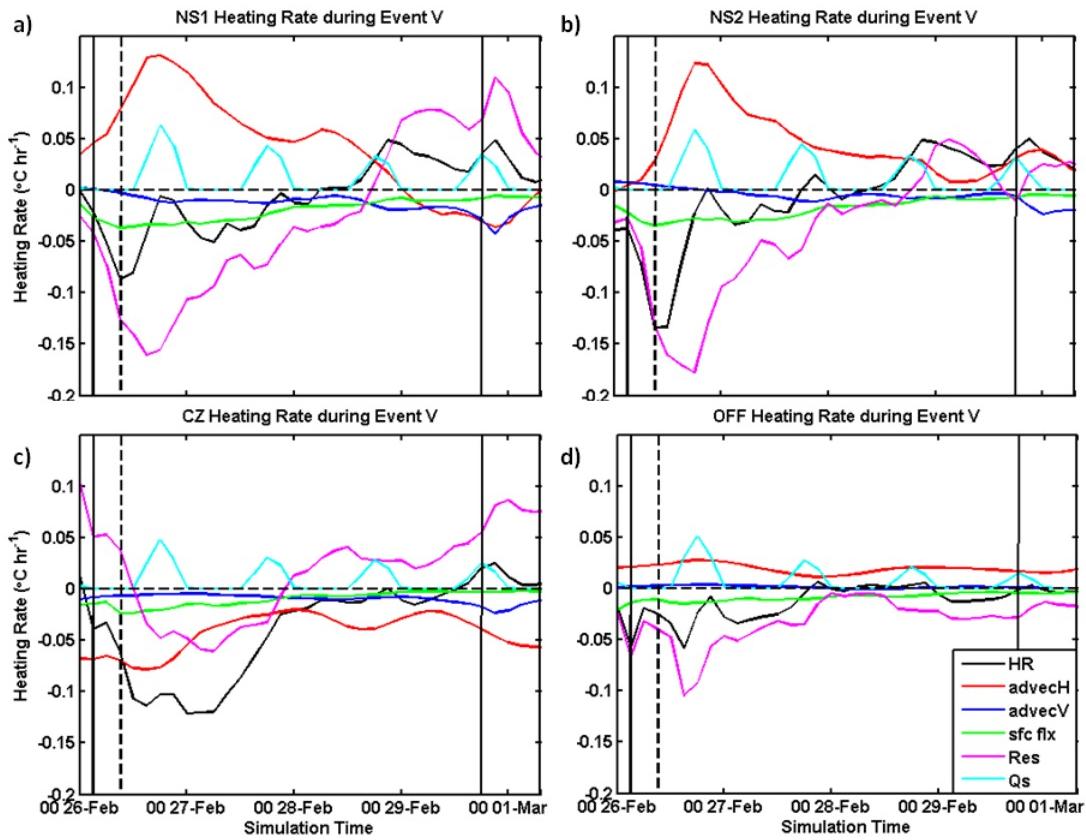
Figure 79. Time variation of heating rate (black), horizontal advection (red), vertical advection (blue), surface flux heating (green), residual heating (pink) and solar radiation heating (cyan) in °C hr^{-1} for a) NS1, b) NS2, c) CZ, and d) OFF from 00 UTC on 26 February to 03 UTC on 01 March 2004.

124
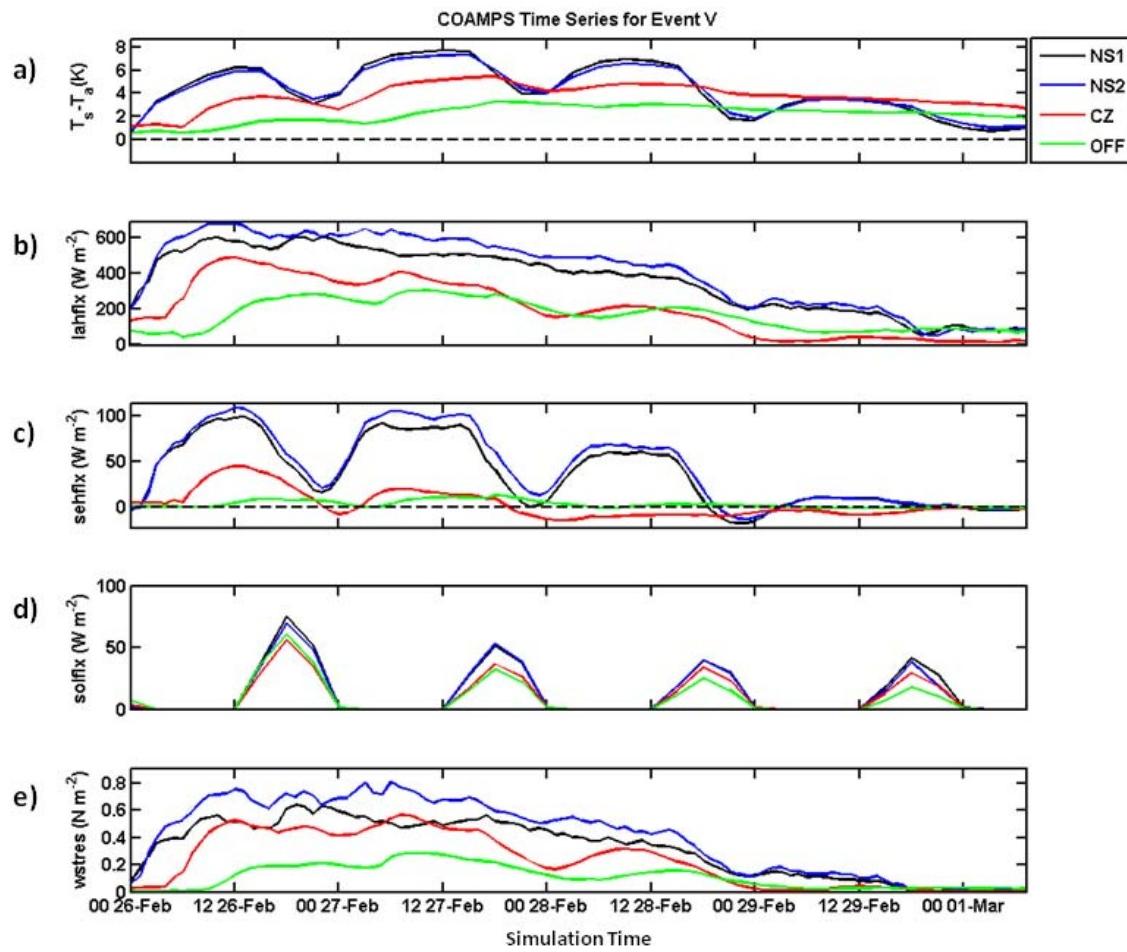
Figure 80.　　　COAMPS/NCOM a) air-sea temperature difference (T_s-T_a, K), b) latent heat flux (W m^{-2}), c) sensible heat flux (W m^{-2}), d) solar heat flux (W m^{-2}), and e) wind stress (N m^{-2}) for NS1 (black), NS2 (blue), CZ (red), and OFF (green) regions from 00 UTC on 26 February to 03 UTC on 01 March 2004.

THIS PAGE INTENTIONALLY LEFT BLANK

VI. EVALUATION OF UNCOUPLED AND COUPLED COAMPS/NCOM MODEL RESULTS

Fully coupled ocean-atmosphere models have been used for case studies of physical phenomena where air-sea interactions are expected to have a significant effect on the boundary-layer dynamics. Since evaluation and validation of fully-coupled models are still in progress, it is not clear where the ocean-atmosphere coupling will have the most significant impact. Previous modeling studies of the Gulf of Tehuantepec have used stand-alone atmosphere or ocean models only (Steenburgh et al. 1998; McCreary et al.1989; Clarke 1988). All of these studies have hypothesized that a fully-coupled model study of the gap outflow would be beneficial.

Observations from the GOTEX experiment provide the opportunity for model evaluation with measurements in the atmosphere, the upper-ocean, and particularly turbulence near the air-sea interface for quantifying the air-sea exchange processes. This chapter will focus on a systematic evaluation of the model results using GOTEX measurements. The model results to be evaluated include the stand-alone COAMPS, stand-alone NCOM (referred to as uncoupled) and the two-way coupled COAMPS/NCOM simulations.

The first part of our evaluation will include subjective evaluation of the structure of the downstream evolution of the gap outflow jet in the lower atmosphere along the path of dropsonde locations. Similar features in the upper-ocean temperature will also be studied along the path of AXBT locations for each of the four flights discussed in the previous two chapters. In the second part of the evaluation, we will make point-to-point comparisons between aircraft *in situ* observations and model output for an objective evaluation of the model error statistics. It is understood that such objective error analysis may not be optimal for high resolution models such as the COAMPS/NCOM setup used in this study because even a slight spatial or temporal shift may appear as model error, when in reality it may be an artifact of the interpolation from the model time and space to the time and location of the observation (Mass et al. 2002). However, these comparisons serve as a general overview of the model in comparison with the corresponding aircraft

observations. Such model evaluation efforts also allow us to examine the differences in the model results between the uncoupled and coupled COAMPS simulations, as well as the uncoupled and coupled NCOM output. Model error statistics were calculated using all aircraft observations made from legs at nearly constant altitude during nine GOTEX flights, which provide observations throughout the Gulf of Tehuantepec and varying stages of the outflow development. Since each of the five events varied greatly in maximum intensity and duration a wide range of boundary layer conditions are included in this evaluation.

A.   DOWNSTREAM DEVELOPMENT OF THE OUTFLOW JET

In this section, we will provide a subjective evaluation of the main features of the outflow jet development and its associated thermodynamic structure in the atmosphere. This section of the evaluation will mainly use dropsonde measurements from four flights where soundings were deployed with spatial coherence downstream of the jet core. Vertical cross sections along the path reveal the variation of the jet away from the coast, as seen from both observations and model simulations.

Figure 81 shows an example of the comparison of wind speed variability along the dropsonde path seen from RF10 dropsonde measurements and from the uncoupled and coupled COAMPS simulations. Here, agreement of the wind speed maximum is clearly seen along with the narrow, elevated structure of strongest winds reaching offshore. The elevation of the jet is higher in both the uncoupled and coupled COAMPS output and the simulated depth of the strongest winds is greater than measured by the dropsondes. In the uncoupled simulation, the strongest winds (greater than 20 m s^{-1}) do not reach far enough offshore, compared with the observations, while the coupled COAMPS wind jet reaches farther offshore than the observations. Comparisons from other GOTEX flights show similar results to those in Figure 81. In general, during each event, the modeled outflow jet was in reasonable agreement with aircraft observations. Comparison of the vertical cross sections from RF02, RF03, RF09, and RF10 show that both versions of COAMPS simulated a jet maximum that was higher in elevation with a

broader extent of strong winds, both vertically and in distance offshore, while the magnitude of the strongest winds agree well with dropsonde data.
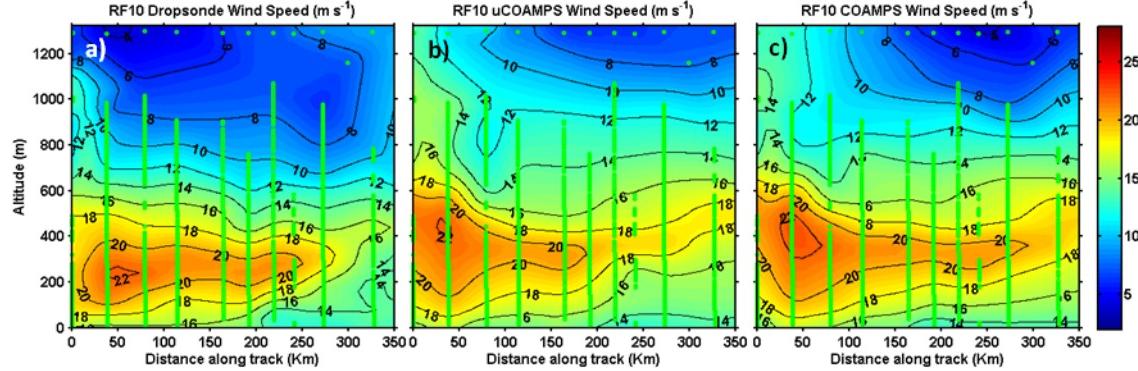
Figure 81.   Wind speed (m s^{-1}) cross sections along the RF10 flight track for a) dropsondes, b) uncoupled COAMPS, and c) coupled COAMPS/NCOM. Green vertical lines represent the locations where the dropsonde data were available. The horizontal axis shows the distance along the track in kilometers from the location of DS12, 4 km from shore, denoted by the blue star in Figure 41.

As the Central American cold surges trigger a strong pressure gradient across the Chivela Pass creating gap winds, the cold air flows through the gap and over the Gulf of Tehuantepec. We hence expect significant horizontal variability in the air temperature within the gap outflow region where the cold, dry air is advected over the water and modified by the coastal ocean. Figure 82 shows a comparison of potential temperature cross sections from dropsondes and coupled COAMPS for RF02 (Event II, a and b) and RF09 (Event V, c and d). The coupled and uncoupled COAMPS show very similar patterns in the temperature cross sections with differences between the two models of less than 0.5 K during all four flights. Due to this similarity, the temperature comparisons in Figure 82 show only the observed temperature and the coupled COAMPS output.
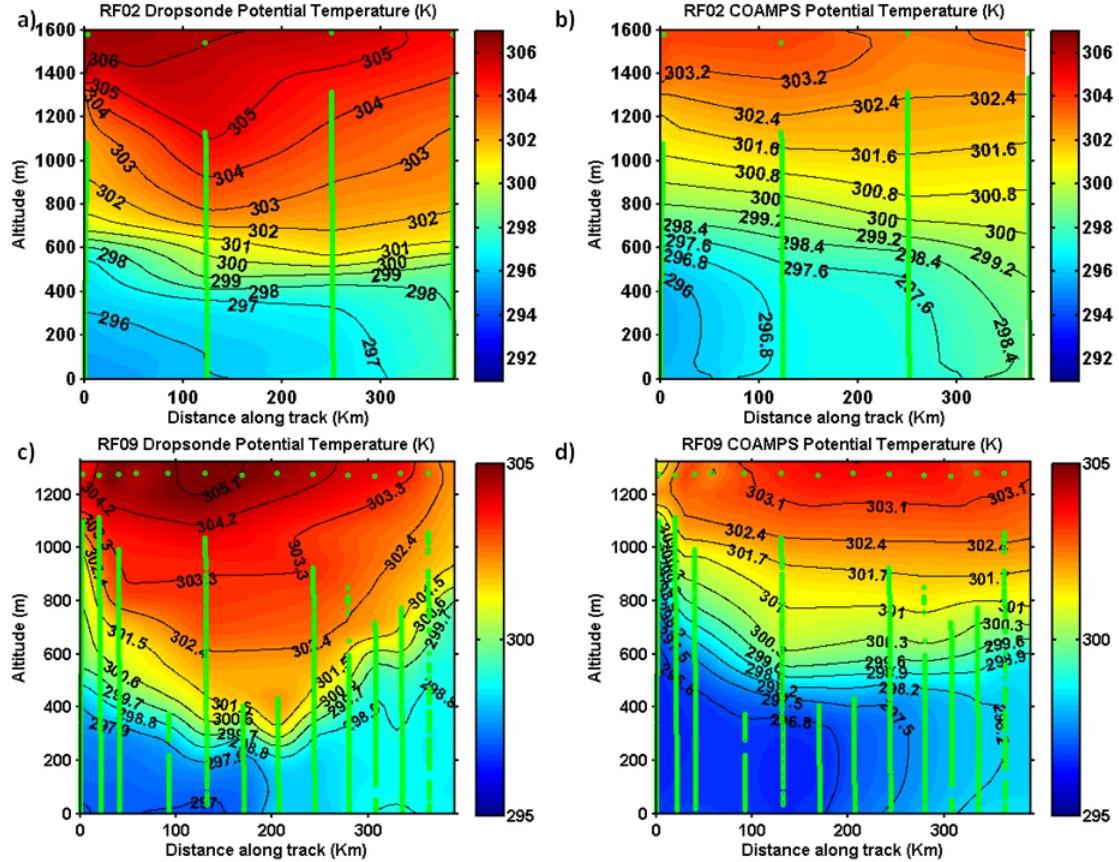
Figure 82.   Potential temperature (K) cross sections from dropsondes (a, c) and coupled COAMPS (b, d) for RF02 (a, b) and RF09 (c, d). Note the horizontal axis and temperature range are different for each flight. Green vertical lines represent the locations where the dropsonde data were available. The horizontal axis shows the distance along the track in kilometers. For RF02, the start point was the location of DS01, 119 km from shore, denoted with a blue star in Figure 11. For RF09, the start point was the location of DS14, 20 km from shore, denoted with a blue star in Figure 34.

Although the general temperature structure is similar between the observations and the coupled COAMPS simulation for both events shown in Figure 82, there are some notable differences. During Event II, the cold temperature in the model output at the beginning of the track does not extend as far offshore as seen in the dropsonde measurements (for example, the 296 K contour line in Figure 82b). The model boundary layer was consistently well-mixed through a deeper layer compared to the shallow mixed layer or layer with weak stable stratification in the first 200 km of the dropsonde cross sections (Figure 82 a and c). Such differences are likely caused by the larger surface

sensible and latent heat fluxes produced by the model due to over-estimated sea-surface temperature (which will be discussed in Section B). The depth of the well-mixed layer was too deep compared to observations during each of these four flights where dropsonde downstream tracks are available. During Event V (Figure 82c, d), the cold tongue of boundary layer air seems to extend much farther offshore compared to the dropsonde profiles. For this event, the observed mixed layer sloped down through the Coupling Zone to nearly 200 m altitude and then increased rapidly through the Offshore region (Figure 82c). This variability is not depicted in the corresponding model results (Figure 82d). Some of the details in the mesoscale features were not represented well in the model. However, the overall difference in temperature between the model and observations was less than 1 K within the boundary layer.

The offshore extent of the cold air was not far enough during Event II, but farther than observed during Event V, suggesting that inconsistencies in the model simulation are likely synoptically driven and due to larger scale differences not evaluated within this study.

Figure 83 shows a comparison of the vertical cross sections of specific humidity between the dropsonde measurements and the uncoupled and coupled COAMPS results from RF02. The general low-level moisture structure, as measured by dropsondes, was dry near the coast, with increasing moisture offshore. The driest air was close to shore above the boundary layer and the outflow jet. The overall pattern of specific humidity contours shows good agreement between the dropsondes and models. Note that the cross sections in Figure 83 began 119 km offshore, within the Coupling Zone. Both uncoupled and coupled COAMPs were slightly too moist Nearshore and within the Coupling Zone. Offshore, uncoupled COAMPS was too moist while coupled COAMPS was too dry. It is also noted that the boundary layers, observed and modeled, are strongly stratified in water vapor specific humidity, although a well-mixed boundary layer was identified in potential temperature. As seen in Chapter IV, the surface latent heat flux within the GOTEX region was extremely large due to the high wind stress and dry air advected through the gap. The persistent and extremely large latent heat flux during the Tehuano event may likely contribute to the water vapor stratification seen in Figure 83. This effect

is amplified in the model because the model over-estimated the surface latent heat flux
(to be discussed in Section B).
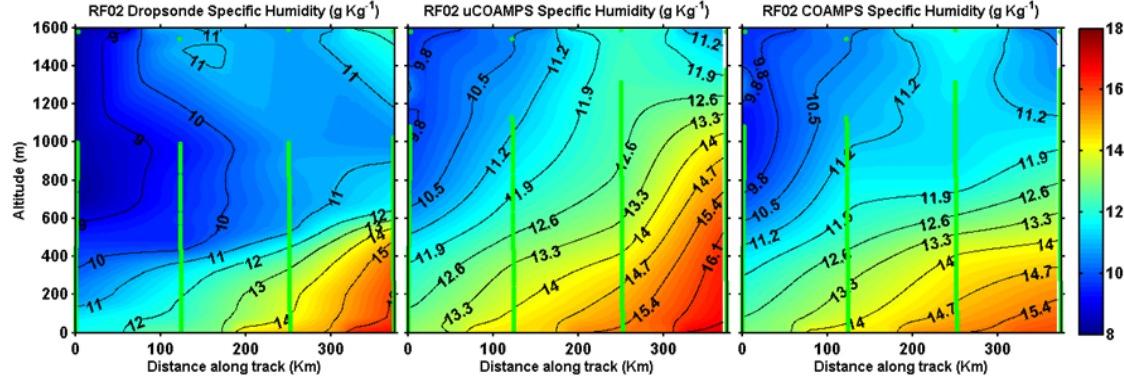
Figure 83.   Specific humidity (g kg^{-1}) cross sections from a) dropsondes, b) uncoupled
COAMPS, and c) coupled COAMPS. Green vertical lines represent the locations
where the dropsonde data were available. The horizontal axis shows the distance
along the track in kilometers. For RF02, the start point was the location of DS01,
119 km from shore, denoted with a blue star in Figure 11.

Vertical cross sections of sea temperature from AXBTs and coupled NCOM are
shown in Figure 84. Similar to the COAMPS potential temperature output, the sea
temperature from uncoupled and coupled NCOM vary by less than 0.5 K and therefore,
only the coupled NCOM sea temperature cross section is shown (Figure 84b). The RF02
vertical cross sections (Figure 84a and b) begin 20 km from shore. The very cold
Nearshore surface temperatures measured by the AXBTs were 4–5 K colder than the
Nearshore NCOM surface temperatures. The general structure of the raised thermocline
from 150 to 350 km along the track is well-represented by the NCOM sea temperature.
Within the Offshore region, the notable difference is the depth of the 286 K isotherm 50
m deeper than measured by AXBTs. The RF09 vertical cross sections begin 120 km
offshore within the Coupling Zone (Figure 84c and d). Here, the general temperature
structure throughout the cross section from coupled NCOM agrees very well with the
AXBT temperature structure. Nearshore, the difference in surface temperature is only
about 2 K warmer in coupled NCOM. Comparisons for flights RF03 and RF10 reveal
similar results.
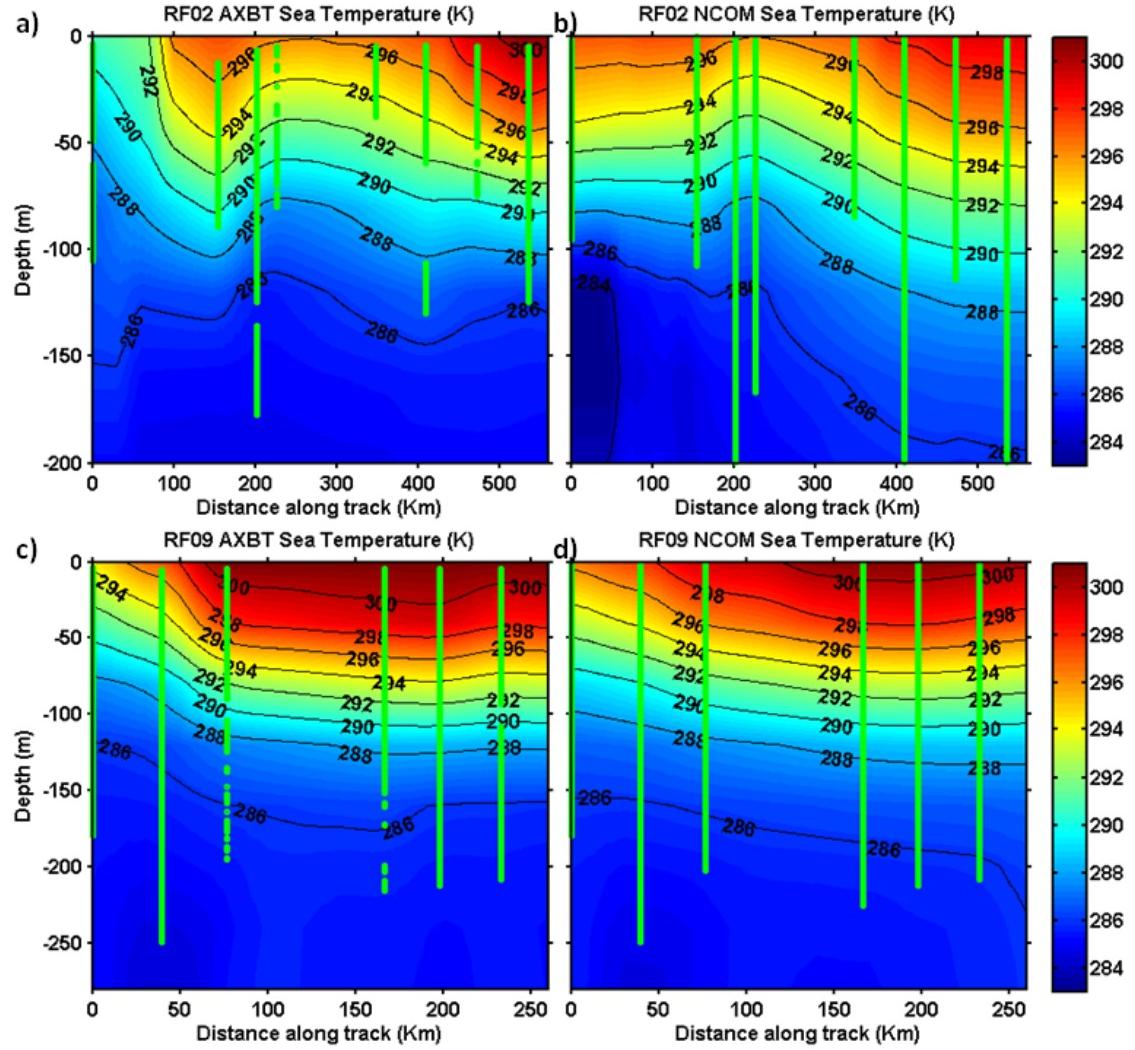
Figure 84. Sea temperature (K) cross sections from ABTS (a, c) and coupled NCOM (b, d) for RF02 (a, b) and RF09 (c, d). Note the horizontal and vertical axes are different for each flight. Green vertical lines represent the locations where the AXBT data were available. The horizontal axis shows the distance along the track in kilometers. For RF02, the start point was the location of BT01, 20 km from shore, denoted with a green star in Figure 11. For RF09, the start point was the location of BT14, 120 km from shore, denoted with a green star in Figure 34.

B. MODEL ERROR STATISTICS

This section provides a detailed inter-comparison of the model results to the aircraft observations. The evaluation is organized to first show the scatter plots of model vs. observational data to illustrate the variability of the measurements and the modeled values, as well as the difference between the two. These comparison pairs will be used to

133

generate model error statistics. We will also investigate the difference between the coupled and uncoupled model results.

A large number of data from the GOTEX C-130 measurements are available for the model evaluation. Since the measurements were made almost exclusively during active gap outflow events (with exception of RF08), all of the model-observation inter-comparisons are made during different stages of the outflow events. For surface variables (SST, T_s-T_a, sehflx, lahflx, wstres), the number of samples was 41,520. For sigma-level variables interpolated to aircraft altitude (theta, q_v, WS, TKE), the number of samples was 103,878. The high number of model-observations pairs is slightly misleading from the perspective of statistical significance. The model output may not be independent because of the inherent smoothing from the numerical schemes and the interpolation of neighboring grid points to the location of the observations. The result is a smaller effective sample size, which was not explicitly determined. Because of the difficulty in determining the degrees of freedom in this set of model-observation pairs, tests for statistical significance were not conducted. A normalized Taylor diagram will be used to consolidate several of the model error statistics (specifically the standard deviation, the correlation coefficient, and the centered RMS difference) so that improvements of the coupled model simulations over the uncoupled simulations can easily be identified.

A statistical summary of the analyzed variables is presented in Table 4. For a quick comparison of the coupled model performance versus the uncoupled model performance, the better values have been highlighted in red. For root mean squared error (RMSE), the lower value is considered to be better, and better bias values are based on the lowest absolute value. In general, the fully coupled COAMPS appears to have outperformed the uncoupled COAMPS, with an improvement in RMSE and correlation coefficient for the sea-surface temperature, air-sea temperature difference, sensible heat flux, specific humidity, latent heat flux, and turbulent kinetic energy.

Two variables stand out from this generalization. The RMSE and bias increased slightly for coupled COAMPS potential temperature. However, the variability increased, as inferred from the higher standard deviation for the coupled model. The lower centered

RMSE ($RMSE_C$) for the coupled model suggests that the perturbations of potential temperature were more accurate. For the wind speed, the coupled model had a higher standard deviation and error (RMSE and $RMSE_C$), and the bias shows only a slight improvement. With a mean difference of only 0.02 N m^{-2} and hundredths of a difference between the other statistics, there was essentially no difference in wind stress between the models. The comparison between uncoupled and coupled NCOM is limited because only wind stress and sea-surface temperature are available for comparison. However, the coupled NCOM does show improvement in sea-surface temperature over the uncoupled NCOM, while the change in wind stress is minimal, just as in COAMPS.

Table 4.   Statistics of mean, standard deviation (σ), root mean square error (RMSE), bias, centered RMSE ($RMSE_C$), and correlation coefficient (R) for uncoupled (uCO) and coupled (cCO) COAMPS vs. aircraft observations (a/c). Lower values of RMSE, bias, and $RMSE_C$, and higher values of R are highlighted in red to draw attention to the difference between the models. The two NCOM variables are denoted with 'N' before the variable name.

Variable	Mean			σ			RMSE		Bias		RMSE$_c$		R	
	a/c	uCO	cCO	a/c	uCO	cCO	uCO	cCO	uCO	cCO	uCO	cCO	uCO	cCO
THETA K	299.00	298.16	297.98	3.98	3.93	4.02	1.56	1.62	-0.84	-1.02	1.32	1.26	0.94	0.95
SST K	298.05	299.67	298.56	3.02	1.47	1.68	2.66	1.88	1.62	0.52	2.11	1.81	0.77	0.85
NSST K	298.05	298.22	298.56	3.02	1.73	1.69	1.99	1.88	0.17	0.50	1.99	1.81	0.78	0.85
Ts-Ta K	1.27	3.36	2.57	1.80	1.41	1.23	3.01	2.24	2.10	1.31	2.15	1.82	0.12	0.33
SEHFLX W m^{-2}	6.88	47.79	29.99	26.17	33.69	27.82	56.68	38.11	40.91	23.11	39.23	30.31	0.16	0.37
q$_v$ g kg^{-1}	11.33	11.34	11.05	2.74	2.61	2.56	1.46	1.34	0.01	-0.28	1.46	1.31	0.85	0.88
LAHFLX W m^{-2}	340.06	505.55	432.01	185.04	154.19	143.04	221.01	164.19	165.49	91.95	146.48	136.03	0.64	0.68
WS m s^{-1}	13.63	16.40	16.42	3.28	5.68	5.88	6.91	7.08	2.79	2.77	6.33	6.51	0.08	0.08
WSTRES N m^{-2}	0.48	0.50	0.48	0.33	0.22	0.22	0.22	0.22	0.02	0.00	0.22	0.22	0.74	0.74
NWSTRES N m^{-2}	0.48	0.51	0.48	0.33	0.23	0.22	0.22	0.22	0.03	0.00	0.22	0.22	0.75	0.74
TKE m^2 s^{-2}	0.95	0.90	0.89	1.08	0.82	0.82	0.68	0.67	-0.05	-0.05	0.68	0.67	0.78	0.79

Scatter plots of uncoupled (red) and coupled (blue) COAMPS vs. aircraft observations for potential temperature, sea-surface temperature, air-sea temperature difference, specific humidity, latent heat flux and sensible heat flux are shown in Figure

85. For all scatter plots, the data have been parsed for figure purposes only. The figures shown are representative of the distribution of all data points. The cold bias in potential temperature is obvious from the distribution of the scatter points, with little change from the uncoupled to the coupled model. Sea-surface temperature shows the most obvious improvement between the uncoupled and the coupled model. Uncoupled COAMPS, which received sea-surface temperature from NCODA every twelve hours, had a larger warm bias, and very poor performance when sea-surface temperature was below 292 K. The coupled COAMPS SST values are directly from NCOM every 30 minutes. The sea-surface temperature bias improved by 1.11 K, and NCOM simulation improved for extreme low values of sea-surface temperature. The bias toward an unstable boundary layer is seen in Figure 85c. Specific humidity, shown in Figure 85d, shows little change in the overall distribution between models. However, the bias changed from slightly positive to slightly negative, which is likely due to the large improvement in latent heat flux bias (Figure 85e) simulating less moisture flux into the boundary layer. Due to the improvement in the air-sea temperature difference (Figure 85c) the bias of latent heat flux was reduced from 165 W m^{-2} to 92 W m^{-2}, an improvement of 73 W m^{-2} (Figure 85e). Sensible heat flux was also over-predicted by both models likely due to the unstable bias in the air-sea temperature difference. Thus, the improvement in air-sea temperature difference (Figure 85c) also led to improvement in the sensible heat flux, reducing the bias from 40.91 W m^{-2} to 23.11 W m^{-2}.
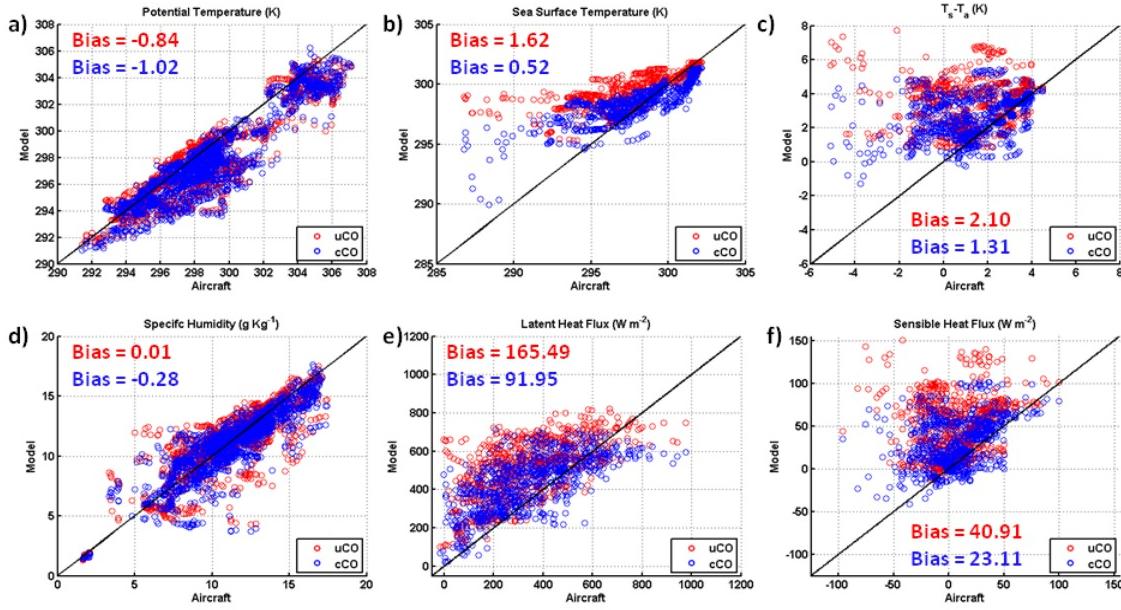
Figure 85.   Scatter plots of model vs. aircraft values for a) potential temperature (K), b) SST (K), c) air-sea temperature difference (K), d) specific humidity (g kg^{-1}), e) latent heat flux (W m^{-2}), and f) sensible heat flux (W m^{-2}). Values for the uncoupled COAMPS are shown in red; COAMPS/NCOM values are shown in blue.

Scatter plots for wind speed and wind stress are shown in Figure 86. There was very little change in the distribution or bias of either wind speed or wind stress between the two models. These results for wind speed and wind stress are similar to those reported in Allard et al. (2010).
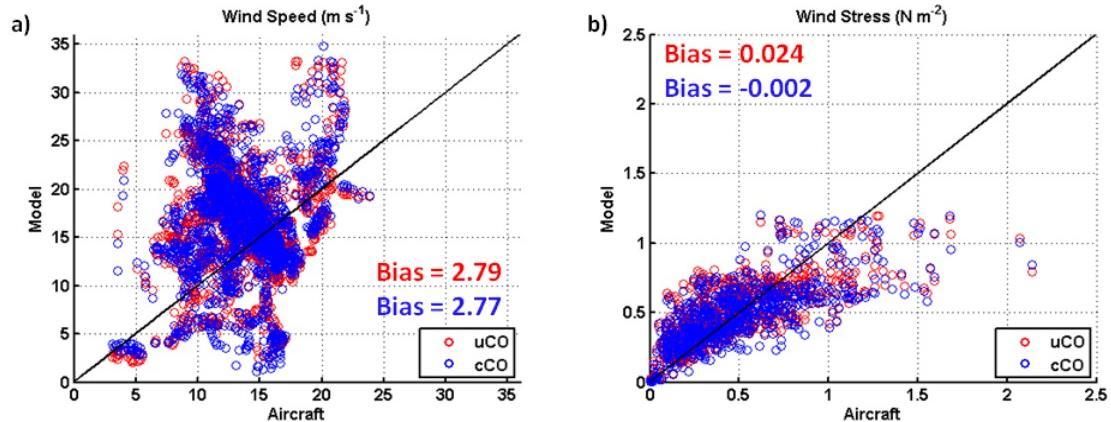
Figure 86.   Scatter plots of model vs. aircraft values for a) wind speed (m s^{-1}), and b) wind stress (N m^{-2}). Values for the uncoupled COAMPS are shown in red; COAMPS/NCOM values are shown in blue.

Scatter plots for the two NCOM variables, wind stress and sea-surface temperature, are shown in Figure 87. Wind stress shows little change in distribution or bias between the uncoupled NCOM and coupled NCOM. For sea-surface temperature, the warm bias actually increases in the coupled NCOM. However, RMSE of the coupled NCOM SST is reduced (Table 4).
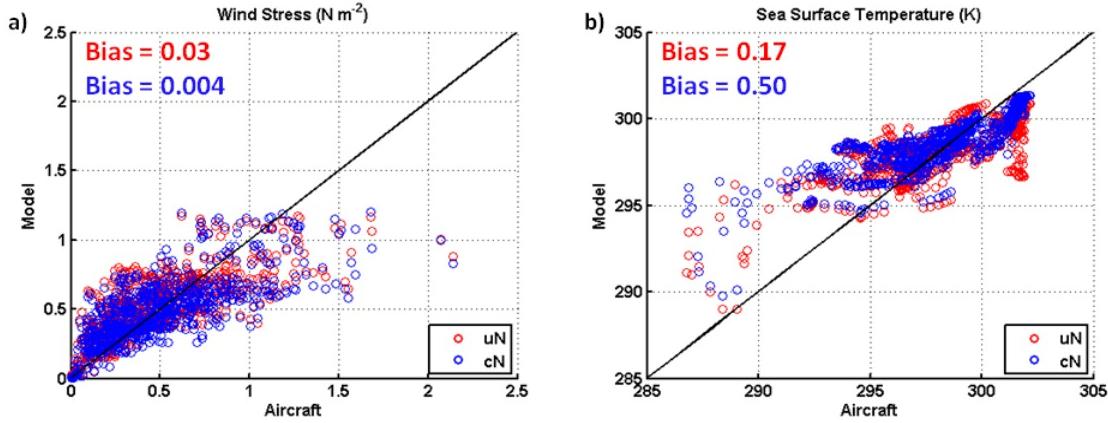
Figure 87.   Scatter plots of model vs. aircraft values for a) wind stress (N m^{-2}), and b) SST (K). Values for the uncoupled NCOM are shown in red; COAMPS/NCOM values are shown in blue.

With the exception of wind stress, all of the surface variables from COAMPS/NCOM appear to benefit from the 2-way coupling process. Using sea-surface temperatures directly from NCOM at an increased coupling frequency, the COAMPS SST values improved by greater than 1 K leading to a reduction in the unstable bias of the air-sea temperature difference. Improvement in the air-sea temperature difference directly resulted in improvements in the simulated sensible and latent heat fluxes. Root mean squared error (RMSE) from Table 4 is presented graphically in Figure 88. The improvement in the performance of sigma-level variables from the coupled model simulations is not as clear. Wind speed and potential temperature each showed a small increase in RMSE, while turbulent kinetic energy showed no change at all. Although the absolute value of the bias increased slightly, the specific humidity error (RMSE) improved by 0.12 g kg^{-1}. The improvement in latent heat flux, which reduced the addition of moisture to the boundary layer, resulted in a slight negative (dry) bias in specific humidity. The improvement in sea-surface temperatures decreased the unstable

bias of the air-sea temperature difference and reduced the over-prediction of sensible heat flux.
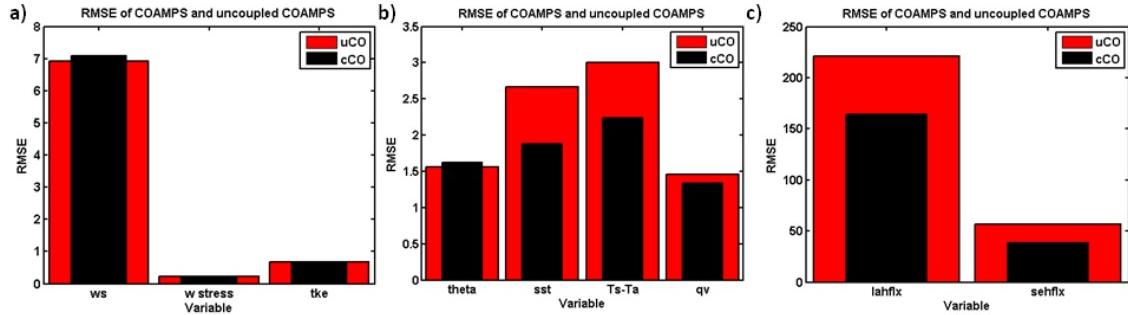
Figure 88.   Root mean squared error (RMSE) for a) wind speed (m s^{-1}), wind stress (N m^{-2}), and TKE (m^2 s^{-2}); b) potential temperature (K), SST (K), air-sea temperature difference (T_s-T_a, K), and specific humidity (g kg^{-1}); c) latent heat flux (lahflx, W m^{-2}), and sensible heat flux (sehflx, W m^{-2}). The uncoupled COAMPS values are in red; coupled COAMPS are in black.

To investigate the model performance in the three regions within the gap outflow, RMSE was calculated for the observations within each of the three regions (Figure 89). Sea-surface temperature errors greatly improved within the Nearshore and Coupling Zone regions (approximately 1.5 K). Offshore, the RMSE of sea-surface temperature increased slightly. During Event V, which provided a large number of the Offshore observations, the Offshore sea-surface temperatures were actually warmer than simulated.   The improvement of air-sea temperature difference across all three regions resulted in improved RMSE for both sensible and latent heat fluxes in all regions also, with the largest improvements in the Nearshore and Coupling Zone regions.   The potential temperature error was slightly worse in every region, as suggested by the overall statistics.   Although specific humidity improved overall, the regional RMSE shows improvement only in the Nearshore region (not shown).
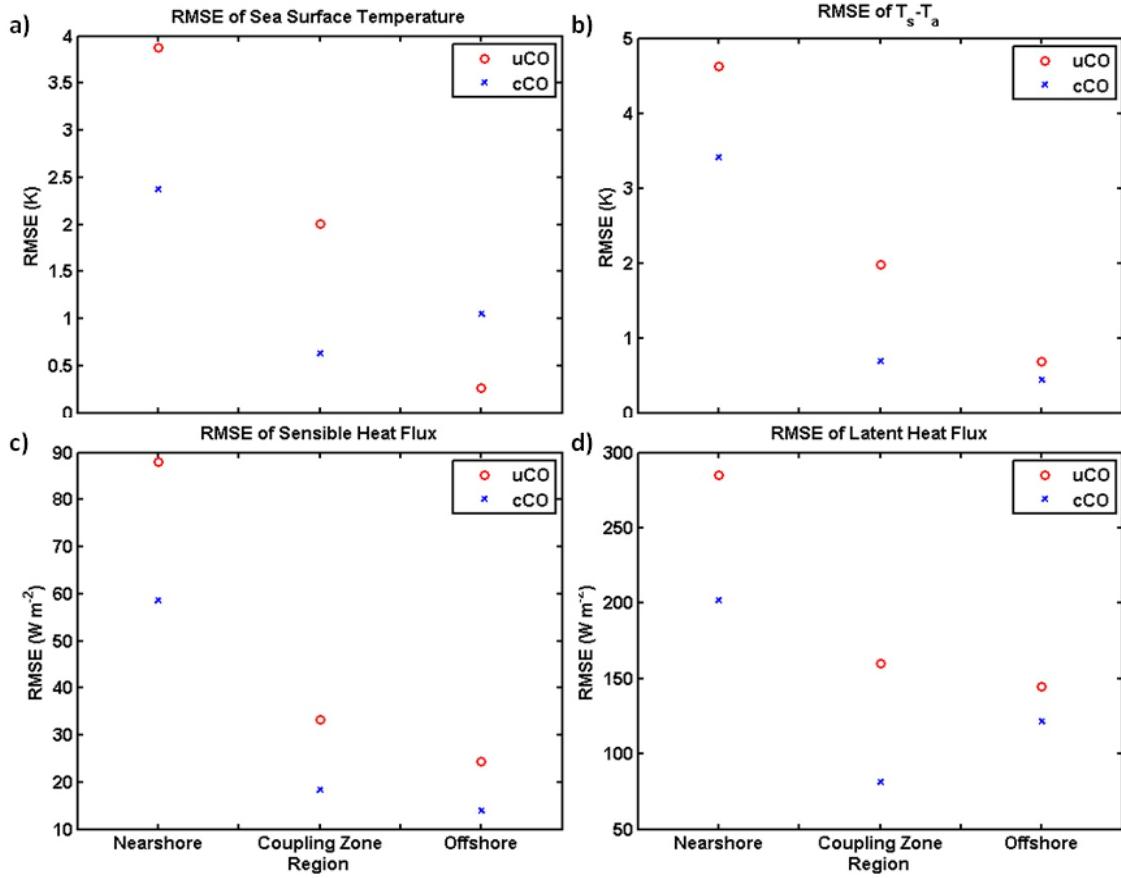
Figure 89. Regional RMSE of a) SST (K), b) air-sea temperature difference (K), c) sensible heat flux (W m^{-2}) and d) latent heat flux (W m^{-2}).

As seen in Table 4, comparing each variable from each model setup creates a large number of statistics from which to draw an overall conclusion. Taylor (2001) described a way to present multiple model statistics for multiple variables on a single diagram, which will be utilized here. Figure 90 shows the normalized Taylor Diagram for uncoupled COAMPS, uncoupled NCOM and coupled COAMPS/NCOM variables. A description of the diagram setup was presented in Chapter III. Uncoupled COAMPS values are shown in red; uncoupled NCOM in green; and coupled COAMPS/NCOM in blue. In general, moving down and towards the observation point on the x-axis represents overall improvement. Comparison between the red/green (uncoupled COAMPS and NCOM) and the blue (COAMPS/NCOM) supports the generalization that the coupled model outperforms the uncoupled model within the confines of the GOTEX

experiment. With the exception of wind speed, all variables show improvement from the uncoupled model to the coupled model, although the changes in wind stress and TKE are especially small. From uncoupled NCOM and coupled COAMPS/NCOM, the sea-surface temperature shows a similar improvement to the uncoupled COAMPS to coupled COAMPS/NCOM SST. Since the uncoupled NCOM receives the wind stress fields from uncoupled COAMPS (at a longer time interval), the improvement in NCOM wind stress is the same as from uncoupled COAMPS, which is minimal. The greatest improvements from the air-sea coupling are seen within the surface variables of air-sea temperature difference sensible heat flux, and latent heat flux. Improvements to these variables through the air-sea coupling are critical because of the important role of temperature and moisture distribution throughout the boundary layer, and the temperature structure in the upper-ocean.
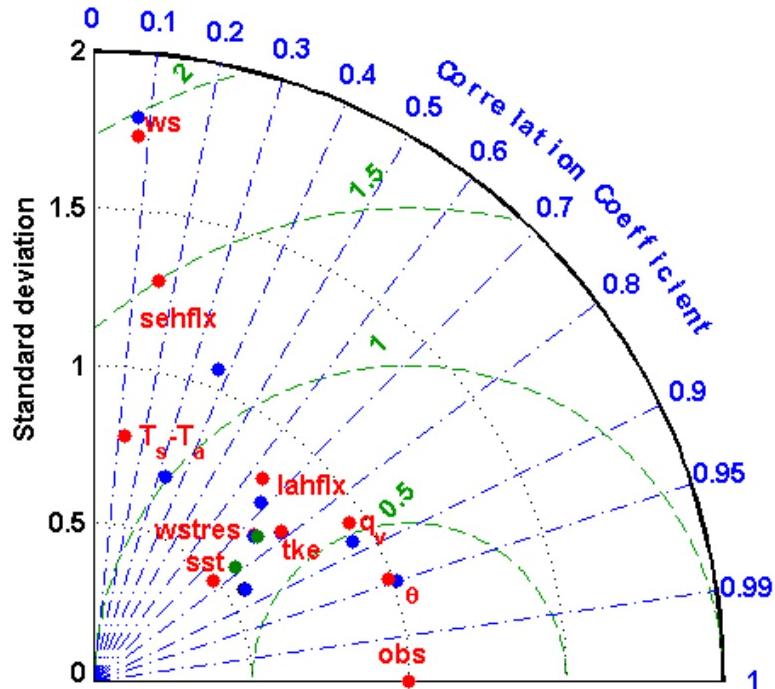
Figure 90. Taylor Diagram for uncoupled COAMPS (red), coupled COAMPS (blue), and coupled NCOM (green) model statistics. All statistics have been normalized according to Taylor (2001) so that the observations have a standard deviation of 1. The vertical axis represents the standard deviation of the model values (black dotted lines). The radial position represents the correlation between the model values and the observations (blue dashed lines). The centered RMS difference is represented by the green dashed lines centered on the observations.

141

The fully-coupled COAMPS/NCOM compared well with observations in the subjective and the statistical evaluations. The magnitude of maximum wind speed during Event II and Event V agreed well with observations, although the jet elevation was too high and the depth of the strongest winds within the jet core was greater than within the dropsonde observations. The simulated potential temperature throughout the cross sections agreed well with the dropsondes differing by less than 1 K throughout all three outflow regions. The well-mixed boundary layer was deeper in the simulations than observed. The simulated specific humidity cross sections were too moist within the Nearshore and Coupling Zone regions, but too dry within the Offshore region. The dropsondes revealed that the boundary layer was highly stratified in moisture, which was well-represented by the coupled model cross sections. The raised thermocline in the AXBT cross sections were well-modeled by coupled NCOM. Although within the Coupling Zone, NCOM was 2 K warmer than the observations.

The consolidation of model error statistics using the Taylor diagram revealed that all variables, except wind speed, were improved by the model coupling. The improvement in sea-surface temperature, evident in the lower bias, lower $RMSE_C$, and higher correlation coefficient, led to an improvement in the air-sea temperature difference. As the bias toward an unstable boundary layer was reduced, additional improvements in sensible heat flux and latent heat flux were also seen. The change in sensible heat flux appeared to have little influence on the potential temperature. However, the smaller bias in latent heat flux, which reduced the over-prediction of upward latent heat flux, may be the reason for the slightly dry bias in specific humidity. Wind stress and TKE showed very little change. Minimal differences were seen in the wind speed statistics, but the representation on the Taylor diagram showed that it was the only variable that did not benefit from coupling of the ocean-atmosphere models. Although the wind speed did not improve, and potential temperature and specific humidity showed only slight improvements, the benefit of the model coupling is primarily the surface heat fluxes. NCOM provided more realistic sea-surface temperature

142

through the high-frequency coupling, which improved the air-sea temperature difference. The resulting improvement in sensible and latent heat fluxes ultimately represent more realistic atmospheric forcing on the ocean surface.

THIS PAGE INTENTIONALLY LEFT BLANK

VII. SUMMARY, CONCLUSIONS, AND RECOMMENDATIONS

A. SUMMARY OF ANALYSIS METHODS

The Gulf of Tehuantepec gap outflow has been previously studied using relatively limited measurements of the atmosphere or ocean, and stand-alone atmosphere or ocean models. The GOTEX data set provided greater spatial and temporal coverage of co-located atmosphere and ocean measurements, including *in situ* fluxes. Analysis of the GOTEX data set revealed more detail about the downwind development and temporal evolution of the atmospheric and ocean boundary layers. Three distinct regions within the outflow were identified from the aircraft observations. Each of these regions had unique response characteristics to the outflow forcing. Two-way coupled COAMPS/NCOM simulations were used to investigate the spatial and temporal evolution and more fully understand the differences among these three regions beyond the limitations of the GOTEX observations. Finally, an evaluation of the uncoupled and coupled models using all available aircraft data revealed overall improvement in the surface-flux estimation by the coupled COAMPS/NCOM, mainly due to the improvement in sea-surface temperature and thus improvement in the air-sea temperature difference.

The GOTEX data set is unique in that it provides measurements during five outflow events. All five of these events, measured by nine research flights, were studied to identify previously unknown aspects of the spatial and temporal evolution of the gap outflow. Based on the analysis of all of the flights, patterns emerged which suggested that there were three regions within the outflow that had distinct response characteristics within the atmospheric boundary layer and ocean mixed layer. For the in-depth analysis, two events (Events II and V) were chosen as case studies because during each event, back-to-back flights were flown on successive days, providing temporal measurements available for the first time from GOTEX. Using all available aircraft data from flights RF02, RF03, RF09 and RF10, the spatial and temporal evolution of the atmospheric boundary layer and ocean mixed layer were analyzed.

145

Two-way coupled model simulations using COAMPS V. 5 and NCOM V. 4 were available for the GOTEX period, providing the first coupled model study within this region. For the two case studies, model output was used to further understand the distinct differences among the three regions identified in the observational analysis. Heat budget calculations of the ocean mixed layer were conducted for each event to determine the dominant cooling mechanisms during the gap outflow events.

Finally, an evaluation of the uncoupled and coupled COAMPS and NCOM model output was conducted. Model output was compared to aircraft measurements from nine GOTEX flights, providing coverage over a large area within the GoT and during a variety of outflow development stages. Model error statistics were calculated for all model-observation pairs and analyzed for changes in model performance. This model evaluation was unique because it used *in situ* flux measurements rather than flux estimates based on the bulk formulations.

B.   CONCLUSIONS

The initial hypothesis of this study was that the Gulf of Tehuantepec region was the ideal "natural laboratory" for studying air-sea interactions because the air-sea coupling dominated the downwind development and temporal evolution of the atmospheric boundary layer and ocean mixed layer. Prior to this study, the Gulf of Tehuantepec gap outflow had been studied as a mesoscale phenomenon that showed significant variability of surface fluxes and sea-surface temperature within the outflow region. The analysis of GOTEX observations revealed that the gap outflow has three distinct regions with unique response characteristics. General characteristics of the gap outflow agree well with previous studies. The advection of cold, dry air by the strong northerly winds is most evident closest to the coast. Sea-surface temperatures cool significantly as a result of strong surface forcing. And, the west side of the outflow jet turns anticyclonically while the east side appears to follow a straight or only slightly cyclonic trajectory. However, based on this work, further details are available with respect to the variability within the outflow region.

The Nearshore region extends from the coast over the gently sloping continental shelf to the 500 m bathymetry curve. During the strengthening stage of the gap outflow, it is within this region where the coldest, driest boundary layer air is found. The elevated jet maximum is at its highest elevation and the surface forcing on the upper-ocean is strongest. Cold sea-surface temperatures stabilize the boundary layer within this region, and sensible heat flux is generally negative. By the decay stage of the gap outflow, wind stress and turbulence within the Nearshore have weakened and although the sea-surface temperatures continue to cool, the strongest forcing on the upper-ocean has moved to over the Coupling Zone region. From the AXBT profiles, the high variability in the ocean temperature structure is obvious. Several Nearshore profiles showed the absence of a mixed layer due to strong upwelling raising the thermocline to the surface, while other profiles show a shallow but very cold ocean mixed layer. From the limited AXBTs from GOTEX, the ocean dynamics close to the coast are not yet fully understood.

The Coupling Zone region reaches offshore from the 500 m bathymetry curve. Although the boundary of this zone was nominally defined using the aircraft low-level sea-surface temperature measurements, and determining where the change in sea-surface temperature was at a minimum, no objective criterion was found to define the outer limit to this region. It was within this region that air-sea interactions were thought to be a dominant mechanism to changes in the atmospheric boundary layer and ocean mixed layer; beyond the immediate influence of the topographic forcing, but affected by strong turbulence. Within the atmospheric boundary layer, temperature increases while wind speed weakens with distance from shore. The maximum latent heat flux is within this region (with exception of one flight, RF09), where the boundary layer remains unstable and the advection of cold, dry air is still strong. A slight increase in moisture within the boundary layer indicates that the moistening rates from latent heat-flux divergence and horizontal advection are no longer in balance. Sea-surface temperatures begin to cool immediately and continue to cool throughout the event. The ocean mixed layer persists throughout the event, although the response is not as clear as expected. The mixed layer and thermocline depth are highly variable, while entrainment mixing at the base of the OML is persistent throughout the event. The variability along the thermocline is the

result of upwelling due to Ekman pumping or possibly the propagation of internal waves along the thermocline, which have been documented within this region (Apel and Jackson 2002).

The Offshore region is beyond the area where there are significant changes to the atmospheric boundary layer and ocean mixed layer. The spatial and temporal variability within this region is much smaller compared to the other two regions. Contrary to the initial analysis which defined the Offshore region where there was no cooling of sea-surface temperatures, the selected Offshore region did show slight cooling of sea-surface temperatures. There is also more variability within the ocean temperature structure than expected. While the mixed layer remains relatively deep (>30 m), the thermocline was highly variable.

The exception to the patterns seen throughout the regions is RF09. Especially within the Nearshore region, the RF09 ocean mixed layer characteristics do not show a similar response. However, RF09 was measured sooner than others after the onset of Event V. While the atmospheric boundary layer had already begun to respond, the ocean mixed layer had not. By RF10, the characteristics of the ABL and OML support the evolution identified in Event II.

The mechanisms for moisture exchange within the gap outflow are generally well-balanced leading to very little variability in the specific humidity. Since the gap winds are known to bring dry air into the GoT, little has been studied about the spatial gradients of moisture within the outflow. It is found that the specific humidity increased slightly from the coast to the Offshore region. A comparison of moistening from the latent heat-flux divergence and drying from horizontal advection revealed that these two mechanisms are mostly in balance throughout the outflow; leading to only small temporal changes in specific humidity.

The potential temperature within the outflow is more complicated because of diurnal variation of the upstream air temperature. The most significant impact of the upstream land happens naturally within the Nearshore region. This variation is apparent in the comparison of the aircraft measurements near shore at the beginning (morning) and

148

at the end (afternoon) of RF03. The diurnal variations are also seen in the Coupling Zone and the Offshore region as indicated by COAMPS results, with a smaller magnitude (about 1 K) than within the Nearshore region. However, during the intensification stage of the outflow event (i.e. RF02), the diurnal variation seems to be masked by the strong response of the lower atmosphere to abrupt changes of air mass due to strong advection and modification by the evolving underlying surface.

Analysis of the simulated evolution from coupled COAMPS/NCOM provided additional insight to augment the aircraft observations. The high-resolution COAMPS model revealed the presence of a secondary gap outflow jet to the east of the Chivela Pass jet. It is hypothesized that this secondary jet may have significant impact on the upper-ocean dynamics, especially on the disintegration of the cyclonic circulation east of the outflow jet. The asymmetric response to symmetric forcing has been a major factor in the discussion of the ABL and OML response to the GoT outflow jet. Due to the high grid spacing of the coupled model, including the terrain, a secondary jet is clearly seen to the east of the main GoT jet. This jet was first mentioned in the thesis work of Cherrett (2006), but follow-on studies were not conducted. From these coupled simulations, the existence of this second jet is much clearer. The pass through which this second jet originates is 200 km east of the Chivela Pass. The minimum elevation is 750 m, roughly 500 m higher than the Chivela Pass, and it spans the width of the isthmus. Observations of a separate jet have never been reported because most of the remote sensors (i.e. satellite winds) do not have the grid spacing to resolve the difference between the two jets. Additionally, because the presence of this jet was unknown, no field experiments have extended their collection far enough to the east to measure this second jet. COAMPS/NCOM simulations clearly show a second jet originating from this slightly higher pass. At 3 km grid spacing, the outflow jets do not merge. A narrow strip of flow convergence and minimum wind speed remains between the two jets, following a slightly anticyclonic trajectory.

Both GOTEX observations and model results of wind direction very close to the coast show cyclonic turning to the east of the jet axis, contrary to the previous arguments against it. This suggests that close to the coast, before the two jets begin to interact, the

east side of the main jet is subject to cyclonic turning. However, less than 50 km from the coast, the influence of the second jet, and the convergence zone created between them, prevent cyclonic turning to the east of the GoT jet, and anticyclonic turning on the west side of the secondary jet. Therefore, when viewed from the coarse resolution of the satellite, it appears that the east side of the GoT jet is dominated by almost straight trajectories.

If this second jet is indeed an actual feature within the GoT, its presence sheds new light on the asymmetric response of the ABL and OML. While the opposite forces of cross-flow pressure gradient acceleration and Coriolis acceleration generally explain the lack of cyclonic turning to the east, the influence of a second jet, with its own balance of forces could be a stronger influence. The convergence between the two jets prevents the Chivela Pass jet from exhibiting cyclonic turning to the east, and the second jet from exhibiting anticyclonic turning to the west, resulting in what has previously appeared to be rather straight flow from the main jet.

One of the major features that drive the discussion of the asymmetric response is the cyclonic ocean circulation to the east. Previous studies have noted that while the anticyclonic ocean eddy shows a clear signature in surface measurements of currents, or even satellite sea-surface temperatures, either a very weak cyclonic circulation, or often none at all is seen to the east. Trasviña et al.(1995) attributed the weak cyclonic response to the combination of Ekman divergence in a very shallow mixed layer to the east along with weakened density gradients due to strong entrainment mixing. The NCOM simulations clearly show a cyclonic circulation, which remains slightly weaker than the anticyclonic eddy, between events. With the strong surface forcing from both gap outflow jets, the surface currents during events are dominated by ageostrophic flow nearshore, and a combination of ageostrophic flow and Ekman transport further offshore. The signature of the cyclonic circulation is not seen in the surface currents from NCOM during any GOTEX events. However, below the surface (20 m depth was most commonly used), the cyclonic circulation persisted. Ocean measurements at depth, especially current measurements, to the east in the Gulf of Tehuantepec are not available to confirm the existence of this circulation below the surface.

Finally, our detailed analyses of the upper-ocean heat budget revealed the dominant mechanisms in determining the sea-surface temperature evolution in different regions of the GoT. This study showed that entrainment mixing is the dominant cooling mechanism followed by heat loss due to surface fluxes in the Nearshore and Coupling Zone regions. Horizontal advection can play different roles depending on the location. In the Nearshore region, it warms up the upper-ocean due to convergence of the warm water toward the center of the gap exit. However, its magnitude can be much smaller compared to entrainment mixing. Upwelling in the Nearshore region is strong, but cooling in the OML as a result of upwelling is very small due to the small vertical gradient in temperature in the ocean mixed layer.

Although few ocean measurements have been made *in situ* during the recovery phase after a gap outflow event, previous studies have estimated the recovery time of the sea-surface temperatures from 5–50 days. Sea-surface temperature time series from coupled NCOM suggest that the sea-surface temperatures begin rebounding sometime between when the outflow event begins to decay and wind stress reaches a post-event minimum. The average recovery time for the GOTEX events was 2 days, with the Nearshore region recovering more quickly than the Coupling Zone region. During prolonged outflow events, the magnitude of sea-surface temperature cooling within the Offshore region increases. In these cases, the Offshore region exhibits an even slower recovery than the Coupling Zone. The Nearshore region recovers more quickly because the mixed layer is shallower so that solar heating can increase the mixed layer temperature more quickly, and horizontal advection brings warm water toward the mouth of the Gulf. Entrainment mixing due to turbulence drops off quickly throughout all three regions as the wind stress decreases.

Based on the divergence forced by the offshore flow, coastal upwelling was hypothesized to be one of the dominant mechanisms contributing the cooling of the ocean mixed layer. Based on the heat budget calculations, the entrainment cooling rate and loss of heat due to upward surface fluxes are the two dominant mechanisms, while the cooling from vertical advection is very small. The improvement of the surface fluxes within the coupled model resulted in more realistic ocean forcing within the outflow.

151

Comparisons of the uncoupled and coupled COAMPS simulations showed little change in the general feature of the outflow jet, or the boundary layer characteristics. Surface fluxes did improve within the coupled model. However, the feedback of the air-sea coupling was expected to improve both the simulation of the atmospheric boundary layer and the ocean mixed layer. While the model evaluation did indicate improvement in all variables except wind speed, the improvement in the ABL due to coupling in the model coupling was minimal. However, since the dominant cooling mechanisms of the OML are based on the surface heat fluxes and turbulence, the coupled model should lead to improvements in the simulation of the ocean mixed layer in NCOM. With limited ocean measurements, the total benefit of this coupling on the ocean simulation cannot be fully evaluated.

C.   RECOMMENDATIONS FOR FUTURE WORK

Although this study did not focus on the synoptic forcing for each of the events, it is clear that the temporal and spatial variability of the lower atmosphere is predominantly controlled by the large-scale setting that established the magnitude of the pressure gradient and the time duration of the strong gradient. This study suggested that the boundary layer temperature and water vapor are mainly controlled by the horizontal advection by the outflow wind and turbulent flux divergence. In order to fully understand and predict the controlling factors of the jet development, a better understanding of the role of synoptic forcing is necessary. This would provide even more insight into the small scale spatial and temporal evolution described here. While the synoptic conditions which trigger these events have been studied in general, comparison of the synoptic conditions between events to understand how the large-scale forcing affects event characteristics has not. In particular, the recovery response of the cold ocean mixed layer appears to be driven by the event duration, rather than local forcing effects.

Since the largest improvement in the coupled model was seen within the surface heat fluxes, it would be beneficial to study the sensitivity of the resultant surface fluxes to choices of different parameters or different types of surface flux parameterizations.

Because of the strong wind and significant temporal/spatial variability, a complex wave field likely prevailed throughout the GoT region during Tehuano events. It is desirable to understand the relationship between the wave field and the surface fluxes from both observations and modeling efforts when wave measurements and coupled atmospheric-wave-ocean models are available. Concurrent measurements from the GOTEX wave field and surface fluxes should be valuable in improving sea-state dependent surface flux parameterizations.

One of the most interesting findings from this high-resolution model study was the identification of a secondary jet east of the Chivela Pass jet. Two-way COAMPS/NCOM simulations are already available for a study of the dynamics of this outflow jet and its influence on the asymmetric response within the Gulf of Tehuantepec. In addition to a detailed simulation study of this secondary jet, if future field work is considered in this region, it is recommended to broaden the typical collection area to include the eastern part of the GoT so that observations can be used to better understand the influence of this second jet.

A lack of ocean measurements, especially current measurements, prevents a full understanding of the ocean dynamics within this region. However, with the simulated persistence of the cyclonic circulation, it would especially interesting to understand how the second jet influences the circulation to the east of the Gulf of Tehuantepec. Additionally, coastal upwelling studies have traditionally focused on regions with alongshore flow which forces upwelling driven by Ekman transport. In this study, we relied on the divergence of mass transport to differentiate between coastal upwelling due to Ekman and alongshore flow, and the offshore ageostrophic transport forced by the Gulf of Tehuantepec jet.

THIS PAGE INTENTIONALLY LEFT BLANK

LIST OF REFERENCES

Allard, R. A., Campbell, T. J., Smith, T. A., Jensen, T. G. Cummings, J. A., Chen, S., Doyle, J., Hong, X., Small, R. J., and S. N. Carroll, 2010: Validation test report for the Coupled Ocean Atmospheric Mesoscale Prediction System (COAMPS) version 5. Naval Research Laboratory Rep. NRL/MR/7320–10–9283, 172 pp. [Available online at http://www7320.nrlssc.navy.mil/pubs/2010/allard2-2010.pdf]

Apel, J. R. and C. R. Jackson, 2002: *An Atlas of Internal Solitary-like Waves and their Properties*. Global Ocean Associates, Rockville, MD.

Bao, J.-W., Wilczak, J.M., Choi, J.-K., Kantha, L.H., 1999: Numerical Simulations of Air-Sea Interaction under High Wind Conditions Using a Coupled Model: A Study of Hurricane Development, *Mon. Wea. Rev.*, **128**, 2190–2210.

Barton, E. D., Argote, M.L., Brown, J., Kosro, P.M., Lavin, M., Robles, J.M., Smith, R.L., Trasviña, A., Velez, H.S., 1993: Supersquirt: Dynamics of the Gulf of Tehuantepec, Mexico. *Oceanography,* **6,** 23–30.

Brennan, M.J., Cobb, H.D.III, Knabb, R.D., 2009: Observations of Gulf of Tehuantepec Gap Wind Events from QuikSCAT: An Updated Event Climatology and Operational Model Evaluation, *Weather and Forecasting*, **25**, 646–658.

Bryan, F. O., Kauffman, B. G., Large, W. G., and P. R., Gent, 1996: The NCAR CSM Flux Coupled, Technical Report TN-245+STR, National Center for Atmospheric Research, Boulder, Co. 70pp.

Clarke, A. J., 1988: Inertial wind path and sea-surface temperature patterns near the Gulf of Tehuantepec and Gulf of Papagayo, *J. Geophy. Res.*, **V93, C12**, 15491–15501.

Chen, S., T. J. Campbell, H. Jin, S. Gabersˇek, R. H. Hodur, and P. Martin, 2010: Effect of two-way air–sea coupling in high and low wind speed regimes. *Mon. Wea. Rev.*, **138**, 3579–3602.

Cherrett, R. C. 2006: Observed and Simulated temporal and spatial variations of the gap outflow region, M.S. Thesis, Meteorology Department, Naval Postgraduate School, 63.

Chelton, D. B., M. H. Freilich, and S. K. Esbensen, 2000a: Satellite observations of the wind jet off the Pacific coast of Central America. Part I: case studies and statistical characteristics, *Mon. Wea. Rev.*, **128**, 1993–2018.

Chelton, D. B., M. H. Freilich, and S. K. Esbensen, 2000b: Satellite observations of the wind jet off the Pacific coast of Central America. Part II: Regional relationships and dynamical considerations. *Mon. Wea. Rev.*, **128**, 2019–2043.

Collins, N., G. Theurich, C. DeLuca, M. Suarez, A. Trayanov, V. Balaji, P. Li, W. Yang, C. Hill, and A. da Silva, 2005: Design and Implementation of Components in the Earth System Modeling Framework. *International Journal of High Performance Computing Applications*, **19**, Number 3, 341–350.

Deng, Z., Xie, L., Lie, B., Wu, K., Zhao, D., and T. Yu, 2009: Coupling winds to ocean surface currents over the global ocean, *Ocn. Model.*, **29**, 261–268.

Dorman, C. E., R. C. Beardsley, and R. Limeburner, 1995: Winds in the Strait of Gibraltar. *Quart. J. Roy. Meteor. Soc.,* **121,** 1903–1921.

Drennan, W. M., Graber, H. C., Hauser, D., and C. Quentin, 2003: On the wave age dependence of wind stress over pure wind seas, *J. Geophys. Res.*, **108**, C3, 8062–8075.

Estrade, P., P. Marchesiello, A. Colin de Verdiere, and C. Roy (2008), Cross-shelf structure of coastal upwelling: A two-dimensional expansion of Ekman's theory and a mechanism for inner shelf upwelling shut down, *J. Mar. Res.,* **66**, 589–616.

Fairall C W, E F Bradley, J E Hare, A Grachev, and J B Edson, 2003: Bulk parameterization of air-sea fluxes: Updates and verification for the COARE algorithm, *J. Climate*, **16**, 571–591.

Friehe, C. A., W. J. Shaw, D. P. Rogers, K. L. Davidson, W. G. Large, S. A. Stage, G. H. Crescenti, S. J. S. Khalsa, G. K. Greenhut, and F. Li, 1991: Air-sea fluxes and surface layer turbulence around a sea-surface temperature front. *J. Geophys. Res.*, **96**, 8593–8609.

Fu, W. Zhou, G., and H. Wang, 2006: Modeling the Tropical Pacific Ocean Using a Regional Coupled Climate Model, *Adv. Atmos. Sci.*, **23**, No. 4, 625–638.

Gill, A. E., 1982: *Atmosphere-Ocean Dynamics*. Academic Press, Inc., 662 pp.

Hill, C., C. DeLuca, V. Balaji, M. Suarez, and A. da Silva, 2004: Architecture of the Earth System Modeling Framework. *Computing in Science and Engineering*, **6**, Number 1, pp. 18–28.

Hodur, R. M., 1997: The Naval Research Laboratory's Couple Ocean/Atmosphere Mesoscale Prediction System (COAMPS), *Mon. Wea. Rev.,* **125**, 1414–1430.

Hong, X., S. Wang, T. R. Holt, P. J. Martin, L. O'Neill, 2012: Modulation of the Sea-Surface Temperature in the Southeast Pacific by the Atmospheric Low-Level Coastal Jet. *J. Geophys. Res.Ocn*, submitted.

Hurd, W. E., 1929: Northers of the Gulf of Tehuantepec. *Mon. Wea. Rev.,* **57,** 192–194.

Jerlov, N. G., 1968: *Optical Oceanography*. Elsevier, 199 pp.

Knauss, J. A., 1997: *Introduction to Physical Oceanography*. Waveland Press, Inc., 309pp.

Konstantinou, N. 2006: Ocean mixed layer response to gap wind scenarios, M.S. Thesis, Meteorology Department, Naval Postgraduate School, 63.

Kundu, P. K., and I. M. Cohen, 2008: *Fluid Mechanics*. 4th ed. Elsevier Inc., 872 pp.

Larson, J. W., Jacob, R. L., Foster, I. and J. Guo, 2001: The Model Coupling Toolkit, *Proc. 2001 International Conf. on Computational Sci.*, 185–191.

Lebaupin-Brossier, C.L., Drobinski, P., 2009: Numerical high resolution air-sea coupling over the Gulf of Lions during two Tramontane/Mistral events. *J. Geophys. Res*. **114**, D10110.

Li, F., W. Large, E. J. Walsh, and K. Davidson, 1989: Ocean radar backscatter relationship with near-surface winds: a case study during FASINEX. *J. Phys. Oceanogr.*, **12,** 342–353.

Liu, M., Nachamkin, J.E., Westphal, D. L., 2008: On the improvement of COAMPS Weather Forecasts Using an Advanced Radiative Transfer Model, *Weather and Forecasting*, **24**, 286–306.

Liu, H., Lin, W., and M. Zhang, 2010: Heat Budget of the Upper-ocean in the South-Central Equatorial Pacific, *J. Climate*, **23**, 1779–1792.

Louis J-F, 1979: A parametric model of vertical eddy fluxes in the atmosphere. *Bound.-Layer Meteorol*, **17**,187–202.

Martin, P. J., 2000: Description of the NAVY Coastal Ocean Model Version 1.0, NRL 801 Report:NRL/FR/7322–00–9962.

Mass, C. F., S. Businger, M. D. Albright, and Z. A. Tucker, 1995: A windstorm in the lee of a gap in a coastal mountain barrier. *Mon.Wea. Rev.,* **123,** 315–331.

Mass, C.F.; Ovens, D.; Westrick, K., and Colle, B.A., 2002: Does increasing grid spacing produce more skillful forecasts? *Bulletin of the American Meteorological Society*, **83**, 407–430.

McCreary, J. P., H. S. Lee, and D. B. Enfield, 1989: The response of the coastal ocean to strong offshore winds: With application to circulation in the Gulfs of Tehuantepec and Papagayo. *J. Mar.Res.,* **47,** 81–109.

Mellor, G., and T. Yamada, 1974: A hierarchy of turbulence closure models for planetary boundary layers. *J. Atmos. Sci.,* **31,** 1791–1806.

Mellor, G. L., and T. Yamada, 1982: Development of a turbulence closure model for geophysical fluid problems. *Rev. Geophys.,* **20**, 851–875.

Nasa's Jet Propulsion Laboratory, California Institute of Technology, Physical Oceanography Distributed Active Archive Center (PO.DAAC) , [Available online at http://podaac.jpl.nasa.gov/], last accessed August 2012.

NCAR Earth Observing Laboratory, cited 2012: NCAR EOL C-130 Investigator Handbook. [Available online at http://www.eol.ucar.edu/instrumentation/aircraft/C-130/documentation/c-130-investigator-handbook/c-130-investigator-handbook/], last accessed August 2012.

Overland, J. E., and B. A. Walter Jr., 1981: Gap winds in the Strait of Juan de Fuca. *Mon. Wea. Rev.*, **109**, 2221–2233.

Paulson, C. A., and J. J. Simpson, 1977: Irradiance measurements in the upper-ocean. J. Phys. Oceanogr., **7**, 952–956.

Perlin, N., Skyllingstad, E. D., and R. M. Samelson, 2011: Coastal Atmospheric Circulation around an Idealized Cape during Wind-Driven Upwelling Studies from a Coupled Ocean-Atmosphere Model, *Mon. Wea. Rev.*, **139**, 809–829.

Powers, J. G., and M. T. Stoelinga, 2000: A coupled air-sea mesoscale model: Experiments in atmospheric sensitivity to marine roughness, *Mon. Wea. Rev.*, **128**, 208–228.

Renault, L., Dewitte, B., Marchesiello, P., Illig, S., Echevin, V., Cambon, G., Ramos, M., Astudillo, O., Minnis, P., and J. K. Ayers, 2012: Upwelling response to atmospheric coastal jets off central Chile: A modeling study of the October 2000 Event, *J. Geophys. Res.*, **117**, C02020.

Roden, G. I.,1961. On the wind-driven circulation in the Gulf of Tehuantepec and its effect upon surface temperatures. *Geofis. Int., I*, 55–72, 1961.

Schultz, D. M., W. E. Bracken, L. F. Bosart, G. J. Hakim, M. A. Bedrick, M. J. Dickinson, and K. R. Tyle, 1997: The 1993 Superstorm cold surge: Frontal structure, gap flow, and tropical impact. *Mon. Wea. Rev.*, **125**, 5–39; Corrigendum, 125, 662.

Schultz, D. M., W. E. Bracken, L. F. Bosart, G. J. Hakim, M. A. Bedrick, M. J. Dickinson, and K. R. Tyle, 1998: Planetary- and synoptic-scale signatures associated with Central American cold surges. *Mon. Wea. Rev.,* **126,** 5–27.

Steenburgh, W. J., D. M. Schultz, and B. A. Colle, 1998: The Structure and Evolution of Gap Outflow over the Gulf of Tehuantepec, Mexico. *Mon. Wea. Rev.*, **126**, 2673–2691.

Stull, R. B., 1988: *An Introduction to Boundary Layer Meteorology*. Kluwer Academic Publishers, 666 pp.

Stumpf, H.G., 1975: Satellite detection of upwelling in the Gulf of Tehuantepec, Mexico. *Mar. Wea. Log*, **19**, 71–74.

Taylor, K. E., 2001: Summarizing multiple aspects of model performance in a single diagram. *J. Geophys. Res.*, **106**, 7183–7192.

Thomson, R. E. and I. V. Fine , 2003: Estimating mixed layer depth from oceanic profile 820
Data, *J. Atmos. Oceanic Technol.*, **20**, 319–329.

Trasviña Castro, A., E. D. Barton, J. Brown, H. S. Velez, P. M. Kosro, and R. L. Smith, 1995: Offshore wind forcing in the Gulf of Tehuantepec, Mexico: The asymmetric circulation. J. Geophys. Res., 100, 20 649–20 663.

UCAR COMET MetEd, cited 2012: COMET Gap Wind Module. [Available online at https://www.meted.ucar.edu/training_module.php?id=111], last accessed August 2012.

Von Storch, J. S., 2000: Signatures of Air-Sea Interactions in a Coupled Atmosphere-Ocean GCM, *J. Climate*, **13**, 3361–3379.

Wang, S., Wang, Q., and J. Doyle, 2002: Some improvement of Louis surface flux 825
Parameterization, *Preprints, 15th Symp. On Boundary Layers and Turbulence*, **826** Wageningen, Netherlands, Amer. Meteor. Soc., 547–550, 2002.

Wen, Y., Huang, L., Deng, J. Zhang, J. Wang, S., and L. Wang, 2006: Framework of Distributed Coupled Atmosphere-Ocean-Wave Modeling System, *Adv. Atmos. Sci.*, **23**, No. 3, 442–448.

Wilks, D. S., 1995: *Statistical Methods in the Atmospheric Sciences*. Academic Press, Inc., 467 pp.

Xie, S.-P., Xu, H., Kessler, W.S., Nonaka, M., 2005: Air-Sea Interaction over the Eastern Pacific Warm Pool: Gap Winds, Thermocline Dome, and Atmospheric Convection, *J. Climate*, **18**, 5–20.

Zhang, J.A., Drennan, W.M., Black, P.G., French, J.R., 2009: Turbulence Structure of Hurricane Boundary Layer between the Outer Rainbands, *J. Atmos. Sci.*, **66**, 2455–2467.

Zhuo, T., Yu, Y., Yu, R., Liu, H., Li, W., and X. Zhang, 2004: Coupled climate system model coupler review, *Adv. Atmos. Sci.*, **28**,, 993–1008.

INITIAL DISTRIBUTION LIST

1.   Defense Technical Information Center
        Ft. Belvoir, Virginia

2.   Dudley Knox Library
        Naval Postgraduate School
        Monterey, California

3.   Chairman, Code 372
        Department of Meteorology
        Naval Postgraduate School
        Monterey, California

4.   Professor Qing Wang
        Department of Meteorology
        Naval Postgraduate School
        Monterey, California

5.   Professor Joshua Hacker
        Department of Meteorology
        Naval Postgraduate School
        Monterey, California

6.   Professor Patrick Harr
        Department of Meteorology
        Naval Postgraduate School
        Monterey, California

7.   CAPT Rebecca Stone
        Graduate School of Engineering and Applied Sciences
        Naval Postgraduate School
        Monterey, California

8.   Dr. Shouping Wang
        Naval Research Laboratory
        City, State

9.   Dr. Xiaodong Hong
        Naval Research Laboratory
        Monterey, California

10.   LCDR Heather R. Hornick
        Little Creek, Virginia